MAGNETIC RESPONSE MEASUREMENTS OF MESOSCOPIC SUPERCONDUCTING AND NORMAL METAL RINGS

A DISSERTATION
SUBMITTED TO THE DEPARTMENT OF PHYSICS
AND THE COMMITTEE ON GRADUATE STUDIES
OF STANFORD UNIVERSITY
IN PARTIAL FULFILLMENT OF THE REQUIREMENTS
FOR THE DEGREE OF
DOCTOR OF PHILOSOPHY

Hendrik Bluhm
December 2007

I certify that I have read this dissertation and that, in my opinion, it is fully adequate in scope and quality as a dissertation for the degree of Doctor of Philosophy.

(Kathryn A. Moler) Principal Adviser

I certify that I have read this dissertation and that, in my opinion, it is fully adequate in scope and quality as a dissertation for the degree of Doctor of Philosophy.

(Steven A. Kivelson)

I certify that I have read this dissertation and that, in my opinion, it is fully adequate in scope and quality as a dissertation for the degree of Doctor of Philosophy.

(David Goldhaber-Gordon)

Approved for the University Committee on Graduate Studies.

Abstract

The main part of this thesis reports three experiments on the magnetic response of mesoscopic superconducting and normal metal rings using a scanning SQUID microscope.

The first experiment explores the magnetic response and fluxoid transitions of superconducting, mesoscopic bilayer aluminum rings in the presence of two coupled order parameters arising from the layered structure. For intermediate couplings, metastable states that have different phase winding numbers around the ring in each of the two order parameters were observed. Larger coupling locks the relative phase, so that the two order parameters are only manifest in the temperature dependence of the response. With increasing proximitization, this signature gradually disappears. The data can be described with a two-order-parameter Ginzburg-Landau theory.

The second experiment concentrates on fluxoid transitions in similar, but single-layer rings. Near the critical temperature, the transitions, which are induced by applying a flux to the ring, only admit a single fluxoid at a time. At lower temperatures, several fluxoids enter or leave at once, and the final state approaches the ground state. Currently available theoretical frameworks cannot quantitatively explain the data. Heating and quasiparticle diffusion are likely important for a quantitative understanding of this experiment, which could provide a model system for studying the nonlinear dynamics of superconductors far from equilibrium.

The third and most important scanning SQUID study concerns 33 individual mesoscopic gold rings. All measured rings show a paramagnetic linear susceptibility and a poorly understood anomaly around zero field, both of which are likely to unpaired defect spins. The response of sufficiently small rings also has a component

that is periodic in the flux through the ring, with a period close to h/e. Its amplitude varies in sign and magnitude from ring to ring, and its typical value and temperature dependence agree with predictions for persistent currents in diffusive metal rings.

In addition to the above three experiments, a scanning Hall probe study of the magnetic superconductor $ErNi_2B_2C$ and related theoretical results on the magnetic fields above a superconductor with internal magnetism are discussed. In this experiment, a scanning Hall probe microscope was used to image $ErNi_2B_2C$ in the superconducting, antiferromagnetic, and weakly ferromagnetic regimes. It is shown that isolated vortices spontaneously rearrange on cooling through the antiferromagnetic transition temperature $T_N = 6$ K to pin on twin boundaries, forming a striped pattern. In the ferromagnetic phase below $T_{WFM} = 2.3$ K, a weak, random magnetic signal appears, but no spontaneous vortex lattice is present down to 1.9 K. This indicates that ferromagnetism coexists with superconductivity by forming small, subpenetration depth ferromagnetic domains. The interpretation of this experiment is supported with extensive modeling of the magnetic fields above the surface of a superconductor with an intrinsic magnetization. Solutions for various magnetic domain boundary configurations and relations between the spectral densities of the magnetization and the resulting field are derived. The latter are useful if the magnetization varies randomly. These results were also applied to existing data from scanning experiments on Sr_2RuO_4, leading to the conclusion that a chiral domain wall would have been detectable, but small random domains and defects may have been undetectable at the experimental noise level.

Acknowledgements

First of all, I would like to thank Kam Moler. She has been a great advisor not only for her professional and scientific mentorship, but also because she never forgot that science is done by human beings which have certain needs beyond results and a career. I have benefited very much from the freedom and independence she has allowed me, while always knowing that I could count on her support when needed. Furthermore, she deserves some credit for assembling a bunch of wonderful people in her group. Nick has been both a friend and a tremendous shielded-room mate. He has enriched my life by sharing my passion for physics and the ups and downs in the life of an experimentalist. Working with him has certainly pushed the balance between inspiration and transpiration in the right direction. Since our junior Julie joined the team, she has also been a very helpful hand.

I could hardly imagine better colleagues than my contemporaries in the group - Nick, Ophir, Lan, Cliff, Rafael and Jenny. Over the years, we have shared many late night discussions, sailing trips, bike rides, and many other activities. I would also like to thank Per, Brian and Janice from the former generation of students, who taught me many of the dirty details of cryogenic experiments.

Over the years, life in our lab has been enriched by several long term visitors: Yoshi Maeno, John Kirtley, Eli Zeldov, Yuval Oreg and Martin Huber, who also enabled most of the experiments in this thesis by making and providing the SQUID sensors.

Work at Stanford would not have been the same without the very open and supportive environment of the McCullough basement, particular from the KGB and

Goldhaber-Gordon groups. I often felt we formed some kind of grand canonical ensemble, certainly in terms of equipments, but sometimes also with respect to students fluctuating from one lab to the other. In the early stages of my graduate work, I also had a very productive and enjoyable collaboration with the Fisher group.

My parents Manfred and Gudrun deserve far too many credits to mention them all. Together with my grand parents Georg and Ilse, they have laid the foundation for my career as a physicist through a very stimulating childhood. They have always supported and fostered my ambitions, even if it meant only that we could only see each other after traveling around a quarter of the globe - which they did quite a few times.

Finally, I would like to thank my girlfriend Anna, who has given me a good reason and a place to escape from experiments every know and then.

Contents

List of Tables

List of Figures

Chapter 1

Outline

This outline mainly serves as a guide to the contents of this thesis. Since the different parts are mostly self contained and to a large extend reformatted version of published papers with their own introductory paragraphs, the reader is referred to the individual chapters for introduction to the respective subject matters. As part of the the reformatting, I have updated references and replaced those to papers contained in this thesis with the corresponding section. Appendix A lists the definitions of most variables used in this thesis.

The driving force for the development of the scanning SQUID technique employed in most of the experiments reported here was the study of persistent currents in normal metal rings discussed in chapter 5, which I consider the most important outcome of my graduate work. The core of the experimental results is discussed in section 5.3, which is a paper draft written in PRL style. Since measurements for this project are still in progress the time of writing, this draft will see some revision before publication.

Some supporting data and the backaction of the SQUID will be discussed in section 5.4. Section 5.1 gives a brief introduction to the physics of persistent current and an overview of the most important theoretical results. Previous experimental findings on persistent currents are summarized in section 5.2.

Chapter 2 deals with some aspects of the scanning SQUID microscope used for the ring experiments in chapters 3, 4 and 5. The design, modeling and testing of the cryogenic RF filters are described in section 2.1, a reproduction of a paper submitted

to Review of Scientific Instruments. Section 2.2 covers the thermal properties of the scanner and filter assembly. Its contents are relatively straightforward, but I have included it because the problem of running a current of several tens of mA to the mixing chamber of a dilution refrigerator seems somewhat nonstandard, so that it might be a useful resource. I do not discuss the design of the scanner in the other hand, since part of it has been adopted from my predecessor Per Björnsson, and it is more or less self explanatory with drawings or the actual scanner at hand.

Chapters 3 and 4 describe two experiments on superconducting aluminum rings. Those experiments, neither of which were planned beforehand, are by-products of our effort to measure the response of superconducting rings in the fluctuation regime [78]. Once discovered, the observed effects were interesting enough to deserve further study. The first experiment deals with the magnetic response in the presence of two order parameters. The main body, which was published in Physical Review Letters, is contained in section 3.1. Sections 3.2 discusses the fit procedures and results and is a reproduction of an EPAPS document relating to the main paper. Section 3.3 presents some additional, unpublished data which further illustrate and support the reported observation of states with two different phase winding numbers in each of the components. It also touches upon the clarification of the results of Ref. [131], some aspects of which are at best rather unclear.

The above three experiments are closely related both conceptually and in terms of the technique. Each of them consists of measurements of the magnetic response of mesoscopic rings fabricated from elemental metals, using a scanning SQUID microscope. Differences between them are the sample material, in particular the strength of electron interactions which cause superconductivity in the aluminum rings, the temperature range explored, and the specific question addressed by each experiment. The remaining two chapters may seem more or less unrelated to the rest of this thesis. They discuss a scanning Hall probe experiment on the magnetic superconductor $ErNi_2B_2C$ (chapter 6) and a technique to compute the magnetic fields above the surface of a magnetic superconductor (chapter 7), which I developed for the interpretation of the data in chapter 6. However, they are conceptually related to the two-order-parameter effects discussed in chapter 3. Both experiments address the

interplay between two different order parameters. An additional connection can be made through the spin-triple superconductor Sr_2RuO_4, which is thought to have internal magnetism due to its $p_x + ip_y$ two-component order parameter. On the one hand, chapter 7 includes an estimate of the fields outside the sample generated by chiral currents expected in this material. On the other hand, Sr_2RuO_4 might allow fractional vortices, which are topologically equivalent to the states with two different phase winding numbers observed in the two-order-parameter aluminum rings of chapter 3. The insight gained from that experiment was the basis of my contribution to a theory paper on the prospects of finding fractional vortices in Sr_2RuO_4 [37].

The scanning SQUID microscope and the dilution refrigerator used for the experiments in chapters 3, 4 and 5 was originally designed and implemented by Per Björnsson. My main improvements of the instrument consist of the addition of a coarse motion stage, and the development of the cryogenic filters described in section 2.1. Nick Koshnick and I also enhanced the ability to apply large currents and the background rejection and noise performance of the SQUID susceptometry technique. The SQUIDs were designed and fabricated by Martin Huber. I have written nearly all the programs used to take, analyze and model the data from the three scanning SQUID experiments. Nick Koshnick carried out a large part of the fabrication of the superconducting ring samples reported in chapters 3 and 4. He also contributed an approximately equal share of data taking and preparation to those experiments, but I have done most of the work related to data analysis and interpretation and all the modeling. The work for the measurements on normal rings was mostly my own, with support from Nick Koshnick and Julie Bert. The scanning Hall probe experiments on $ErNi_2B_2C$ of chapter 6 were carried out by myself on an instrument that was set up by Janice Guikema. The samples were grown and characterized by Suchitra Sebastian. Chapter 7 is entirely my own work.

Chapter 2

Instrument design aspects

2.1 Cryogenic RF-Filters with zero dc-resistance

Hendrik Bluhm, Kathryn A. Moler,
submitted to Review of Scientific Instruments.

Abstract

The authors designed, implemented and tested cryogenic RF filters with zero DC resistance, based on wires with a superconducting core inside a resistive sheath. The superconducting core allows low frequency currents to pass with negligible dissipation. Signals above the cutoff frequency are dissipated in the resistive part due to their small skin depth. The filters consist of twisted wire pairs shielded with copper tape. Above approximately 1 GHz, the attenuation is exponential in $\sqrt{\omega}$, as typical for skin depth based RF filters. By using additional capacitors of 10 nF per line, an attenuation of at least 45 dB above 10 MHz can be obtained. Thus, one single filter stage kept at mixing chamber temperature in a dilution refrigerator is sufficient to attenuate room temperature black body radiation to levels corresponding to 10 mK above about 10 MHz.

2.1.1 Introduction

Many cryogenic experiments involve electronic transport measurements, which typically require leads connecting the sample to room temperature instrumentation. Without appropriate filtering, those electrical connections will also transmit parasitic signals to the sample. Many samples are very sensitive to such disturbances, especially when the relevant energy scales are in the milli-Kelvin region and the devices are small. The effect of extrinsic noise, which can be either anthropogenic or thermal from higher temperature sources, can simply be to heat the electrons in the sample above the lattice temperature. Because of their small volume, mesoscopic devices are particularly sensitive to even very small amounts of power [69]. In some experiments, such as SET-based devices or solid state qubits, microwave radiation may directly affect the quantum dynamics under study through effects like photon assisted tunneling [91] or excess dephasing [15].

To mitigate these undesirable effects, it is crucial that electrical connections to the sample be filtered sufficiently [19]. With an increasing number of experimentalists exploring quantum physics at the nano scale, there is a growing need for simple filtering solutions. We present here a filter design similar to the one in Ref. [128], but with a DC resistance limited only by contact resistances. It allows us to supply currents on the order of 50 mA to the mixing chamber of a dilution refrigerator while maintaining a respectable base temperature. In our case, such large currents are required in order to locally apply a magnetic field using a micron scale field coil integrated in a scanning SQUID susceptometer [17], intended primarily for magnetic response measurements on mesoscopic samples [22, 78]. Similar requirements also occur for flux bias lines of superconducting qubits. Most flux biased qubit experiments currently employ a conventional superconducting magnet, but the individual tuning of several qubits in a well shielded environment [110] is only achievable with locally generated fields.

The vanishing DC resistance of our filters is achieved by using composite wires with a superconducting core surrounded by resistive material, which are wrapped in copper tape to form a lossy transmission line. At DC, all the current is flowing in the superconducting core, so that there is no dissipation. At higher frequencies,

the skin effect restricts the current flow to the resistive part, so that once the skin depth δ is smaller than the thickness of the resistive sheath, the dissipation quickly approaches that of a purely resistive conductor. The low frequency attenuation is increased by adding two discrete capacitors to ground along each line. At frequencies below the intrinsic inverse RC time of the transmission line, those capacitors together with the frequency-dependent resistance of the transmission line act as a 2-pole RC filter. When they become ineffective above their self resonance, the attenuation is entirely due to the transmission line. Since some of our wires can tolerate a larger resistance, we have also implemented filters with purely resistive wires, which allowed us to reduce their length.

Our filters provide an attenuation of at least 45 dB above 10 MHz and reach 120 dB at 500 MHz, with a strong extrapolated increase at higher frequencies. This attenuation exceeds the ratio of the photonic spectral density $S_E(\omega, T) = \hbar\omega/(\exp(\hbar\omega/k_B T) - 1)$ at room temperature to that at 10 mK above $f = \omega/2\pi = 10$ MHz (See fig. 2.4). Thus, it is sufficient to use a single filter stage. As any dissipative circuit element, including filters, emits thermal radiation, it has to be kept at the base temperature of the cryostat. Filters for nine resistive and six superconducting twisted wire pairs inside the copper tape shield fit into a cylindrical space with a diameter of 80 mm and a height of 120 mm. If required, additional filtering to eliminate extrinsic radiation can be added at room temperature, for example at a shielded room feedthrough or cryostat breakout box.

The remainder of this paper is organized as follows: After briefly describing filtering concepts that have appeared in the literature so far in section 2.1.2, we discuss the physical implementation of our design in section 2.1.3. A model for the filter is developed in sec ion 2.1.4, followed by test result in section 2.1.5.

2.1.2 Conventional filtering strategies

This section will give a brief overview of different filtering strategies suitable for cryogenic applications. A more detailed review can be found in Ref. [19]. Commercially

available reflective filters such as pi-filters are a convenient choice for filtering technical noise at room temperature. However, impedance mismatches in the connected lines may cause resonances which severely compromise their performance, and combining several stages to achieve a high attenuation may not have the desired result. If they are to be used at cryogenic temperatures, one should keep in mind that the properties of some models may change dramatically at low T.

Simple RC filters may be quite useful for low to intermediate frequencies if a large resistance (and/or capacitance) can be tolerated. At microwave frequencies, parasitic inductances and capacitances of the lumped elements tend to limit their performance, in contrast to copper powder or transmission line filters which typically feature a very strong attentions above about 1 GHz. Copper powder filters are the classic design for low temperature applications, first reported in Ref. [90] and further optimized in reference Ref. [52]. They are based on the dissipation of energy by high frequency stray fields through eddy currents. Since copper powder filters are usually made with a single wire, they are more convenient for coaxial cables than for twisted pairs. Due to the high cutoff frequency (e.g. 15 dB at 100 MHz) [19], a combination with an RC or LC stage is often necessary. Ref. [97] reports a variant with superconducting wire, which shows a similar attenuation as our filters if configured as pi-filters.

Over the last decade, various versions of dissipative transmission lines have been used as filters. Some of them are essentially resistive coaxial cables [146]. Vion *et al.*[136] have developed a relatively compact lithographic implementation. More recently, the Schoelkopf group reported a very flexible and low cost version based on resistive wire wrapped in copper tape, [128] which underlies the approach described here. Our modifications of this design are primarily the use of wire with a superconducting core, which eliminates the undesired dc resistance, and the addition of discrete capacitors for increased attenuation at intermediate frequencies. With the exception of Vion's compact filters, the above transmission line filters rely on the skin effect, which confines AC magnetic fields and therefore currents in a conductor with resistivity ρ to one skin depths $\delta = \sqrt{2\rho/\mu_0\omega}$ below the surface. Due to this constriction of the current flow, the resistance increases as $\sqrt{\omega}$, leading to an attenuation of the form $\exp(-\sqrt{\omega/\omega_0})$.

2.1.3 Physical implementation

The transmission line part of our filters consists of "copper tape worms" as described in Ref. [128]. Three twisted pairs are arranged in parallel and wrapped in copper tape, which forms the outer conductor of the transmission line and shields the signal carrying wires. Our first tape worm generation was sealed by soldering along the seams as indicated in Fig. 2.1 in order to achieve optimal RF tightness. However, the soldering process appeared to degrade the wire insulation, which caused frequent shorts to the copper tape or between the wires. Furthermore, unavoidable thickness variations of the solder seam lead to sharp kinks at the thinnest spots which sometimes caused the copper tape to break. To avoid these problems, we eliminated the soldering step in a second generation. To maintain an acceptable RF tightness without soldering, it is crucial to have a large overlap along the seams. The width of the unsoldered filter ribbon ($\approx$ 8 mm) was about one third of that of the tape used, so that the overlap extended over the full ribbon width. The test results reported in Sec. 2.1.5 are from a prototype filter of the first generation.

We used 3M copper tape with non-conductive adhesive (type 1194). The conductive-adhesive variety (1181) is unsuitable because its adhesive contains small metal spikes that can penetrate the wire insulation. Since even some tape rolls with nominally non-conductive adhesive tend to be contaminated with such spikes, the tape should be checked carefully under a microscope and discarded if any spikes appear.

The wire used for the superconducting filters is a customized version of persistent current switch wire purchased from Supercon Inc. The 0.05 mm diameter superconducting core is made of NbTi and the resistive outer part of $Cu_{70}Ni_{30}$, with a resistivity of 38.5 $\mu\Omega$m. To obtain a sufficient resistance at 10 MHz, we chose a total outer wire diameter of 0.2 mm. The wire insulation is 15 μm thick Formvar. The non-superconducting filters were made of 37 AWG Stablohm 800 wire, which has a resistivity of 132 $\mu\Omega$cm. Their insulation has a thickness of 6 μm and 16 μm for the first and second generation, respectively. The thinner insulation was chosen initially to maximize the capacitance between the wire and the tape, but then replaced in order to reduce the likelihood of shorts.

To increase the attenuation between about 10 and 100 MHz, we connected 5.1

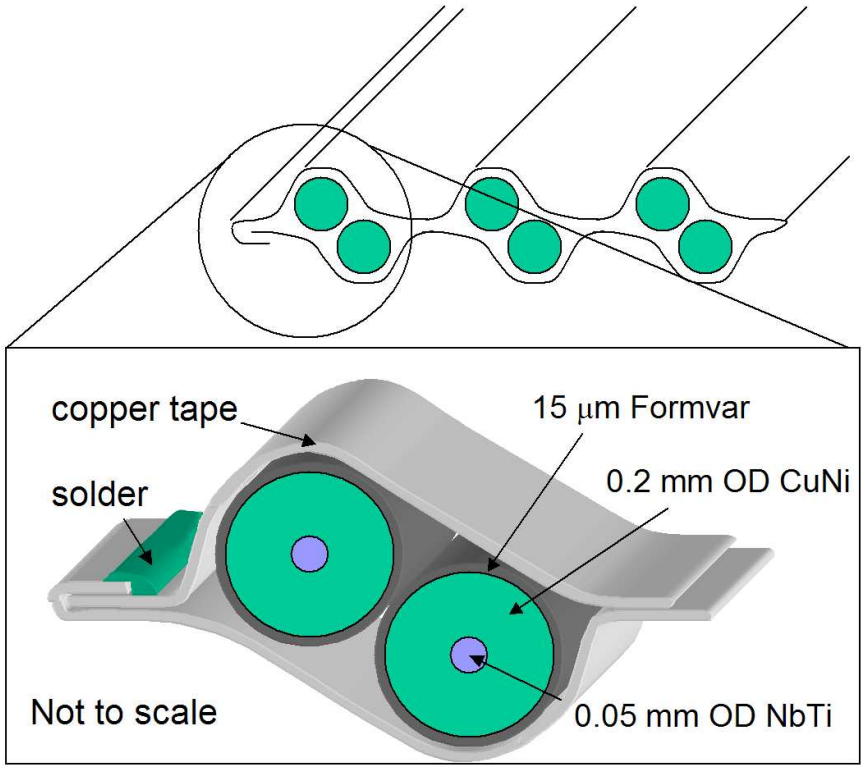

Figure 2.1: Schematic cross section of a copper tape worm of the first generation, with a soldered seam. The width of a ribbon with three twisted pairs is about 8 mm.

nF capacitors form the 700B series manufactured by American Technical Ceramics Inc. (ATC) between each filter wire and the shield, one quarter of the total filter length from each end. Those high quality RF capacitors are very compact (approximately 2.8 mm cubes) and have a high self resonance of 100 MHz and a negligible temperature dependence. They were placed in 20 mm long boxes made of 3/16" square brass profile. The ends of these filter housings were closed by soldering in matching brass plugs with a hole to feed through the wires. One contact of the capacitors was directly glued onto those plugs using Epotek H20E conductive epoxy. In the first generation, the copper tape shield was soldered directly into the holes of the end plugs. These direct connections were replaced by short adapter pieces made of 1/16" brass tubing for improved mechanical stability in the second generation. In order to protect the wire from excessive heating and sharp metal corners, the part inside the brass tubing

was threaded through Teflon tubing. The same techniques were used to connect the tape worm to copper parts used as feedthroughs towards the sample area. To avoid vacuum problems, the capacitor boxes were filled with Stycast 1266 through small holes, which were later electrically sealed with silver epoxy.

The superconducting filters are about 4 m long. Due to their larger resistance, 2 m are enough for the resistive version. They were accommodated in our dilution refrigerator by coiling them around an OFHC copper support below the mixing chamber. For 2 m of filter ribbon with three twisted pairs, this requires a height of about 1.5 cm and a diameter of about 8 cm, including the space for the capacitors. Fig. 2.2 shows a partially assembled superconducting filter consisting of two such coils. For good thermal contacts, the filters were clamped between machined copper parts with groves to accommodate the wires. It is important not to apply pressure to the latter to avoid shorts.

After elimination of initial problems with frequent shorts, the filters turned out to be reliable over several cooldowns. Some of them were operated at voltages of more than ± 180 V w.r.t. ground, i.e. 360 V between the wires of a pair. However, they tend to suffer from dunking in liquid nitrogen, as some liquid enters the tape worm and forces it apart when expanding upon warming up.

2.1.4 Modeling

Approximate analysis

Although the model discussed in section 2.1.4 provides a fairly accurate quantitative description, the simplified analysis of this section is useful in order to better understand the significance of the different model parameters and as a rough tool for preliminary design work. In the following, C and L denote the capacitance and inductance per unit length of the transmission line.

The dissipation in the resistive material becomes significant once the skin depth $\delta = \sqrt{2\rho/\mu_0\omega}$ becomes of order or smaller than the thickness $r_i - r_c$, where r_i and r_c are the radius if the inner conductor and its superconducting core, respectively. Above this cutoff, the current flows within a layer of thickness δ below the surface,

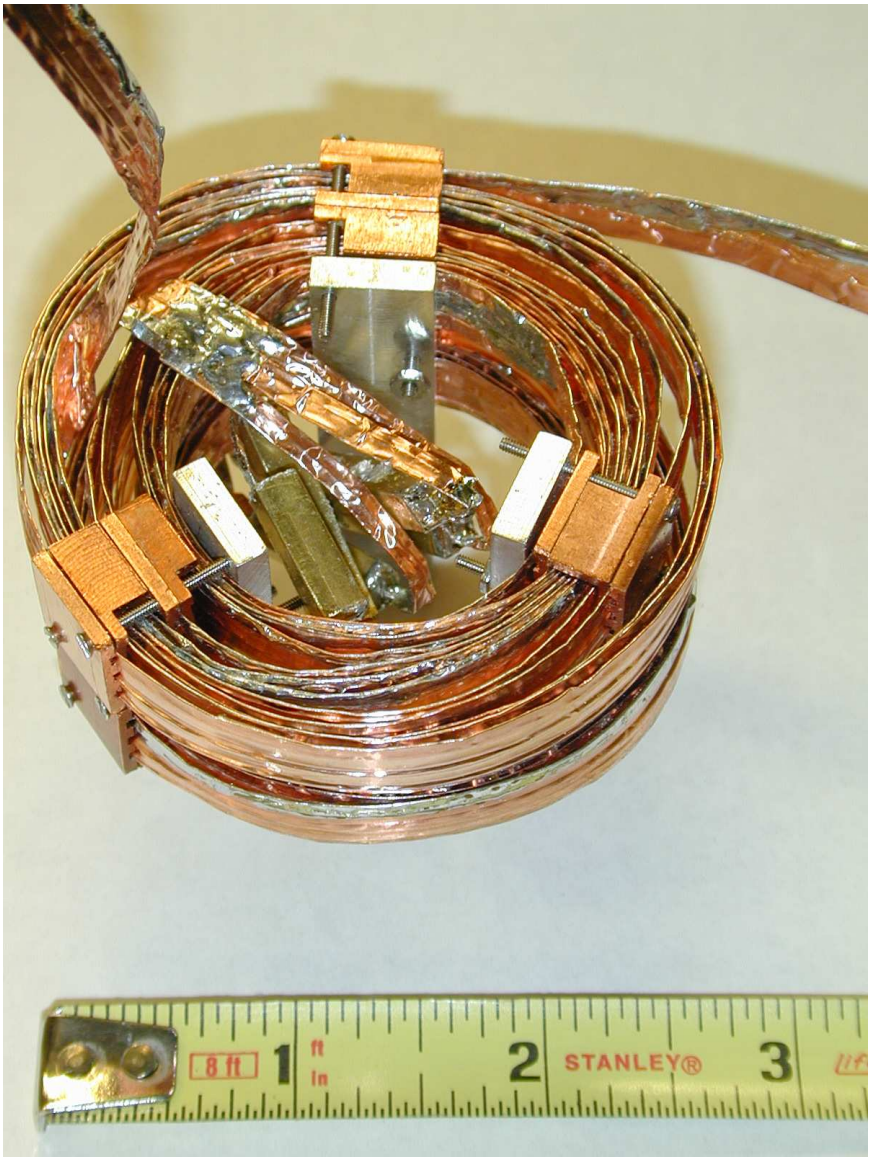

Figure 2.2: Partially assembled superconducting filter. When fully assembled, several such filters are stacked and the aluminum bars shown in the picture replaced by long copper bars connecting the filters. The brass parts in the center accommodate the capacitors.

so that the frequency dependent resistance per unit length is $R(\omega) \approx \rho/2\pi r_i\delta = (1/2\pi r_i)\sqrt{\omega\rho\mu_0/2}$.

At frequencies where the discrete capacitors are dominant, their time constant $R(\omega)C$ needs to be as large as possible for strong attenuation. The value of the capacitors is limited by availability and size considerations. $R(\omega)$ is at first glance proportional to $\sqrt{\rho}$, however the wire thickness $2r_i$ required to force the current into the resistive sheath also increases as $\sqrt{\rho}$, so that not much would be gained from a higher resistivity.

For the chosen type of wire, the cutoff frequency according to the above criterion is $\mu_0\rho(r_i - r_c)^2/2 = 17$ MHz. The resistance at cutoff is about $\rho/\pi r_i^2 = 12\ \Omega$/m, giving an RC roll off frequency of 1.3 MHz. Thus, one can expect a significant attenuation at cutoff. (Note that the resistance *at* 1.3 MHz is much smaller though.)

For a 2-pole RC filter with $R \propto \sqrt{\omega}$, one obtains a roll off of 60 dB/decade. This will provide sufficient attenuation up to the capacitor self resonance at 100 MHz. At larger frequencies, the transmission line needs to provide all the attenuation. We first derive a simple expression for its performance.

In a transmission line with perfect conductors and a homogeneous dielectric with relative permittivity ϵ_r, the relation between the electric and magnetic fields of a TEM mode [65] imply that $LC = \epsilon_r/c^2$, with c denoting the speed of light in vacuum. Thus, the line impedance $Z_0 = \sqrt{L/C}$ is given by $Z_0 = \sqrt{\epsilon_r}/Cc$. [1] With I, P and V denoting the current, power and voltage of a forward propagating mode in the line, the power loss per unit length is $dP/dx = RI^2 = RIV/Z_0 = (R/Z_0)P$. Integrating this along the transmission line gives a power attenuation of e^{-lR/Z_0}, where l is the total length. Since $Z_0 \propto 1/C$ as explained above, we thus have to maximize the RC constant of the line. As the capacitance is proportional to the area over which the wire faces the shield and R is the surface impedance divided by the wire circumference, the RC product is approximately independent of the wire

[1] This is valid in as long as the field penetrating the conductor does not contribute significantly to the inductance, which holds if $\delta \ll r_o - r_i$, i.e. above about 300 MHz where $\delta = 20\ \mu$m. At lower frequencies, about one skin depth of the resistive material acts as "dielectric" with infinite ϵ_r. It contributes to L, but does not reduce C below the value determined by the insulator because only magnetic, but no radial electric fields can penetrate the conductor.

diameter. However, $R(\omega) \propto \sqrt{\rho}$, so that a high resistivity is desirable, as long as $r_i - r_c$ is adapted accordingly.

Model for a coaxial geometry

We now turn to the more accurate model that we used to fit the test results. The copper tape worm sections are modeled as a dissipative transmission line with a frequency dependent resistance per unit length, $R(\omega)$. According to the standard transmission line model [112], the local voltage between the two conductors, $V(x)$, and the longitudinal current, $I(x)$, are related by $V(x) = V_0 e^{\pm\gamma(\omega)x}$ and $V(x) = \pm Z_0(\omega) I(x)$. The propagation coefficient γ and line impedance Z_0 are given by

$$\gamma(\omega) = \sqrt{i\omega C(i\omega L + R)} \quad \text{and} \tag{2.1}$$

$$Z_0(\omega) = \sqrt{\frac{i\omega L + R}{i\omega C}}. \tag{2.2}$$

To compute the frequency dependence of $R(\omega)$, the skin effect and the presence of the superconducting core have to be taken into account. In order to avoid a numerical computation of the fields inside the transmission line, we first consider a circular coaxial geometry with a composite inner conductor of outer radius r_i, which has a superconducting core of radius r_c. r_o denotes the inner radius of the outer conductor. The dielectric between the conductors is assumed to have a homogeneous relative dielectric constant ϵ_r. As the resistivity of the copper shield is much smaller than that of the wire, its resistance will be neglected for simplicity in the following. For this geometry, $C = 2\pi\epsilon_r\epsilon_0 \log(r_o/r_i)$ and $L = 2\pi\mu_0 \log(r_o/r_i)$. $R(\omega)$ is the ratio between the longitudinal electric field at the surface of the inner conductor, $E_x(r_i)$, and the total current I. Now $I = \oint \vec{B} \cdot d\vec{s} = 2\pi r_i B_\phi(r_i)$ and $E_x(r_i) = \rho j_x(r_i) = (\rho/\mu_0)(\nabla \times \vec{B})_x = (\rho/\mu_0 r)\partial(rB_\phi(r))/\partial r$, so that we get:

$$R(\omega) = \frac{\rho}{\mu_0 2\pi r_i^2} \frac{\frac{\partial}{\partial r}|_{r=r_i}(rB_\phi)}{B_\phi(r_i)}. \tag{2.3}$$

To evaluate Eq. (2.3), we compute $B_\phi(r)$ as a solution of $\nabla^2 B + 2i/\delta^2 B = 0$. In cylindrical coordinates with $\vec{B} = B_\phi(r)\hat{e}_\phi$, this equation reduces to

$$\frac{\partial}{\partial r}\left(\frac{1}{r}\frac{\partial}{\partial r}(rB(r))\right) + 2i/\delta^2 B(r) = 0.$$

The solutions are first order Bessel functions of the first and second kind $J_1(\alpha r)$ and $Y_1(\alpha r)$ with $\alpha = -(1-i)/\delta$. Y_1 diverges for $r \to 0$ while J_1 is regular there but diverges for $r \to \infty$. Thus the solution for a homogeneous resistive wire would be $B_\phi(r) = B_\phi(r_i)J_1(\alpha r)/J_1(\alpha r_i)$, For the wire with a superconducting core, the boundary condition at the interface is

$$E_x(r_c) = \rho j_x(r_c) = \frac{\rho}{\mu_0 r}\frac{\partial}{\partial r}|_{r=r_c}(rB_\phi(r)) = 0.$$

Together with a given value for $B_\phi(r_i)$, this determines the coefficients of the two solutions. To evaluate the radial derivative, it is useful to note that $\partial J_1(\alpha r)/\partial r = (\alpha/2)(J_0(\alpha r) - J_2(\alpha r))$. The same holds for Y_1. Note that this procedure automatically takes the contribution of the magnetic field inside the resistive material to the total inductance into account. It is manifest in the imaginary part of $R(\omega)$.

The approximations made here are valid as long as the longitudinal electric fields in the dielectric are much smaller than the radial field and the radial current densities are much smaller than the longitudinal ones. The largest expected attenuation is on the order of 1 dB/cm in the GHz range, so that the characteristic length scale over which the amplitude changes significantly along the propagation direction is about 10 cm. Comparing this to the sub-mm radial length scale shows that the above condition holds well over the full frequency range under consideration.

To compute the S-matrix of a complete filter with capacitors to ground whose self resonance is modeled through a series inductance, we use the $ABCD$-matrix formalism [112, 128]. The result is compared to measured S-parameters in Sec. 2.1.5.

Effect of twisted pair geometry

Due to the three-conductor geometry, there are two TEM modes. By symmetry, one is a common mode for which both wires have the same potential with respect to the shield, and the other one a differential mode with opposite voltages on each wire. Only the common mode can be measured using standard microwave equipment typically featuring coaxial connectors. In this case, the twisted pair can be treated as one single conductor.

Lacking exact knowledge of the cross section geometry, the capacitance and inductance per unit length, C and L, cannot be calculated accurately and must be extracted from measurements. Thus, only the resistance $R(\omega)$ needs to be considered in order to transfer the model derived for coaxial lines to this common mode. At low frequencies, where $\delta \gg r_i$, Eq. (2.3) reduces to the DC resistance of the wire. A twisted pair without superconducting cores would trivially have half the resistance of a single wire. In the opposite limit ($\delta \ll r_i$), the factor $2\pi r_i$ in Eq. (2.3) must be replaced by the active circumference over which the wire surface is adjacent to the shield. The inner region, where the two wires face each other, will essentially be field free and thus contribute little to the conductance, leading to a correction factor slightly smaller than unity. Hence, one would expect the resistance of the pair to be up to a factor 1/2 smaller than that of a single wire, with the largest corrections occurring at low frequency. We have incorporated this into the model by multiplying $R(\omega)$ as obtained from the known geometry and resistivity by a correction factor α.

As only the common mode can be tested properly, the attenuation of the differential mode needs to be estimated. It is convenient to define all parameters for the differential mode with respect to the voltage between one wire and the ground shield. First, we consider C and L corresponding to this mode. If the symmetry plane between the two wires were replaced by a perfect conductor, the same boundary conditions would arise: by symmetry, the electric field must be normal to it and the magnetic field parallel. (The charge and current on the second wire can simply be considered as images of the first enforcing the boundary conditions on the hypothetical conductor.) Since the copper tape shield is also modeled as a perfect conductor,

the differential mode should therefore have very similar parameters as the coaxial geometry. Now the capacitance C is approximately proportional to the area over which the wire surface faces the ground conductor, while the inductance L and resistance $R(\omega)$ are inversely proportional to it. (This is the origin of the factor $2\pi r_i$ in equation 2.3). Thus, the product determining the propagation coefficient of the transmission line [Eq. (2.1)] remains unchanged compared to the common mode. Only the line impedance Z_0 will be affected. A more intuitive explanation of this argument is that the common mode simply has a different effective area between the two conductors.

At frequencies where the discrete capacitors are important, the situation for the differential mode is slightly less favorable. As there is now only one rather than two parallel capacitors between the wire and shield, the capacitance seen by the propagating wave is simply half as large as for the common mode. The correction factor α on the other hand will be close to unity, but was larger than 0.5 for the common mode as explained above. Thus, one can expect the RC-time constant to decrease by about 20 – 30 %. Due to the increase of of $R(\omega)$ with higher frequency, the roll off frequency will change less than that.

2.1.5 Test results

We tested a complete prototype filter and shorter copper tape worms without additional capacitors by soldering them to copper blocks fitted with SMA connectors. Both wires were connected to the center pin so that we measured the common mode transmission. The characterization from 50 MHz to 20 GHz was carried out using a HP 8510 vector network analyzer. Below 20 MHz, we used a sine wave generator and a digital oscilloscope. All measurements were performed in a 50 Ω environment. Additionally, we measured the capacitance per unit length at kHz frequencies using a capacitance bridge. For the common and differential modes, respectively, we obtained 0.61 nF/m and 0.23 nF/m. The latter value was measured between the two wires with a floating shield so that it has to be doubled to conform with the definition form section 2.1.4. The ratio of $0.61/0.46 = 1.3$ is just the ratio of the effective areas, corresponding to a correction $\alpha = 1/1.3 = 0.77$ for the common mode resistance

compared to the coax geometry.

Fig. 2.3 shows the result of the low frequency measurements at 300 K and 4 K and the corresponding models, for which we used $\alpha = 0.65$. As expected, $\alpha = 0.5$ slightly improves the agreement between model and data at low frequencies. The peak in the 4 K data around 3 MHz is due to a resonance caused by the discrete capacitors and the inductance of the transmission line.

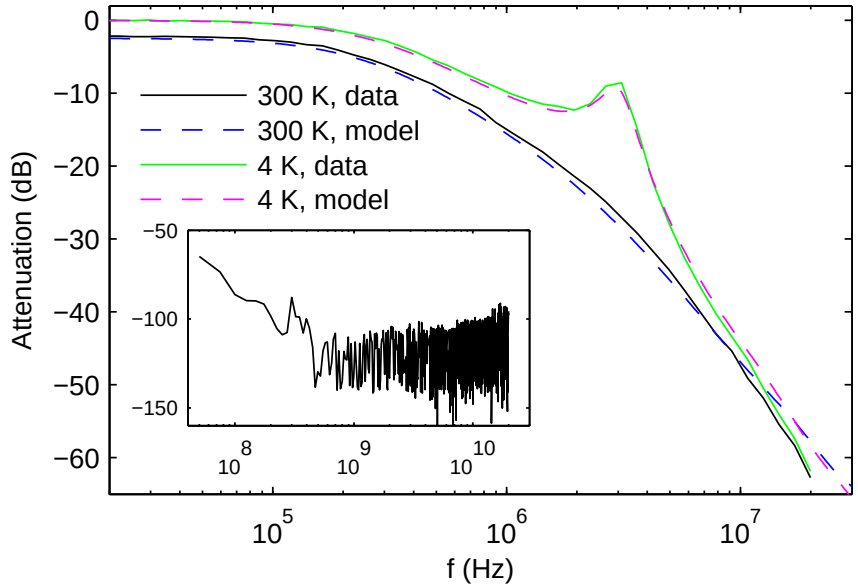

Figure 2.3: Insertion loss of a filter prototype in a 50 Ω line at low frequencies at 300 K and at 4 K with a superconducting core. Below the roll off, the 4 K data shows negligible dissipation. Above 10 MHz, the two measured curves collapse. The peak in the 4 K data is due to an LC resonance of the capacitors and the line inductance. The inset shows the attenuation from 50 MHz to 20 GHz at room temperature. Above about 500 MHz, the signal disappears in the noise floor of the network analyzer.

As can be seen in the inset of figure 2.3, measurements of the complete filter are not very revealing at higher frequencies because the signal disappears in the noise floor of the network analyzer. To extrapolate the filter performance, we measured two shorter tape worm pieces of length $l = 52$ and 88 cm without additional capacitors (Fig. 2.4). Scaling the result to $l = 4$ m, assuming that the attenuation is exponential

in the lengths, shows that the two curves collapse reasonably well. The parameters for the model of a 4 m tape worm without capacitors were adjusted to obtain a good agreement with the data up to 1 GHz. The resulting capacitance of $C = 0.55$ nF/m. is in reasonable agreement with the value of 0.61 nF/m obtained from the bridge measurement. The ripple in the data at sub GHz frequencies is due to resonances in the transmission line caused by the impedance mismatch between the filter and the 50 Ω environment. They can be fit quite well with a model using the actual worm length, but they naturally do not appear in the model for $l = 4$ m.

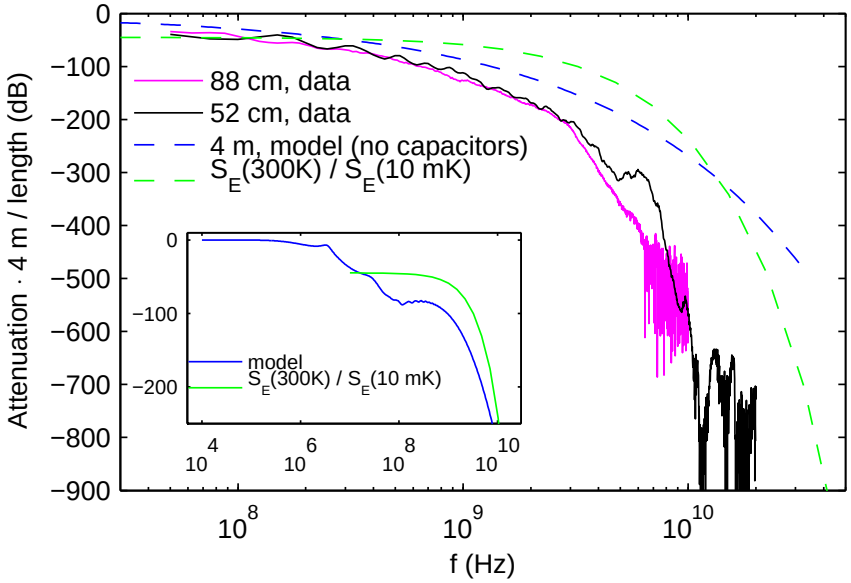

Figure 2.4: Insertion loss of short test pieces without discrete capacitors in a 50 Ω line at room temperature. The data has been scaled to a total length of 4 m assuming that the attenuation (i.e. $|S_{21}|$) decays exponentially with increasing length. The data from two pieces of different length collapses well and shows a significantly higher attenuation than the model for a 4 m long line whose parameters have been chosen to match the scaled data below about 1 GHz. The inset shows the model for the complete filter using the parameters extracted from measurements. The ratio of the bosonic spectral densities at 300 K and 10 mK for $f > 10$ MHz is shown for comparison in both plots.

From the measured heat load due to a quasi-DC current running through a finished

superconducting filter, we can set an upper limit of 3 mΩ on its resistance, with a negligible increase of the dissipated power up to 1 kHz. Since this value includes solder joint resistances outside the filter, its actual resistance is most likely lower.

2.1.6 Concluding remarks

There are a number of points that may have an effect on the filtering performance which we have not checked in detail, or which were changed after testing the prototype. Amongst those is the effect of using Silver epoxy rather than solder to connect wires and seal holes for epoxy injection. It is also likely that the RF tightness of unsoldered tape worm version is inferior compared to the one with the seam sealed by soldering. Due to aging of the tape adhesive and a resulting reduction of the capacitance between the wires and the shield, the filtering performance may degrade after thermal cycling. For the resistive version, we have relied on an adaptation of the model from Sec. 2.1.4 without extensive testing.

Although the design discussed here is seemingly simple, its development and implementation has taken several month of graduate student time, partly due to shorts in the first filter generation and the resulting need to modify the design. On the other hand, the construction of a complete filter was a matter of days once the procedures were finalized. Eliminating the capacitor boxes would make the implementation significantly simpler.

Acknowledgments

This work was supported primarily by the National Science Foundation under Grant No. DMR-0507931, and by the Department of Energy under Contract No. DE-AC02-76SF00515. We would like to thank Ron Potok for useful discussion and Rob Schoelkopf for providing Ref. [128] before publication.

2.2 Thermal engineering

2.2.1 Field coil supply lines

Since a heat load as low as 2.5 μW can raise the base temperature of our dilution refrigerator from 13 to 25 mK, and the field coils of the SQUID need to be supplied with currents of up to 80 mA, it is crucial to keep the resistance in the field coil supply lines to a minimum. At a typical 40 mA amplitude AC operating current, the power dissipated in a 1 mΩ resistance is 0.8 μW!

In order to determine the feasibility of a mΩ connection and to identify the most important contributions to the total resistance, I measured the resistances of various connections used in the field coil supply lines. The results are listed in table 2.1.

Wiring element	Resistance at 300 K	Resistance at 4 K
Al wire bond	0.6 Ω/cm	50 mΩ/cm
Cu PC board	1 mΩ/square	$\leq$ 0.1 mΩ/square
CuNi clad NbTi wires with solder joint		$\leq$ 0.2 mΩ
SIP connection	1 Ω	1 mΩ
Cinch connector	4 mΩ	1 mΩ

Table 2.1: Typical resistances of various elements in the field coil lines, measured with 4 probe measurements and a lockin amplifier at currents of 10 - 50 mA. The 4 K values were measured with the sample submerged in liquid He. Variations by about a factor 2 between different nominally identical samples were not uncommon, and there may be outliers with much larger resistances, for example for bad solder joints.

In the first cooldown without a thermal weak link (see 2.2.3), the field coil lines coming from the SQUID mount were connected to the filter wires using only solder joints rather than SIP connectors. However, the filters were still connected to the fridge loom via a cinch connector. With this configuration, I extracted a total resistance of 6 mΩ in the field coil lines from the amount of power dissipated by the supply current when the wire bonds were superconducting. In order to improve the base temperature at large field coil currents, I thus also replaced the cinch connector with solder joints between Cu and CuNi clad superconducting wires, which led to an

estimated residual resistance of 3 mΩ of unknown origin.

2.2.2 Thermal contact

Even at heat loads that allow the mixing chamber to reach an acceptable base temperature, it is not trivial to avoid large thermal gradients between where the heat is dissipated and the mixing chamber. For estimating thermal impedances, the Wiedemann-Franz law relating the thermal conductivity κ to the temperature T and electrical conductivity σ is quite useful.

$$\kappa(T) = L_{WF} T \sigma, \tag{2.4}$$

with $L_{WF} = 2.44 \cdot 10^{-8} W\Omega/K^2$. For copper, this relation holds fairly well [111]. Integrating it along a thermal pathway of total resistance R between two reservoirs at temperatures T_1 and T_2 leads to the conclusion that the heat power P conducted along the path is

$$P = \frac{L_{WF}}{2R}({T_1}^2 - {T_2}^2). \tag{2.5}$$

In the first cooldown without a thermal weak link (cf. 2.2.3), I recorded the mixing chamber temperature (T_1) at which a certain strongly T dependent feature (at an unknown sample temperature T_2) in the behavior of superconducting rings occurred as a function of power P dissipated by the field coil current. The results confirmed the functional form of Eq. 2.5 and led to a value of $R = 50\ \mu\Omega$ for the resistance of the relevant thermal pathway. At a field coil current of 40 mA, the resulting lowest attainable sample temperature was as high as 140 mK. In that cooldown, the copper parts of the scanner had been polished the last time several month before, and the copper mounting plate at the mixing chamber had not been polished recently at all. The scanner assembly was mounted on the latter with four 2–56 brass screws which could not be tightened very well.

Subsequent measurements of the contact resistance across a 12×8 mm^2 contact held by a single, well tightened 6–32 brass screws gave about 4 $\mu\Omega$ at 300 K and as low as 0.15 $\mu\Omega$ at 78 K, provided the contact areas were freshly polished. Those lockin

measurements were carried out in a liquid nitrogen bucket using a 1 A rms current supplied by a power amplifier. It appears that the results at 78 K were close to being limited by the bulk resistivity of the mating parts, indicating that the improvement by gold coating would not be dramatic. However, a gold coating should eliminate the necessity to polish the mating surfaces before each assembly. Clamping unpolished pieces of gold between two copper parts led to significantly higher resistances, likely due to the reduced contact area. Since brass and copper contract by about 0.38 and 0.32 % [111] between 300 K and 4 K, a joint made with a brass screw should be self tightening upon cooling.

To improve the thermal contact between the mixing chamber, the scanner assembly, the filters and the sample mount, I always polished the mating surfaces that were exposed to air before assembly, and added stronger and more screws where possible. In the cooldown during which I obtained the results from section 5.3, the sample thermometer read about 26 mK with a mixing chamber temperature of 22 mK at 35 mA current amplitude in the field coils. This implies a thermal resistance corresponding to about 1 $\mu\Omega$. It appears that using fine sand paper rather than polishing paper on the mixing chamber mounting plate led to a significant improvement compared to a previous cooldown, where I estimated 8 $\mu\Omega$.

Note that the copper clamps holding the copper tape worm filters in place and heat sinking them were not polished, and their screws could not be tightened very much. Thus, there is likely to be a large thermal resistance between the filters, which also serve as heat sinks for the wires, and the mixing chamber, so that the temperature of the filter used for the SQUID wires was likely a few hundred milli-Kelvin. Other filters should not be affected very much, since each filter is heat sunk individually.

2.2.3 Stable refrigerator operation up to 2 K

Due to the various phase transitions of the ^{3}He and ^{4}He mixture, dilution refrigerators tend to operate unstably above bout 0.7 K, the temperature at which a phase boundary forms. While reasonably stable operation is possible by throttling the circulation and opening the dump away from the phase transitions (another one occurs

around 1.2 K, above which the vapor pressure of ^{4}He increases), the sub-mK stability required for the experiments on Al rings in chapters 3, 4 and Ref. [78]) up to their T_c of 1.25 to -2 K would have been near impossible to achieve. We overcame this problem by thermally isolating the scanner assembly from the mixing chamber using a G10 adapter plate, and providing a limited amount of cooling power through a braided copper wire connected to the mixing chamber. Temperature was controlled through an additional heater and a Cernox thermometer mounted on the scanner assembly. With this setup, the temperature reading was generally stable to within 0.1 - 0.2 mK. The accessible temperature range was about 0.2 - 2 K.

Chapter 3

Superconducting rings with two order parameters

3.1 Magnetic response of mesoscopic superconducting rings with two order parameters

Hendrik Bluhm, Nicholas C. Koshnick, Martin E. Huber, Kathryn A. Moler,
Phys. Rev. Lett., **97**, 237002 (2006).

Abstract

The magnetic response and fluxoid transitions of superconducting aluminum rings of various sizes, deposited under conditions likely to generate a layered structure, show good agreement with a two-order-parameter Ginzburg-Landau model. For intermediate couplings, we find metastable states that have different phase winding numbers around the ring in each of the two order parameters. Those states, previously theoretically predicted, are analogous to fractional vortices in singly connected samples with two-order-parameter superconductivity. Larger coupling locks the relative phase so that the two order parameters are only manifest in the temperature dependence of the response. With increasing proximitization, this signature gradually disappears.

Since the discovery of two-gap superconductivity in MgB_2 [25], the coexistence of two not-too-strongly coupled superconducting order parameters (OPs) has motivated significant theoretical work. A striking prediction is the existence of vortices carrying unquantized flux [9, 10]. For non-negligible Josephson coupling, those exhibit a soliton-shaped phase difference between the two OPs [131, 9]. Theoretically, such solitons may also form when current flow along a wire causes the relative phase to unlock, leading to a higher current than in the phase locked state [60]. Most of this theoretical work is based on a two-OP Ginzburg-Landau (GL) theory [59]. In the realm of superconductivity, this model applies for both Josephson coupled bilayer systems, which are described microscopically by a tunneling BCS Hamiltonian, and intrinsic two-gap systems [105]. A particularly interesting example of the latter is Sr_2RuO_4. Its $p_x + ip_y$ OP would imply zero energy core excitations with non-abelian braiding statistics, which have been envisioned as a basis for topologically protected quantum computation [129, 39]. A similar two-OP model has also been used to describe a liquid metallic state of hydrogen [11], where the electrons and protons would form two independent superfluids.

Compared to the large number of theory papers, there is little experimental work on the mesoscopic structure of such two-OP systems. In this paper, we report the observation of soliton states and other phenomena arising from the interplay between two OPs in quasi-1D, superconducting rings consisting of two parallel, Josephson-coupled aluminum layers. Positioning a scanning SQUID microscope [17] over each ring individually enabled measurements of the current, I, circulating the ring as a function of applied flux, Φ_a, and temperature, T. The ensemble of magnetic responses includes distinct features that cannot be explained by one-OP GL, but can be described by numerical solutions of two-OP GL. The inferred coupling between the two OPs depends on the ring's annulus width, w, allowing us to study the crossover between intermediate and strong coupling regimes. For intermediate coupling, we find metastable states with different phase winding numbers for each OP. Those are the 1D analogue of unquantized vortices [9], and imply a soliton-shaped phase difference [131]. In this regime, multiple transition pathways between states give a rich structure

of hysteretic Φ_a-I curves. At stronger coupling, the system approaches the Cooper limit of complete proximitization [56]: the Φ_a-I curves at any temperature can be described by one-OP GL, but the existence of two OPs is manifest in the temperature dependence of the fitted penetration depth, λ, and the GL-coherence length, ξ_{GL}.

During a single, two-month-long cooldown, we characterized the magnetic response of 40 different rings with eight annulus widths 45 nm $\leq w \leq$ 370 nm and radii R of 0.5, 0.8, 1.2 and 2 μm. The rings were fabricated on oxidized silicon, using liftoff lithography with PMMA resist. The 40 nm thick Al film was deposited by e-beam evaporation at a rate of about 1 Å/s and a pressure of approximately 10^{-6} mBar. During the deposition, the rate temporarily dropped to a negligible level for about 10 min and subsequently recovered, which most likely caused the formation of two superconducting layers separated by an AlO_x tunneling barrier. A disk with a radius of 2 μm had a T_c of 1.6 K, representative of the bulk film. Using $\xi_0 = 1.6$ μm for pure bulk Al [95] and $\xi_{GL}(0) \approx 70$ nm for our rings, as derived below, we infer a mean free path of $l_e = 1.4\xi_{GL}(0)^2/\xi_0 = 4$ nm. The measured critical temperatures T_c of the rings ranged from 1.5 to 1.9 K, depending only on w. Both the short l_e and the large T_c compared to clean bulk Al indicate small grains and a (likely related) strong effect of oxygen impurities [108, 38].

Our SQUID sensor has two counterwound pickup loops and field coils that are used to apply a local magnetic field [62]. We position one pickup loop over a ring, record time traces of the SQUID response while sinusoidally varying Φ_a at a few Hz, and average hundreds to thousands of field sweeps. A background, measured by retracting the SQUID from the sample, is subtracted. The remaining signal is the flux generated by I, plus a residual, elliptic sensor background which is negligible at lower T and unambiguously distinguishable from the ring response at higher T, where fluxoid transitions occur. Details on the technique will be given elsewhere [78].

Rings with $w \leq 120$ nm show no two-OP effects. At low T [Fig. 3.1(a)], there are no fluxoid transitions at the experimental time scale and field sweep amplitude. At higher T [Fig. 3.1(b), (c)], we observe hysteretic transitions, which become non-hysteretic near T_c [Fig. 3.1(d)].

We obtain the theoretical Φ_a-I curve of an individual fluxoid state, n, directly

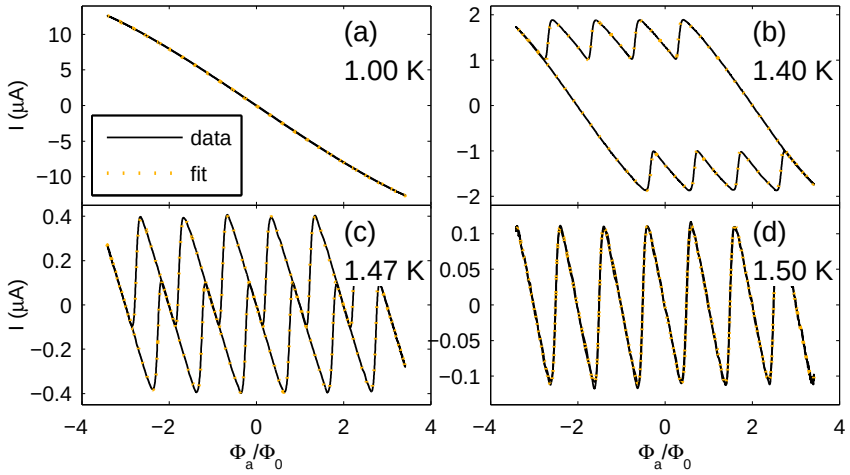

Figure 3.1: Φ_a-I curves for a ring with $w = 120$ nm and $R = 1.2$ μm, fitted to a one-order-parameter Ginzburg-Landau model. The selected curves represent the regimes discussed in the text: (a) no transitions, (b),(c) hysteretic and (d) thermal equilibrium.

from 1D, 1-OP GL [145]:

$$I_n(\varphi) = -\frac{wd\Phi_0}{2\pi R\mu_0\lambda^2}(\varphi - n)\left(1 - \frac{\xi_{GL}^2}{R^2}(\varphi - n)^2\right) \tag{3.1}$$

where $\varphi = \Phi_a/\Phi_0$, $\Phi_0 = h/2e$, and d is the total film thickness. n is the phase winding number of the GL-OP $\psi(x) = |\psi|e^{inx/R}$, where x is the position along the ring's circumference. $\varphi - n \ll R/\xi_{GL}$ gives the linear response of the London limit, while the cubic term arises from pair breaking. Because $wd \ll \lambda^2$, the self inductance can be neglected. Although the width of some rings is several ξ_{GL} at low T, the 1D approximation is justified here because $w \ll R$ and $H_a \ll H_{c2}$ [145].

Close to T_c [Fig. 3.1(d)], transitions are fast enough to model the experimental Φ_a-I curves as a thermal average over all possible states,

$$\langle I(\varphi)\rangle = \frac{\sum_n I_n(\varphi)e^{-E_n(\varphi)/k_BT}}{\sum_n e^{-E_n(\varphi)/k_BT}} \tag{3.2}$$

with $E_n(\varphi) = -\Phi_0 \int_n^\varphi d\varphi' I_n(\varphi')$. We set $\xi_{GL} = 0$ when substituting Eq. (3.1) into Eq. (3.2) because the thermal rounding dominates the cubic term [1]. The free parameters in the fit are λ^{-2}, three background parameters, a small offset in φ, the pickup loop–ring inductance M_{coup}, and the field coil–ring inductance. The fitted inductances are consistent with less accurate geometrical estimates, and are used at lower T.

The hysteretic curves [Fig. 3.1(b), (c)] are rounded from averaging over a distribution of thermally activated transitions [82] near a typical $\varphi = \phi_t + n$. We model them by combining Eq. (3.1) with occupation probabilities $p_n(\varphi - n)$ obtained from integrating the rate equation $dp_n/dt = -p_n/\tau_0 \exp(-E_{act}(\varphi - n)/k_B T)$. For fitting, τ_0 and the activation energy E_{act} are absorbed into ϕ_t. The free parameters are ϕ_t, $dE_{act}/d\varphi(\phi_t)$, ξ_{GL}, λ^{-2}, and three background parameters. φ_t increases very weakly with increasing field sweep frequency, as expected for thermally activated behavior.

For $T \ll T_c$, where no transitions are seen, Eq. (3.1) fits the data with three parameters corresponding to ξ_{GL}, λ^{-2}, and a constant background.

The above models result in excellent fits for measured Φ_a-I curves except at $w = 190$ nm as discussed below. The fitted values for λ^{-2} and ξ_{GL} are shown in Fig. 3.2 for rings typical of each w. All 14 measured rings with $w \leq 120$ nm show T dependences similar to the 1-OP phenomenological expressions $\lambda(T)^{-2} = \lambda(0)^{-2}(1 - t^4)$ and $\xi_{GL}(T) = \xi_{GL}(0)\sqrt{(1+t^2)/(1-t^2)}$, with $t = T/T_c$. For $w \geq 190$ nm, $\lambda^{-2}(T)$ has a high-temperature tail to an enhanced T_c and a peak in ξ_{GL} near but below T_c. Both effects are most pronounced at $w = 190$ nm. The Φ_a-I curves remain hysteretic well into the tails, showing that the enhanced T_c is not a fluctuation effect.

The most striking features of the Φ_a-I curves for a $w = 190$ nm ring [Fig. 3.3(a)-(f)], typical for all six measured rings with $w = 190$ nm and $R \geq 0.8$ μm [2], are transition points in the lower T hysteretic region that are not a function of $\varphi - n$ only, and reentrant hysteresis. The latter is qualitatively related to the local maximum in $\xi_{GL}(T)$ [Fig. 3.2(b)], since in 1-OP GL, a state becomes unstable at $|\varphi - n| \geq \sqrt{R^2/\xi_{GL}^2 + 1/2}/\sqrt{3}$ [138]. However, rather than an increase of the transitions point ϕ_t upon raising T, as expected for a decreasing $\xi_{GL}(T)$, the amplitude

[1] Fluctuation effects within a few mK of T_c [140], where it would be inadequate to set $\xi_{GL} = 0$, will be discussed in Ref. [78].

[2] For rings with $R = 0.5$ μm, Φ_a was too small to observe those features.

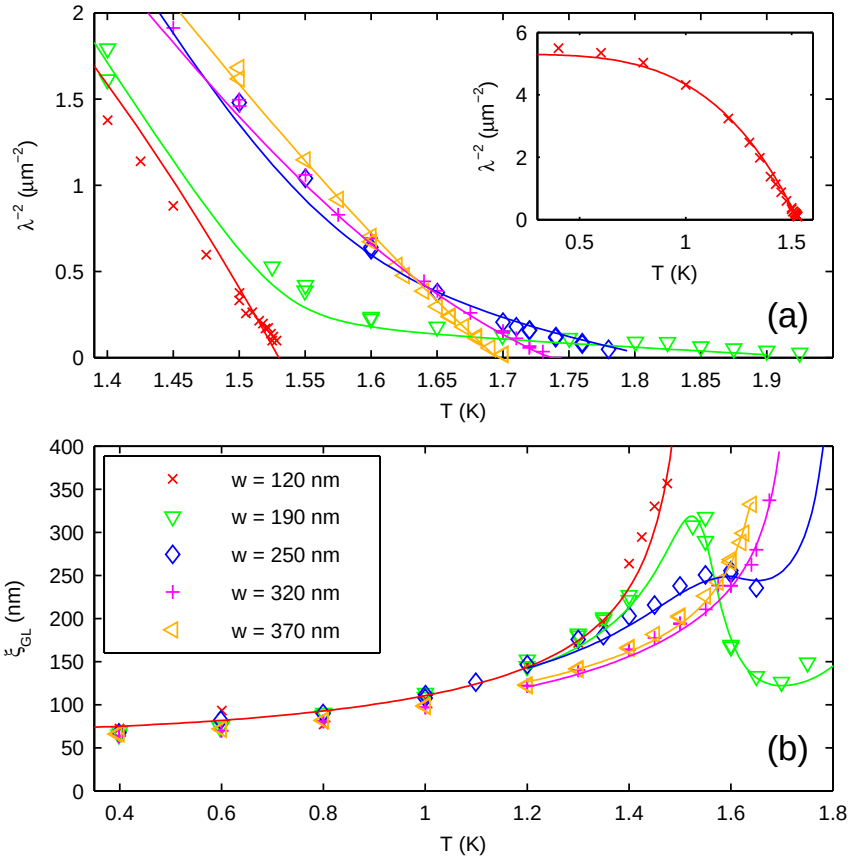

Figure 3.2: (a) λ^{-2} and (b) ξ_{GL} for rings representative of each annulus width w. The discrete symbols are obtained from fits to Φ_a-I curves. Continuous curves represent fits to phenomenological expressions ($w = 120$ nm) or the two-order-parameter GL model ($w \geq 190$ nm), which was only fitted above 1.2 K where GL applies.

of those transitions is reduced until a non-hysteretic curve with a flattening too pronounced to be described by Eq. (3.1) [Fig. 3.3(d)] appears. With a further increase of T [Fig. 3.3(e), (f)], this flattening also disappears and the Φ_a-I curves evolve similarly to Fig. 3.1. This strongly suggests the existence of two OPs, one causing the small ripples in Fig. 3.3(c), and one with a larger T_c adding the large background response and causing the tail in $\lambda^{-2}(T)$. The additional phase winding number from a second, coupled OP also explains the irregular transitions in [Fig. 3.3(a)-(c)]. Although also breaking strict flux periodicity, finite line width corrections to 1D, 1-OP GL [145] would be much smaller and more regular. A vortex pinned in the annulus could in principle lead to similar Φ_a-I curves, however w is too small compared to ξ_{GL} to accommodate its core,and it cannot explain the T dependence of λ^{-2} and ξ_{GL}.

A two-OP GL-model consisting of two standard 1D GL free energy functionals and a coupling term indeed reproduces the peculiar features of Fig. 3.2 and 3.3:

$$\begin{aligned} F[\psi_1,\psi_2,\varphi] &= F_1[\psi_1,\varphi]+F_2[\psi_2,\varphi] \\ &+ \frac{\gamma w}{2}\int_0^L dx|\psi_1-\psi_2|^2 \quad \text{with} \qquad (3.3) \\ F_i[\psi_i,\varphi] &= wd_i\int_0^L dx\left\{\frac{\hbar^2}{2m}\left|\left(-i\nabla+\frac{\varphi}{R}\right)\psi_i\right|^2\right. \\ &+ \left.\frac{\alpha_i}{2}|\psi_i|^2+\frac{\beta_i}{4}|\psi_i|^4\right\} \qquad (3.4) \end{aligned}$$

We define ψ_1 to have the lower T_c. If both components have the same n, one can make the usual ansatz $\psi_i(x)=|\psi_i|e^{inx/R}$. Minimizing (3.3) with respect to $|\psi_1|$ and $|\psi_2|$ results in excellent fits to Φ_a-I curves as in Fig. 3.3(d). At small φ, both OPs contribute significantly, but as φ is increased, pair breaking strongly reduces $|\psi_1|$, whose ξ_{GL} diverges near $T_{c,1}$. In the absence of the more stable ψ_2, ψ_1 would undergo a fluxoid transition much before $|\psi_1|$ could be suppressed that much.

We extracted effective values of $\lambda^{-2}(T)$ and $\xi_{GL}(T)$ from such modeled Φ_a-I curves (and also from fits to datasets similar to Fig. 3.3(d)) using a small φ expansion analogous to Eq. (3.1). Assuming a linear T dependence of α_1 and α_2, this procedure can reproduce the observed form of $\lambda^{-2}(T)$ and $\xi_{GL}(T)$ as demonstrated by the fits

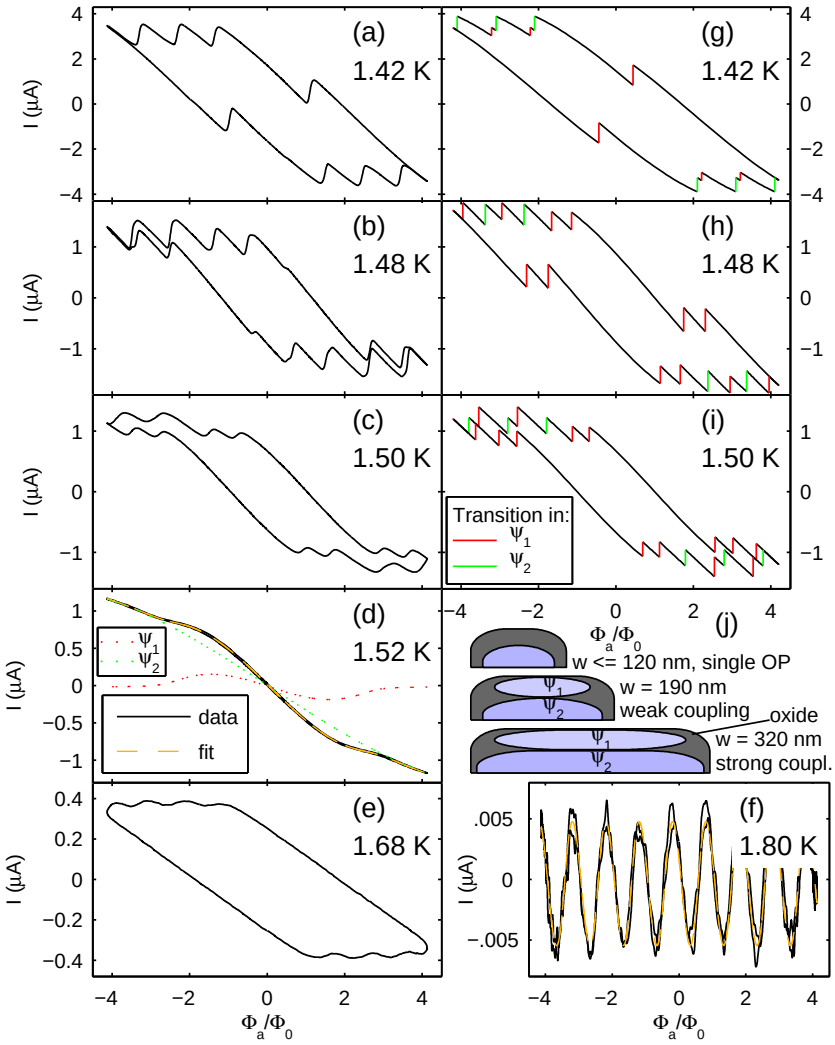

Figure 3.3: (a)-(f): Φ_a-I curves for a ring with $w = 190$ nm and $R = 2$ μm, where the coupling between the two order parameters is weak. In (a) - (c), states with two different fluxoid numbers lead to the observed transition pattern. In (d), no transition occurs because one component is stabilized by the other. Dotted lines show the contributions of ψ_1 and ψ_2 derived from the model. (e) and (f), taken above the lower T_c, reflect the response of a single order parameter. (g)-(i): Results from the two-OP model corresponding to (a)-(c). (j): Schematic of film structure (cross section).

in Fig. 3.2. The knee in $\lambda^{-2}(T)$ corresponds to the lower $T_{c,1}$, above which the amplitude of ψ_1 becomes very small. From $w = 190$ nm to $w = 370$ nm, the coupling strength γ increases by a factor 30-50, by far the largest line width dependence of all fit parameters [3]. The resulting stronger proximitization smears out the two-OP features. It appears that ψ_1 not only has a lower T_c, but also a smaller l_e than ψ_2. Fit parameters obtained from Φ_a-I curves and the curves in Fig. 3.2 are consistent within about a factor 2. This discrepancy may be due to fluctuations of ψ_1 at large φ, or a nontrivial phase difference [60], which are not considered in our model for Φ_a-I curves.

To model the hysteretic Φ_a-I curves [Fig. 3.3(a)-(c)], we calculate the activation energies $E_{act}(\varphi - n)$ for transitions in either ψ_1 or ψ_2 by numerically computing saddle point solutions of the GL - equations obtained from variation of (3.3), assuming that the relevant saddle points evolve continuously from those of the uncoupled system upon increasing γ. We then derive the complete Φ_a-I curve assuming that a transition in ψ_i occurs whenever $E_{act}(\varphi - n) < \kappa_i k_B T$, where the $\kappa_{1,2}$ are treated as phenomenological parameters of order unity. Of several simulation runs with various parameters similar to those obtained from the fits, the one shown in Fig. 3.3(g)-(i) gave the best similarity with the data [Fig. 3.3(a)-(c)]. While the uncertainty of the fit parameters [see Sec. 3.2] and simplicity of the model forbid a more quantitative comparison, the simulations show that metastable states with $n_1 \neq n_2$ are key to understanding the observed Φ_a-I curves. Due to the coupling between the OPs, the variation of the relative phase is soliton-like [131], similar to a Josephson vortex, however with the phase gradient along the junction being mostly due to the kinetic rather than the magnetic inductance. This soliton corresponds to the domain walls originating from unquantized vortices in bulk samples [9]. Intuitively, it is formed upon increasing φ when the larger ξ_{GL} of ψ_1 causes ψ_1 to become unstable at a smaller φ than ψ_2, and the coupling is weak enough for ψ_2 to stay in the same state. However, the soliton energy makes it less stable than states with $n_1 = n_2$. This leads to the observed step-like transition sequence.

[3] See section 3.2 for a discussion of the fit procedures and parameters.

Apart from the general agreement with the simulations and the irregular transitions, the most direct experimental evidence for states with $n_1 \neq n_2$ are branches of Φ_a-I curves that are shifted relative to each other by less than one Φ_0 horizontally, such as around $\Phi_a/\Phi_0 \approx \pm 3$ in Fig. 3.3(b). Individual, unaveraged field sweeps show that this is not an effect of averaging over different transition pathways, contrary to the features at $\Phi_a/\Phi_0 \approx \pm 0.3$.

The emergence of two OPs can be explained by the temporary drop of the deposition rate during the metalization. At the lower rate, more oxygen was co-deposited to form a tunneling barrier [see Fig. 3.3(j)]. Different oxygen concentrations and/or grain sizes led to different values of T_c and ξ_{GL} in the two superconducting layers. It is known that PMMA outgases significantly and that thinner lines are affected more [45]. This likely caused the line width dependence of the coupling and the complete oxidization of one of the superconducting layers for $w \leq 120$ nm, where we found no evidence for two OPs. The critical Josephson current densities estimated from the inferred values of γ support this picture [see Sec. 3.2].

This fabrication result was unintentional but fortuitous. While the parameters should be tunable a priori with controlled exposure to oxygen gas, it would be difficult to obtain reproducible results from outgasing resist. Nevertheless, the data and analysis draw a clear picture of a two-OP superconductor with GL parameters that depend consistently on w. This dependence and the occurrence of two different T_c's allowed the study of a wide range of parameters. The insight thus gained may be used to design similar experiments on intrinsic two-component superconductors. The creation and detection of $h/4e$ vortices in Sr_2RuO_4 would be of particular interest [129, 39]. Since their energy is logarithmically or linearly divergent in the sample size [9, 10], they might only be accessible as metastable states in mesoscopic samples, similar to the soliton states discussed here.

In conclusion, we have explored effects emerging from two coupled order parameters in mesoscopic superconducting rings. The most interesting ones are an anomalous temperature dependence of the average superfluid density λ^{-2} and effective coherence length ξ_{GL}, and a qualitative modification of the behavior of phase slips related to previously predicted metastable states with two different phase winding numbers [60, 9]

and a soliton-shaped phase difference [131].

This work was supported by NSF Grants No. DMR-0507931, DMR-0216470, ECS-0210877 and PHY-0425897 and by the Packard Foundation. Work was performed in part at the Stanford Nanofabrication Facility, which is supported by NSF Grant No. ECS-9731293, its lab members, and industrial affiliates. We would like to thank Per Delsing, Egor Babaev and Mac Beasley for useful discussions.

3.2 Two-order-parameter GL fits

Hendrik Bluhm, Nicholas C. Koshnick, Martin E. Huber, Kathryn A. Moler,
EPAPS Document No. E-PRLTAO-97-084648
(available at `http://www.aip.org/pubservs/epaps.html`).

Abstract

This addendum to Ref. [22] describes the procedures used to fit the two-order-parameter GL model to the data and discusses the resulting parameters.

For a ring consisting of two Josephson-coupled layers, the most natural form for a GL-functional in the 1D approximation is

$$\begin{aligned} F[\psi_1,\psi_2,\varphi] &= F_1[\psi_1,\varphi]+F_2[\psi_2,\varphi] \\ &+ \frac{w\gamma}{2}\int_0^L dx|\psi_1-\psi_2|^2 \quad \text{with} \qquad (3.5) \\ F_i[\psi_i,\varphi] &= wd_i\int_0^L dx\left\{\frac{\hbar^2}{2m}\left|\left(-i\nabla+\frac{\varphi}{R}\right)\psi_i\right|^2\right. \\ &+ \left.\frac{\alpha_i}{2}|\psi_i|^2+\frac{\beta_i}{4}|\psi_i|^4\right\} \qquad (3.6) \end{aligned}$$

(cf. Eqs. (3.3), (3.4)). Phenomenologically, the coupling term can be motivated in the weak coupling limit by the requirement that it should yield a $\cos(\phi_1 - \phi_2)$ dependence on the phase difference and not change the free energy if two identical superconductors with the same phase are coupled to each other. For small γ and near T_c, it also reproduces the temperature dependence of the critical current density $J_c = \gamma 2\pi/\Phi_0|\psi_1||\psi_2|$ near T_c, which was calculated from microscopic theory in Refs. [4, 3]. For identical $T_{c,1} = T_{c,2}$, one obtains $J_c \propto |\psi|^2 \propto 1 - T/T_c$. For $T \lessapprox T_{c,1} < T_{c,2}$ on the other hand, the temperature dependence near $T_{c,1}$ is dominated by $|\psi_1| \propto \sqrt{1 - T/T_c}$.

By absorbing the terms $\gamma|\psi_i|^2$ in the functional (3.5) into the quadratic terms in F_i and renormalizing the order parameter, it can be brought into the form

$$\begin{aligned} \tilde{F}[\tilde{\psi}_1, \tilde{\psi}_2, \varphi] &= F_1[\tilde{\psi}_1, \varphi] + F_2[\tilde{\psi}_2, \varphi] \\ &- \frac{wd\tilde{\gamma}}{2} \int_0^L dx (\tilde{\psi}_1^* \tilde{\psi}_2 + \tilde{\psi}_1 \tilde{\psi}_2^*) \quad \text{with} \qquad (3.7) \\ \tilde{F}_i[\tilde{\psi}_i, \varphi] &= wd \int_0^L dx \left\{ \frac{\hbar^2}{2m} \left| \left(-i\nabla + \frac{\varphi}{R} \right) \tilde{\psi}_i \right|^2 \right. \\ &+ \left. \frac{\tilde{\alpha}_i}{2} |\tilde{\psi}_i|^2 + \frac{\tilde{\beta}_i}{4} |\tilde{\psi}_i|^4 \right\} \qquad (3.8) \end{aligned}$$

which has been shown to emerge from microscopic theory for two-band superconductors [59]. We are not aware of a direct derivation of the functional (3.5) for the tunneling case from microscopic theory. However, it has been shown [105] that a tunneling BCS Hamiltonian leads to the same Greens functions as a two band BCS model [130] to second order in the tunneling matrix elements. Thus, it appears that the equivalence between (3.5) and (3.7) holds much beyond GL theory. Although one may expect higher order terms to become significant at stronger coupling, the above functionals should still give a qualitatively correct approximation.

In principle, either form could be used as a starting point to obtain fit models, as the parameters of one are convertible into those of the other with the following

transformations:

$$\tilde{\psi}_i = \nu_i^{1/2}\psi_i \tag{3.9}$$

$$\tilde{\alpha}_i(T) = \alpha_i(T) + d_i^{-1}\gamma \tag{3.10}$$

$$\tilde{\beta}_i = \nu_i^{-1}\beta_i \tag{3.11}$$

$$\tilde{\gamma} = (d_1 d_2)^{-1/2}\gamma \tag{3.12}$$

where $\nu_i = d_i/(d_1 + d_2)$ is the volume fraction occupied by ψ_i in a layered structure.

Not counting the known geometric dimensions and $\nu_{1,2}$, which are not independent from other parameters, there are five GL parameters at any given T and seven if modeling a linear temperature dependence of the $\alpha_{1,2}$, as customary for GL theory. It turns out that in practice, fits of the model to our data are effectively underdefined, so that a wide range of parameter combinations reproduce individual $\Phi_a - I$ curves or $\xi(T)$ and $\lambda^{-2}(T)$ fairly well. To overcome this problem, we have fixed some parameters in each individual fit and made an effort to choose the fixed values such that a physically reasonable dependence of all parameters on w is obtained. Although one might expect more accurate results from fitting all data curves at once, this computationally less complex procedure is sufficient to obtain a consistent overall picture.

Naturally, it is most appropriate to fix parameters that are expected to be independent of T and/or w and physically meaningful. In the functional (3.5),(3.6), $T_{c,i}$ as defined by $\alpha_i(T_{c,i}) = 0$, is the actual bare T_c of ψ_i. In the second form [Eqs. (3.7) and (3.8)] on the other hand, the temperatures at which $\tilde{\alpha}_i(T) = 0$ will be smaller than the bare $T_{c,i}$ because of the γ/ν_i term in Eq. (3.10). Furthermore, the values of $\tilde{\beta}_{1,2}$ and $\tilde{\gamma}$ do not correspond to their physical values for a Josephson coupled bilayer system due to the absorption of ν_i into the normalization of $\tilde{\psi}_i$. Thus, the form (3.5) and (3.6) is more adequate for our purposes.

We have parametrized the temperature dependence of $\alpha_{1,2}$ by $\alpha_i(T) = (T/T_{c,i} - 1)\overline{\alpha}_i$, and assumed all other coefficients to be independent of T. The complete set of fit model parameters consists of $\overline{\alpha}_{1,2}$, $\nu_1 = 1 - \nu_2$, $\epsilon_{1,2} = \overline{\alpha}_{1,2}^2/\beta_{1,2}$, and γ/d. ν_1 had to be included because the individual layer thicknesses $d_{1,2}$ appearing in the prefactors

of Eq. (3.6) are unknown in our samples. The condensation energy densities extrapolated to $T = 0$, $\epsilon_{1,2}$, were used instead of, say, $\beta_{1,2}$, as they should be independent of the mean free path and thus are reasonable to keep fixed.

For the purpose of fitting, we set $\hbar^2/m$ to 1 and normalize $\psi_{1,2}$ and consequently $\beta_{1,2}$ such that one would obtain $|\psi|^2 = \alpha/\beta = \lambda^{-2}$ in the absence of any applied flux or phase winding for a single OP. For this choice of units, it is natural to measure the coupling in terms of γ/d so that the cross section wd only appears in the prefactor of the GL functional (3.5), which has to be multiplied by $\Phi_0^2/4\pi^2\mu_0$ to convert to physical energy. For equal phase winding numbers $n_1 = n_2 = n$ in both OPs, one can make the ansatz $\psi_i(x) = |\psi_i|e^{inx}$, where x is the spatial coordinate along the ring circumference. Variation of Eq. (3.5) w.r.t. $|\psi_{1,2}|$ leads to

$$(\alpha_i + (\varphi - n)^2/R^2)|\psi_i| + \beta|\psi_i|^3 + \gamma(|\psi_i| - |\psi_{2-i}|) = 0$$

for $i = 1, 2$ which can be solved numerically for $|\psi_1|$ and $|\psi_2|$. With the above normalization of $|\psi_{1,2}|$, the supercurrent circulating the ring is

$$I = -\frac{wd\Phi_0}{\mu_0 2\pi R}(\varphi - n)(|\psi_1|^2 + |\psi_2|^2) \tag{3.13}$$

In order to extract an effective λ^{-2} and ξ_{GL} to be used as fit model from a $\Phi_a - I$ curve computed numerically using Eq. (3.13), we have approximated it by a cubic polynomial at small φ according to Eq. (3.1): λ^{-2} is proportional to the linear coefficient , and ξ_{GL}^2/R^2 the ratio of the cubic and linear coefficients. The same procedure was used to obtain the experimental values of λ^{-2} and ξ_{GL}, shown in Fig. 3.2, from fits to measured curves like the one in shown Fig. 3.3(d), which show two component effects but no fluxoid transitions. While the interpretation of those values as a physical coherence length and superfluid density is somewhat questionable at least for weak coupling, this provides an operational definition that is consistent with the 1D GL result in Eq. (3.1).

For the simultaneous fits to the temperature dependence of λ^{-2} and ξ_{GL} shown in Fig. 3.2, we fixed $T_{c,1}$, $T_{c,2}$ and $\epsilon_{1,2}$ and kept $\overline{\alpha}_{1,2}$, $\nu_1 = 1 - \nu_2$ and γ/d as free

parameters. The fit results are shown in the first four columns of table 3.1.

	1	2	3	4	5	6	7
Data type	T-dep.	T-dep.	T-dep.	T-dep.	T-dep.	$\Phi_a - I$	simul.
w (nm)	370	320	250	190	190	190	190
R (μm)	1.2	2.0	0.8	2.0	2.0	2.0	2.0
$T_{c,1}$ (K)	1.53	1.53	1.52	1.52	1.53	1.56	1.53
$T_{c,2}$ (K)	1.98	1.98	1.98	1.98	1.98	1.80	1.90
$\overline{\alpha}_1$ (μm^{-2})	-205	-241	-189	-219	-136	-94	-123
$\overline{\alpha}_2$ (μm^{-2})	-414	-389	-366	-728	-736	-1325	-326
ϵ_1 (μm^{-4})	4545	4545	4545	4545	4545	4783	2278
ϵ_2 (μm^{-4})	4545	4545	4545	4545	4545	4475	2274
γ/d (μm^{-2})	64	22	7.6	2.2	0.96	1.2	0.24
ν_1	0.78	0.76	0.80	0.87	0.81	0.37	0.66
J_c (kA/cm^2)	196	63	26	5	3	3	1

Table 3.1: The first four columns show the parameters from the fits in Fig. 3.2. Column 5 and 6 contain parameters from the ring in Fig. 3.3, obtained from the T-dependence of λ^{-2} and ξ_{GL} and $\Phi_a - I$ curves as in Fig. 3.3(d), respectively. The parameters in the last column were used for the simulation of hysteretic $\Phi_a - I$ curves.

In the 1-OP case, λ^{-2} and ξ_{GL} give a complete description of the $\Phi_a - I$ for a given n and geometry. If two-OP effects are manifest in a $\Phi_a - I$ curve on the other hand, its more complex shape contains additional information, which can be used to check the consistency with the 2-OP GL-coefficients obtained from the temperature dependence. We have done this by fitting all the relevant $\varphi - I$ curves from the one ring presented in Fig. 3.3 with fixed values for $\beta_{1,2}$, obtained from the temperature dependence fits. This constraint was necessary as otherwise there would be a wide range of parameter combinations consistent with the data. From the results, we have extracted the parameters listed in column 6 of table 3.1 by fitting the temperature dependences of $\alpha_{1,2}$ with a linear model and converting all parameters to the definitions used to model the temperature dependence. The results differ by up to a factor of about 2 from the values obtained from $\xi_{GL}(T)$ and $\lambda^{-2}(T)$ of the same ring (column 5). It is possible that the disagreement could be reduced by a better choice of the fixed parameters. However, we speculate that it may partly be due to fluctuation effects

in ψ_1 at large φ, where $|\psi_1|$ is strongly suppressed, which go beyond the scope of our model.

Column 7 of table 3.1 shows the input parameters for the numerical modeling of hysteretic $\Phi_a - I$ curves with different phase winding numbers, shown in Fig. 3.3(g)-(i). The phenomenological parameters $\kappa_1 \approx 6$ and $\kappa_2 \approx 25$ were chosen for best similarity between the simulations and data. Our transition criterion $E_{act}(\varphi - n) < \kappa_i k_B T$ was motivated as a condition for the thermally activated transition rate $1/\tau_0 e^{-E_{act}(\varphi)/k_B T}$ to become comparable to the experimental time scale $t_{exp} \sim 0.1$ s [82, 93]. Identifying κ with $\log(t_{exp}/\tau_0)$, this corresponds to attempt rates of $1/\tau_0 \sim 5000$ s^{-1} and 10^{11} s^{-1} for ψ_1 and ψ_2, respectively. Given that those rates depend exponentially on the $\kappa_{1,2}$, the unphysical values (particularly for ψ_1) do not represent an excessively large inconsistency. Using column 5 as input parameters, the similarity of the simulation results with the data was less convincing.

The line width dependence of the parameters in table 3.1 shows a clear trend in γ, corresponding to the crossover from intermediate coupling to nearly complete proximitization. There is also evidence for an increase of $\overline{\alpha}_2 = \xi_{GL,2}^{-2}$ with decreasing w, indicating a shorter mean free path in the narrower rings. This is likely due to the same effect that eliminates ψ_2 altogether in rings with $w \leq 120$ nm. However, the opposite trend in $\overline{\alpha}_1$ suggests that the sampling of both layers by electronic wave functions at stronger coupling may also play a role in determining the $\overline{\alpha}_{1,2}$. All other parameters show no strong dependence on w.

Near T_c, the thermodynamic critical field H_c is given by the relations $8\pi^2 H_c(T)^2 \Phi_0^2 = \lambda^{-2}\xi_{GL}^{-2} = \alpha(T)^2/\beta$. Due to deviations from the linear temperature dependence of ξ_{GL}^{-2} and λ^{-2} implied by our GL model, the second equality breaks down at low T. Assuming a phenomenological temperature dependence $H_c(T) = H_c(0)(1 - (T/T_c)^2)$, and matching it to the GL result near T_c, one obtains $\epsilon = \overline{\alpha}^2/\beta = 32\pi^2 H_c(0)^2 \Phi_0^2$. $\epsilon = 4500\mu\text{m}^{-4}$, as used in most of the fits, thus corresponds to $H_c(0) = 80$ G. Given the extrapolation involved in this calculation, this is in reasonable agreement with the bulk value $H_c(0) = 100$ G. Taking into account that the enhanced T_c should also increase the condensation energy makes the agreement slightly worse.

To estimate the critical interlayer Josephson current density J_c at low T from

the coupling constant γ, we use the relation $J_c(T) = 2.67J_c(0)(1 - T/Tc)$ [4, 3], which is valid near T_c for symmetric junctions between identical superconductors. The dissimilarity between the two layers in our rings should only lead to correction factors of order unity. Including prefactors and approximating the amplitudes by their values in the uncoupled system, the contribution of the coupling term to Eq. (3.5) per unit area is

$$E_J(T) = \frac{\Phi_0^2}{8\pi^2\mu_0}\gamma|\psi_1||\psi_2| = \frac{\Phi_0^2}{8\pi^2\mu_0}\gamma\sqrt{\frac{\alpha_1(T)\alpha_2(T)}{\beta_1\beta_2}}$$

for $T \lessapprox Tc$, thus giving a critical current density

$$J_c(0) = \frac{\Phi_0}{2.67 \cdot 4\pi\mu_0}\gamma\sqrt{\frac{\overline{\alpha}_1(T)\overline{\alpha}_2(T)}{\beta_1\beta_2}}$$

The last row in table 3.1 shows the values obtained from the fit parameters.This can be compared to known junction fabrication processes: Extrapolating the Nb/Al/Al0_x/Nb trilayer process characterization in Ref. [119] to a 10 min, 10^{-6} mBar exposure, one obtains a critical current density on the order of 100 kA/cm^2, which compares well to the largest extracted values. Given that according to Ref. [119], a factor 100 reduction in critical current corresponds to a four orders of magnitude larger exposure, it seems unlikely that the oxidization process for smaller line widths can be thought of as analogous to the oxygen exposure of a thin film after deposition. It is more plausible that the co-deposition of aluminum and possible direct contact with the resist plays a role.

In conclusion, we have shown that different ways of analyzing and modeling our data in a two-OP GL framework give physically reasonable values for the GL coefficients that agree within about a factor 2. Thus, we find that the modeling supports the two-OP interpretation.

3.3 Detailed analysis of a 2-component Φ_a–I curve

It is conceivable that averaging over field sweeps in which the fluxoid number is not always the same at a given value of φ, even far from any transition, may result in Φ_a–I curves similar to those in Fig. 3.3. For example, branches of an averaged Φ_a–I curve which appear separated by a non-integer change in φ, or have a zero at a non-integer value of φ, can be explained this way. We definitely encountered this situation in some curves without other two-OP effects, where a transition occurs right around the maximum value of φ, so that it does not happen in every field sweep. A similar effect happens if the state selection process after a transition is non-deterministic, as observed in chapter 4.

Examination of single field sweeps helps ruling out this mechanism as a potential alternative explanation for some of the two-OP effects. Fig. 3.4 shows two types of individual traces and the resulting average from a ring that is nominally identical to the one shown in Fig. 3.3, taken at the same temperature as panel Fig. 3.3(b). The little step at $\varphi = \pm 0.3$ in Fig. 3.3(b) most likely originates in the same or a very similar statistical mix of two different transition sequences. Most other irregular features on the other hand appear to be true two-OP effects, as they are also present in each individual field sweep.

Nevertheless, due to sensor noise in Fig. 3.4 and the (unlikely) possibility of different behaviors in different rings, the data discussed so far does not quite give a rigorous proof of states with $n_1 \neq n_2$. However, a Φ_a–I curve from yet another ring, shown in Fig. 3.5, gives further convincing evidence that the two-OP interpretation is correct. As demonstrated by the dashed lines in Fig. 3.5, this curve can be modeled fairly accurately by a fit by eye in which the inter-component coupling is neglected and $n_2 = 0$ throughout, while $n_1 = -3, \ldots, 3$. The branches of the combined response extrapolate to zero at non-integer values of φ.

This dataset also allows a simple semiquantitative explanation of the transition sequence based on a phase-only model in the London limit. In the following, I will first discuss this model and its soliton solutions and then show how it can explain the fluxoid transitions in Fig. 3.5. The first part closely follows the treatment in Ref.

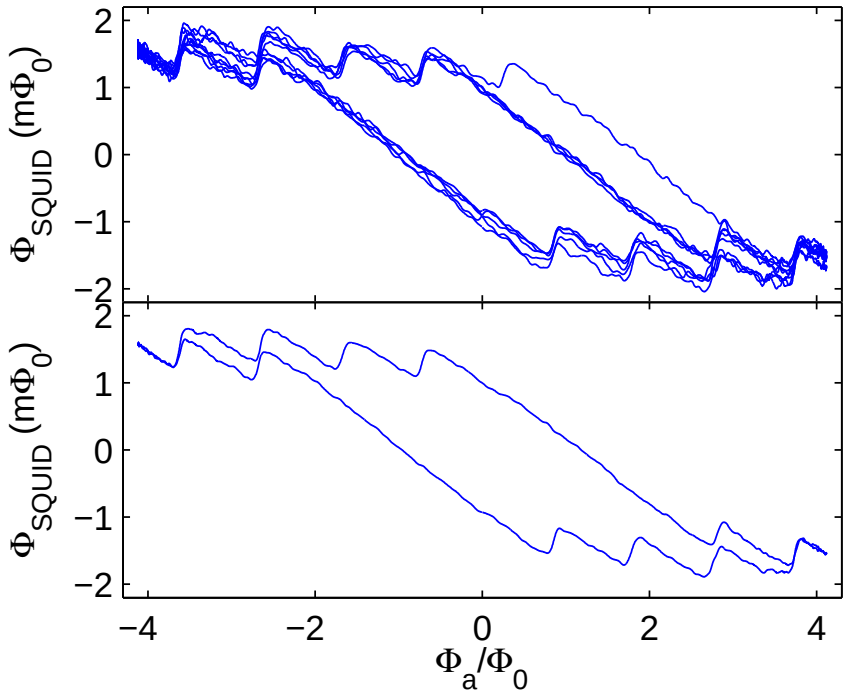

Figure 3.4: Five single field sweeps (top) and their average (bottom) for a ring nominally identical to the one in Fig. 3.3 at $T = 1.475$ K, as Fig. 3.3(b).

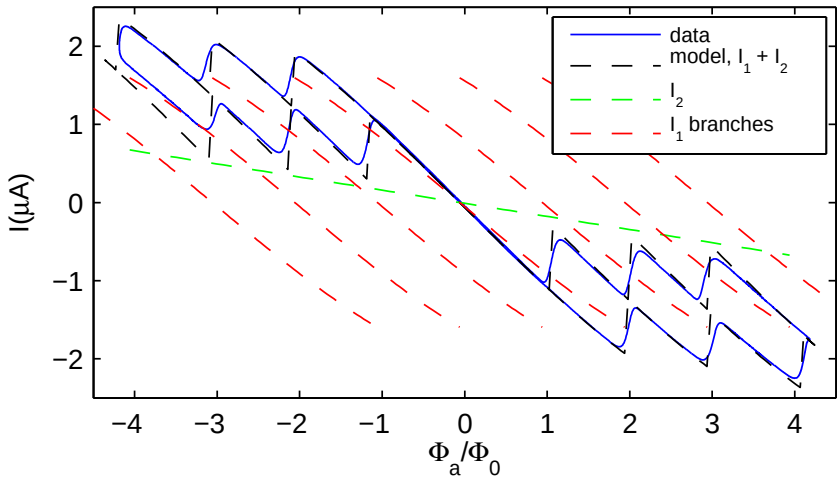

Figure 3.5: Φ_a–I curve from a ring with $w = 190$ nm and $R = 4$ μm at $T = 1.45$ K, in which $n_2 = 0$ throughout. This allows an unambiguous identification of the fluxoid numbers. The black dashed lines represent a fit by eye to a model of the form $I(\varphi) = -a_1(\varphi - n_1)(1 - \xi_1^2/R^2(\varphi - n_1)^2) - a_2\varphi$, which neglects the effect of the coupling on the order parameter amplitude and pair breaking in ψ_2. The contribution of each order parameter in this model is shown in red and green. The calibration and offset in φ were obtained from higher T data. The transition points and a y-offset of 0.13 μA were inserted by hand.

[131], however with a modification that eliminates an apparent error in the continuity condition around the ring.

Assuming constant superfluid densities $|\psi_{1,2}|^2$ in Eq. (3.7), one obtains a phase-only energy functional of the form

$$F[\phi_1, \phi_2, A] = \hbar^2 \left(\sum_{i=1}^{2} \frac{\rho_i}{2} \int_0^L dx \left(\nabla\phi_i + \frac{2\pi}{\Phi_0} A \right)^2 + \kappa \int_0^L dx \cos(\phi_2 - \phi_1) \right) \quad (3.14)$$

with $\rho_i = w d_i \left|\psi_i\right|^2 / m$ and $\kappa = \gamma w |\psi_1 \psi_2| / \hbar^2$. As a different gauge than so far will be used below, no explicit expression for the vector potential A has been used. Variation w.r.t. $\phi_{1,2}$ leads to a pair of continuity equations coupled through the Josephson term. They can be transformed into the Sine-Gordon equation for the phase difference $\theta = \phi_2 - \phi_1$, which decouples from the vector potential:

$$-\nabla^2\theta + \zeta^{-2} \sin(\theta) = 0 \quad (3.15)$$

with $\zeta^{-2} = \kappa(1/\rho_1 + 1/\rho_2)$. Single-valuedness and smoothness of the OPs $\psi_i(x) = |\psi_i| e^{i\phi_i(x)}$ impose the boundary conditions $\theta(L) = 2\pi(n_2 - n_1)\theta(0)$ and $\nabla\theta(L) = \nabla\theta(x)$. For $|n_2 - n_1| = 1$ and $\zeta \ll L$, the single soliton solution of Eq. (3.15) is

$$\theta(x) = 4 \arctan\left(e^{\pm \frac{x - x_0}{\zeta}} \right). \quad (3.16)$$

Approximate solutions for $|n_2 - n_1| > 1$ can be obtained through superpositions of several single soliton solutions with different core positions x_0, provided the latter are several ζ apart.

Variation of 3.14 w.r.t. A gives an expression for the current

$$J = -e^2 \sum_{i=1}^{2} \rho_i \left(\frac{\phi_0}{2\pi} \nabla\phi_i + A \right). \quad (3.17)$$

The complete solutions of Eqs. 3.14 that satisfy the boundary conditions $\phi_i(L) =$

$2\pi(n_i - \varphi_B) + \phi_i(0)$ are of the form

$$\phi_i(x) = (\eta_1 n_1 + \eta_2 n_2 - \varphi_B)x/R + (-1)^i(1 - \eta_i)\theta(x), \tag{3.18}$$

where θ is a solution of Eq. 3.15 and $\eta_i = \rho_i/(\rho_1 + \rho_2)$. In the London gauge, φ_B has to be set to 0, and the vector potential $A = \Phi_a/L$ makes a constant contribution to the current (3.17). For the purpose of the illustration given in Fig. 3.6, it is more transparent to use a gauge where A is a δ-function at $x = 0$ so that $\varphi_B = \varphi = \Phi_a/\Phi_0$ and $A = 0$ in Eq. (3.17). While the soliton part of the solution was already considered in Ref. [131], the possibility of an additional linear phase variation was not considered there. Instead, a somewhat obscure argument led to the result that the flux in the ring is $\eta_1\Phi_0$ for $n_1 = 1$ and $n_2 = 0$, which is true for $wd \gg \lambda^2$, but unphysical in the quasi-1D limit $wd \ll \lambda^2$.

Figs. 3.6(b)-(g) show schematic reconstructions of $\phi_{1,2}$ and θ at the flux bias points indicated by arrows in Fig. 3.6(a). Those plots also provide a simple explanation for when a state becomes unstable. Within the framework of 1-OP GL theory and in the chosen gauge, which has the advantage that the contribution of the applied flux to the superfluid velocity is included in the slope of the $\phi_{1,2}(x)$, a state becomes unstable at $|\nabla\phi| \gtrapprox 1/(\sqrt{3}\xi)$. In the case discussed here, ξ_2 is sufficiently small for $\nabla\phi_2$ never to reach the critical value. Upon increasing φ, a soliton enters the ring and increases n_1 whenever $\nabla\phi_1$ approaches the critical value between already existing solitons, where it is largest. When φ is ramped down again, a soliton leaves the ring whenever $\nabla\phi_1$ becomes too negative in the core of a soliton. For a discussion of the transition sequence leading to the particular Φ_a–I curve discussed in this section see the caption of Fig. 3.6.

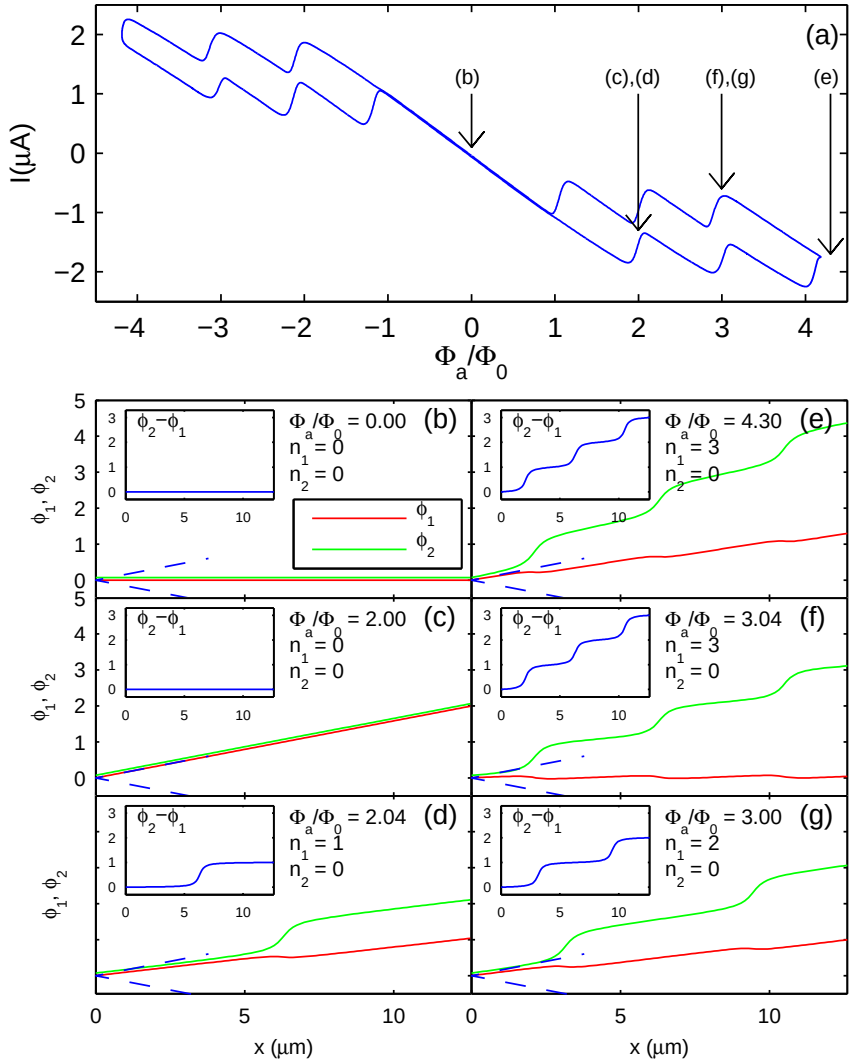

Figure 3.6: Reconstructions of the absolute and relative phases $\phi_{1,2}$ and θ at the flux bias points indicated by arrows in panel (a). The dashed lines in (b) - (g) indicate the critical slope of ϕ_1. Initially, $n_1 = n_2 = 0$, $\varphi = 0$ and $\theta = 0$ (b). Upon increasing φ, $\phi_1 = \phi_2$ vary linearly until the critical value of $\nabla\phi_1$ is reached (c). At this point, a soliton enters so that $n_1 = 1$ (d), thus reducing $\nabla\phi_1$ so that φ can be increased further before the next one enters. At the largest value of φ, $n_1 = 3$ so that there are three solitons in the ring (e). As φ is reduced again, $\nabla\phi_1$ eventually reaches its negative critical value in the core of a soliton (f), so that the solitons decay one by one (g) until the ring returns to the $n_1 = n_2 = 0$ state (b).

Chapter 4

Multiple fluxoid transitions in mesoscopic superconducting rings

Hendrik Bluhm, Nicholas C. Koshnick, Martin E. Huber, Kathryn A. Moler,
submitted to Physical Review B.

Abstract

The authors report magnetic measurements of fluxoid transitions in mesoscopic, superconducting aluminum rings. The transitions are induced by applying a flux to the ring so that the induced supercurrent approaches the critical current. In a temperature range near T_c, only a single fluxoid enters or leaves at a time, leading to a final state above the ground state. Upon lowering the temperature, several fluxoids enter or leave at once, and the final state approaches the ground state, which can be reached below approximately 0.5 T_c. A model based on the widely used time dependent Ginzburg-Landau theory for gapless superconductors can only explain the data if unphysical parameters are used. Heating and quasiparticle diffusion may be important for a quantitative understanding of this experiment, which could provide a model system for studying the nonlinear dynamics of superconductors far from equilibrium.

The dynamics of phase slips (PS) in quasi-1D superconducting wires has long been studied intensively. Most observed phenomena have been explained with phenomenological models[127, 68] and the time-dependent Ginzburg-Landau theory (TDGL) for gapped superconductors [79], often with good quantitative agreement [133]. However, in those wires with diameter d of typically a few μm, the quasi-1D limit $\xi(T) \gtrsim d$ and $\lambda(T) \gg d$ was only accessible very close to the critical temperature T_c, where the coherence length ξ and penetration depth λ diverge. Due to various approximations, the microscopic validity of most of the theoretical models employed is also limited to the vicinity of T_c. Modern e-beam and nanotemplating techniques yield superconducting wires which remain quasi-1D down to $T = 0$, and thus give access to the superconducting dynamics at low temperature without loosing the significant simplifications of the 1D limit. A better understanding of those dynamics is interesting both for its own sake and for device applications, such as microbridge SQUIDs[61] or nanowire single photon detectors [7].

We have probed the dynamical evolution of the order parameter in mesoscopic Al rings at temperatures $T = 0.15 \ldots 0.9\ T_c$. Upon increasing the magnetic flux Φ_a threading a ring, the circulating supercurrent I increases quasistatically until it approaches the critical current, and the ring switches rapidly to a more stable state. We find that near T_c, the phase winding number n of the order parameter $\psi(x) = |\psi|e^{inx}$ changes by $\Delta n = 1$ at each transition, which can leave the ring in a metastable state well above the ground state. At lower T, Δn increases, and the final state approaches the ground state, while static states persist over a larger range of applied flux. Below $T \approx 0.5\ T_c$, the ring decays into the ground state over an increasing range of flux bias points. Such multiple fluxoid transitions were first observed in Ref. [107] for rings not quite in the 1D-limit, theoretically explained based on the gapless TDGL equations [137], and studied further in Ref. [138]. Contrary to our work, the previous experimental results[138, 107] focus on the effect of applying a field H_a not much smaller than the critical field, rather than the temperature dependence. Multiple fluxoid transitions were also found to be manifest heat capacity measurements on an array of rings in Ref. [23], where a qualitative explanation in

terms of static GL solutions obtained from a relaxation algorithm was given. Refs. [14] and [132] contain further related theoretical work on state selection and the effect of fluctuations on the dynamics of mesoscopic superconducting rings, albeit in a different parameter range. The TDGL model in Refs. [138] and [137] can only reproduce our and previous ring data by choosing a numerical constant which is inconsistent with microscopic theory and transport measurements in the resistive state. The gapped TDGL theory may overcome this inconsistency. However in Al, both versions of TDGL are justified only extremely close to T_c, and we estimate that the neglected heating and quasiparticle (QP) diffusion may be important in our experiment. Lacking a tractable theory for superconducting dynamics far from T_c, it is common to use TDGL, sometimes well below T_c and in the gapless version. Thus, it is of considerable interest to understand to what extent those theories are adequate outside their theoretical range of validity, and to develop better theories. Experiments such as ours can be used for validation.

Unlike transport measurements on superconducting wires, where voltage reflects the mean phase winding rate, our experiment probes when phase unwinding ceases, once started. Thus, we explore fast dynamics without a high measurement bandwidth. Furthermore, DC transport measurements are prone to thermal runaway effects at low T, where the critical current is large and cooling is inefficient. In our case, heating is also significant, but localized in space and time due to the finite number of PS's. The absence of leads eliminates the need to consider proximity effects and boundary conditions at the contacts.

The results reported here are from 13 rings with radii $R = 1$ and 2 μm and line width $w = 70$, 115, 140 and 180 nm, measured in a single cool down. We measured I as a function of Φ_a and T by positioning a scanning SQUID microscope[17] over each ring individually. The samples were made by e-beam lithography using PMMA resist and liftoff. The 60 nm thick Al film was deposited using e-beam evaporation at a pressure of 10^{-7} mBar and a rate of 35 Å/s. Using $\xi_0 = 1.6$ μm for pure bulk Al[95] and $\xi(0) = 140$ to 180 nm depending on w, obtained as described below [see also Fig. 4.1(g)], we infer a mean free path of $l_e = 1.4\xi(0)^2/\xi_0 = 17$ to 28 nm. The measured T_c is 1.25 K.

Our SQUID sensor is designed as a susceptometer as discussed in Refs. [55] and [78]. We positioned one of its pickup loops over a ring and recorded its response while sinusoidally varying Φ_a, generated by an on-chip field coil, at 0.6 Hz. To isolate the flux generated by I, we subtracted a background measured by retracting the SQUID from the sample. For each ring, we took 40 such Φ_a–I curves at each T, in steps of 10 mK — a total of more than 40,000 field sweeps containing 550,000 transitions.

We also collected data at a smaller Φ_a-amplitude, so that fluxoid transitions only occurred near T_c, to extract $\lambda^{-2}(T)$ and $\xi(T)$ [Fig 4.1(f, g)], as described in chapter 3. Using fifth order rather than cubic polynomials to fit the low T Φ_a–I curves accounts for corrections to 1D GL at low T [8], and for imperfections in the rings, whose effect is biggest at large I. We also corrected for partial screening of the applied flux.

Fig. 4.1 shows a few individual field sweeps. Each branch of a Φ_a–I curve represents the response $I_n(\varphi \equiv \Phi_a/\Phi_0)$ of a state with fluxoid number n, with a linear response around $\varphi = n$, and a curvature caused by pair breaking at larger $\varphi - n$. $\Phi_0 = h/2e$ is the superconducting flux quantum. Since $w \ll R$ and $H_a \ll H_{c2}$, I_n and the transition points only depend on $\varphi - n$ to high accuracy. In the GL regime, $I_n(\varphi) = -(wd\Phi_0/2\pi R\mu_0\lambda^2)(\varphi-n)(1-(\xi^2/R^2)(\varphi-n)^2)$. At lower T, deviations from the cubic form become noticeable.

We have extracted the position φ_t of each transition and n for each branch, and computed $\phi_t(T) \equiv \langle|\varphi_t - n_i|\rangle$ by averaging over all transitions in each set of field sweeps. n_i and n_f are the n before and after each transition, as illustrated in Fig. 4.1(d). The ≤ 50 mΦ_0 rms-scatter of $|\varphi_t - n_i|$ around ϕ_t, which is partly due to sensor vibrations, is negligible for our purpose. The observed frequencies of $\Delta n \equiv |n_i - n_f|$ values yield a probability distribution as a function of T for each ring, as shown in Fig. 4.1(e). Since we find at most two consecutive integer values of Δn at any given T, the distribution is fully characterized by its mean $\langle\Delta n\rangle(T)$ [Fig. 4.2].

A GL stability analysis neglecting screening effects and fluctuations predicts $\phi_t = \sqrt{R^2/\xi_{GL}^2 + 1/2}/\sqrt{3} \approx R/\sqrt{3}\xi(T)$ [138]. In practice, ϕ_t as shown in Fig. 4.2 varies significantly between nominally identical rings, and is up to 30 % smaller than the measured value of $R/\sqrt{3}\xi(T)$, with the largest deviation for the smallest w. The variations suggests that imperfections contribute significantly to this discrepancy,

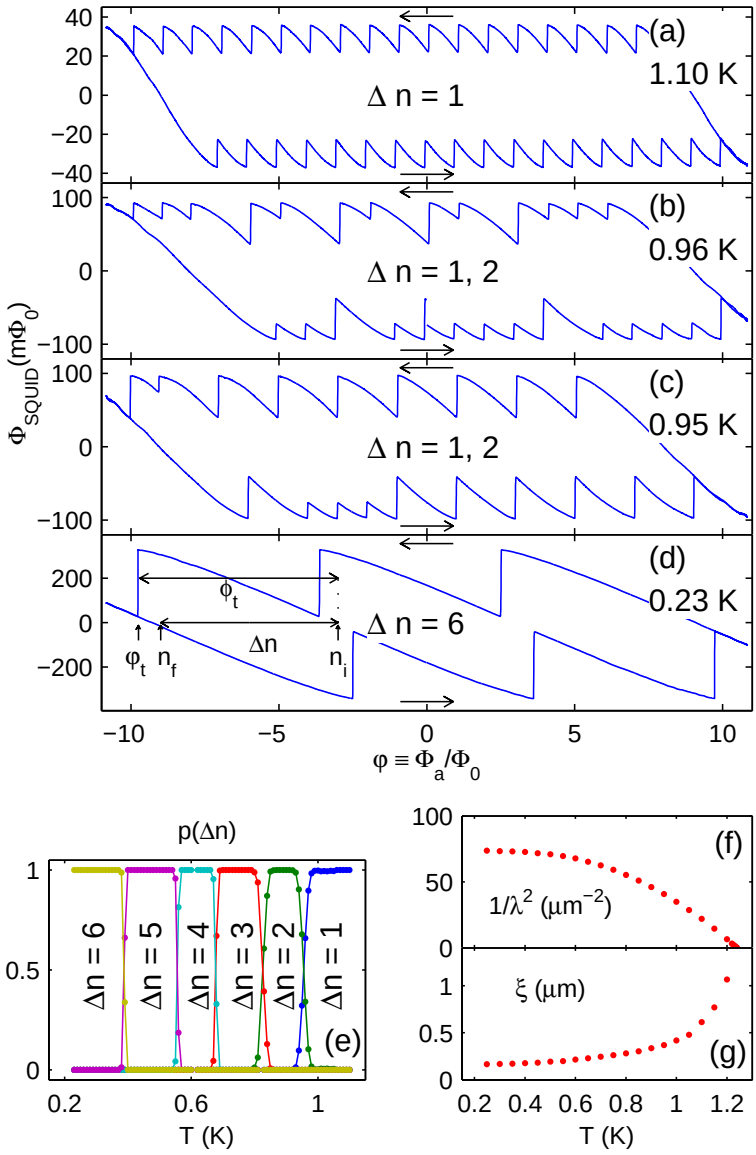

Figure 4.1: (a)-(d) Typical single-sweep Φ_a–I curves for a $R = 2\mu$m, $w = 180$ nm ring. The ring current I is proportional to the SQUID response Φ_{SQUID}, with mutual inductance $M_{coup} \approx 1.2\ \Phi_0$/mA for this ring size. At 1.1 K (a), $\Delta n = 1$ always. Around 0.96 K (b) and 0.95 K (c), $\Delta n = 2$ transitions become increasingly likely. At 0.28 K (d), $\Delta n = 6$, and the ring decays close to the ground state at each transition. The arrows indicate the field sweep direction and illustrate Δn, n_i, n_f and ϕ_t for the transition at $\varphi_t = -9.7$. (e) Probabilities for a change Δn in the fluxoid number. (f),(g) λ^{-2} and ξ as a function of T.

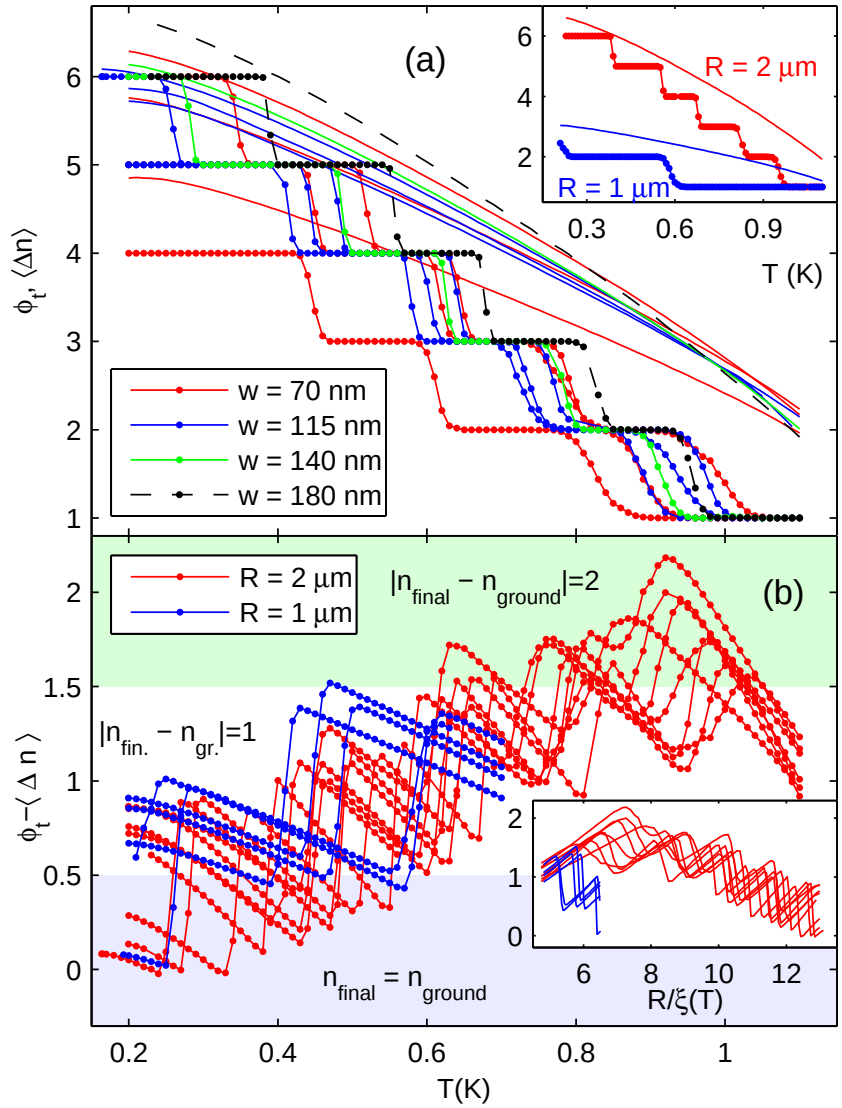

Figure 4.2: (a) Mean transition point ϕ_t (lines only) and $\langle \Delta n \rangle$ (lines with dots, each dot representing one dataset of 40 field sweeps). The inset shows the same data for just the ring from Fig. 4.1 and a $R = 1$ μm ring. (b) ϕ_t - $\langle \Delta n \rangle$ as a function of temperature for all 13 rings. The three shaded regions indicate the difference $|n_f - n_{ground}|$ between the n of the final and the ground state. Since $\phi_t - \langle \Delta n \rangle = \pm(\varphi_t - n_f)$, it encodes both $|n_f - n_{ground}|$, and the dependence of the final state on how far from an integer flux bias point a transition occurs. Comparison with the inset shows that $\phi_t - \langle \Delta n \rangle$ depends directly on the temperature rather than $R/\xi(T)$.

but a deviation from GL theory far below T_c and thermal activation or tunneling may also play a role. The temperatures at which Δn changes also show significant scatter. However, they correlate strongly with the value of ϕ_t at that point for similar T. Consequently, the curves of $\phi_t(T) - \langle\Delta n\rangle(T) = \pm(\varphi_t - n_f)$ from all rings [Fig. 4.2] approximately collapse into a band whose width of ≈ 1 is largely due to the discreteness of $\langle\Delta n\rangle$. Below 0.5 T_c, $\phi_t - \langle\Delta n\rangle < 1/2$ can occur, which implies that the final state is the ground state with $|\varphi_t - n_f| < 1/2$. The lower T, the larger is the range of φ_t over which the ground state is reached. The absence of a clear w dependence of $\phi_t - \langle\Delta n\rangle$ vs. T indicates that the effect of the self inductance and the thermal activation barrier, both of which are proportional to wd, is small.

The results show no significant dependence on sweep frequency from 0.6 to 9.6 Hz. One concern is heating from the ∼5 GHz, ∼5 mΦ_0 Josephson oscillation applied to the rings by the SQUID. Varying the pickup loop–ring inductance M_{coup} by a factor 5 by retracting the SQUID about 2 μm had no significant effect. However, when the sensor chip touched the sample substrate, $\phi_t(T)$ flattened slightly below 0.35 K, changing by 0.1 at 0.2 K. Since this effect is negligible, the data was acquired with the SQUID touching the sample to avoid variations of M_{coup} due to scanner drift and vibrations.

We now turn to discussing our results in terms of the TDGL equations for gapped superconductors:

$$\frac{u}{\sqrt{1+\gamma^2|\psi|^2}}\left(\frac{\partial}{\partial t} + iV + \frac{\gamma^2}{2}\frac{\partial|\psi|^2}{\partial t}\right)\psi = (\nabla - i\mathbf{A})^2\psi + (1-|\psi|^2)\psi \tag{4.1a}$$

$$\nabla^2 V = \nabla\cdot\mathrm{Re}(\psi^*(-i\nabla + \mathbf{A})\psi), \tag{4.1b}$$

where $\gamma = 2\tau_E\Delta_0(T)/\hbar$. $\Delta_0(T)$ is the equilibrium gap, V the electrostatic potential, and τ_E the inelastic electron-phonon scattering time. Without magnetic impurities, theory predicts $u = \pi^4/14\zeta(3) = 5.79$ [79]. Eqs. (4.1) are written in dimensionless variables, as defined in Ref. [96]. We only note that the unit of time is $\tau_{GL} = 2k_BT\hbar/\Delta_0^2$, and the dimensionless ring circumference is $2\pi R/\xi(T)$. The latter might lead to an indirect T-dependence. However, Fig. 4.2(b) shows only a weak

R-dependence of the range of possible $\phi_t(T) - \langle\Delta n\rangle(T)$, whereas plotting $\phi_t - \langle\Delta n\rangle$ against $R/\xi(T)$ (inset) gives two distinct bands. Thus, the T-dependence of γ is more important than that of $R/\xi(T)$, to the extent that Eqs. (4.1) are applicable.

The mechanism underlying multiple PS's in mesoscopic rings was analyzed in Refs. [137, 138], based on numerical solutions of Eqs. 4.1 with $\gamma = 0$. Ref. [137] identifies two timescales: the duration of a single PS, τ_ϕ, and the relaxation time $\tau_{|\psi|}$ of $|\psi|$. If $\tau_\phi \lesssim \tau_{|\psi|}$, the phase may unwind by several 2π before $|\psi|$ can recover after the first PS. Further analysis for wires with finite γ[96] shows that τ_ϕ is related to the voltage drop $\Delta V = IR_{PS}$ across the PS center via the Josephson relation: $\tau_\phi = \Phi_0/\Delta V$, where R_{PS} is the resistance of the region around the PS over which the electric field decays and the QP current is converted to supercurrent. The extent of this region is given by the charge imbalance length $\Lambda_{Q^*} \propto \sqrt{\gamma/u}\xi(T)$. One obtains $\tau_\phi \propto \sqrt{u/\gamma}\tau_{GL}$ and $\tau_{|\psi|} \propto \gamma u \tau_{GL}$. The above expressions are valid for $\gamma \gg 1$. For $\gamma \leq 1$, one should replace γ with 1.

If treating u as a phenomenological adjustable parameter and setting $\gamma = 0$, one thus finds that $\tau_\phi/\tau_{|\psi|}$ decreases with increasing u, so that a larger u leads to larger Δn [137]. Reasonable agreement with a previous experiment at 0.4 K was obtained for u = 48 [138]. However, $u \gg 6$ is inconsistent with microscopic theory and experiments in the resistive state of quasi-1D superconducting wires [64, 133]. Those show that except very close to T_c, $\xi < \Lambda_{Q^*} \propto |T - T_c|^{-1/4}$. Some experiments even found a constant Λ_{Q^*}. When using Eqs. (4.1) with $\gamma = 0$, this implies $u < 1$ and that u decreases with decreasing T [137]. For example, Eqs. (4.1) with $u = 0.01$ and $\gamma = 0$ have been used to model the resistive state [64].

This inconsistency in the effective u arises because γ is negligible only in the gapless limit, where phonon (or magnetic impurity) induced pair breaking causes a fast reaction of the QP population to order parameter variations. For pure Al, this limit only applies for $T > T_c - 10^{-10}$ K. An increase of $\gamma \propto \sqrt{|T - T_c|}$ with decreasing T on the other hand both reduces $\tau_\phi/\tau_{|\psi|}$ and increases $\Lambda_{Q^*}/\xi(T)$, in qualitative agreement with both ring and resistive-state experiments. However, Eqs. (4.1) neglect heating and QP diffusion, which is valid for $\tau_\phi, \tau_{|\psi|} \ll \tau_E$. Thus, even accounting for the slow charge imbalance relaxation by allowing $\gamma \neq 0$ only extends

the theoretical validity to $T_c - T < 0.1$ mK for Al [142] [1].

The observation that $\varphi_t - n_f$ is nearly independent of R implies that the current after a transition is approximately inversely proportional to R. For wires carrying a quasi-dc bias current I on the other hand, phase slipping stops once I drops below some limit I_{c1}, at which $\tau_\phi = \Phi_0/R_{PS}I_{c1} \approx \tau_{|\psi|}$ [96]. Within the TDGL picture discussed above, this finite length effect could be explained if the normal-like length determining R_{PS} is set by circumference rather than Λ_{Q^*}, which is formally plausible since $2\Lambda_{Q^*} > 2\pi R$ at $T = 0$. However, QP's can only diffuse a distance $\sqrt{D\tau_\phi} \ll \pi R$ during a single PS, so that it seems questionable if the whole ring can contribute to R_{PS}. Alternatively, the local reduction of the critical current at the PS center could increase as more PS's occur, so that larger rings holding more fluxoids have a smaller final current. Well below T_c, where $\Delta_0 \gg k_B T$, the electronic heat capacity $c(T)$ is very small, while the kinetic energy density is large. Therefore, dissipating the latter in a PS will lead to significant heating, i.e. excitation of the energy mode of the QP population, which increases for larger R. Thermalization with the lattice occurs on the scale of $\tau_E \geq 50$ ns [142], whereas assuming that R_{PS} is at least that of a ring section of length ξ gives $\tau_\phi \lessapprox 10$ ps. Thus, the electrons are approximately a closed system. If the kinetic energy was converted to homogeneous heating, the resulting electronic temperature would be given, very roughly, by $\max(T, 0.8\text{ K})$, because $c(T)$ is small for $T \lessapprox 0.5T_c$. At this temperature, ϕ_t is still rather large, so that uniform heating would lead to smaller Δn than observed. However, given the short diffusion length $\sqrt{D\tau_\phi} \sim \xi \ll 2\pi R$, hot QP's will remain localized so that diffusive cooling may affect $\tau_{|\psi|}$.

A general description of time dependent superconductivity, similar to the Usadel equations for the static case, was derived in Ref. [142]. Unfortunately, the resulting system of equations for Δ, the Green's functions and electron distribution is rather complex. Approximate solutions for specific cases were studied in Refs. [12, 122]. Similar computations might allow a direct comparison between our data and microscopic theory. A much simpler first step could be a similar study as in [137] using

[1] For some common low-T_c superconductors with shorter τ_E, Eqs. (4.1) hold over a much larger temperature range.

Eqs. (4.1), but with γ rather than u as free parameter. Heating and QP diffusion could be accounted for through a local effective temperature governed by the heat equation.

In conclusion, we have shown experimentally that the final state after a field induced fluxoid transition in mesoscopic rings approaches the ground state for $T \to 0$. While localized heating likely is important, our results cannot be explained with uniform heating. Time dependent Ginzburg-Landau theory for gapped superconductors might give an adequate phenomenological model, however it is not microscopically justified in the experimental temperature range. Although our experiment is conceptually rather simple, a quantitative explanation is intriguingly complex and probably requires the incorporation of QP diffusion. Such a model may also provide insight in localized nonequilibrium effects on the superconducting dynamics in other cases, such as vortex motion or flux avalanches.

This work was supported primarily by NSF Grant No. DMR-0507931, with additional support by DMR-0216470, ECS-0210877 and PHY-0425897 and by the Packard Foundation. Samples were fabricated at the Stanford Nanofabrication Facility of NNIN supported by NSF Grant No. ECS-9731293. We would like to thank Denis Vodolazov and Jorge Berger for useful discussions and comments.

Chapter 5

Persistent currents in normal metal rings

5.1 Theoretical background

5.1.1 Introduction

Since it was realized that persistent currents should exist in normal metal rings in the diffusive regime, they have attracted tremendous theoretical attention. This interest was fueled further by only a handful of experiments, some of which raised more questions than they answered. The only published measurement of persistent currents in single normal metal rings [29] found a signal that was up to two orders of magnitude larger than the theoretically expected result. Experiments on a ballistic ring [89] and ensembles of 30 to 10^7 rings (see section 5.2) were generally in better accord with theory, but many open questions remain. Thus, there is a definite need for further experiments. Due to the very small signals and the inaccessibility of the effect with regular transport measurements, such experiments are considered as very difficult. Addressing this need was one of our motivations for implementing a scanning SQUID microscope in a dilution refrigerator and pushing for the required sensitivity. Up to the point of writing, this instrument allowed us to measure 33 individual Au rings in the last, most successful cooldown, and many more in earlier attempts without

any positive results. The magnetic response of some of the rings contains a flux-periodic component which is fully consistent with the theoretically expected behavior of persistent currents.

In the remainder of this introduction, I will try to convey some physical intuition for persistent currents in mesoscopic systems, and motivate the interest they have received over the years. In sections 5.1.2 and 5.1.3, I will give a brief overview of the theoretical results that are most relevant for comparison to the experiment. Given the vast body of literature on the subject, it will be far from being complete. Section 5.2 will give a more comprehensive summary of previous experimental results.

It was first pointed out by Byers and Yang [26] in connection with superconducting pairing that all thermodynamic quantities of an ensemble of electrons in a ring-like structure are periodic in the flux Φ threading the center. The vector potential due to this flux can be transformed into a phase factor $e^{i2\pi\Phi/\phi_0}$ in the boundary conditions for the single particle wave functions through a gauge transformation. Thus, changing the flux by an integer multiple of $\phi_0 \equiv h/e$ has no effect. While Ref. [26] explicitly neglected mesoscopic fluctuations arising from the discrete nature of electronic levels in small samples, it is exactly those fluctuations that cause many of the known mesoscopic effects.

One of the experimentally accessible thermodynamics quantities in which they can be manifest is the ground state current $I(\Phi)$ circulating a ring as a result of a static applied flux Φ. This is not to be confused with the transient current due to a time dependent flux, which decays over the inductive L/R time of the ring. For a typical mesoscopic ring, L/R is in the picosecond range. Loosely speaking, the equilibrium persistent current is what is left of this induced current when the electrons have relaxed as close to a zero-current state as is consistent with the discrete energy levels.

Theoretical interest in this phenomenon was initially motivated by several factors. Since it represents an equilibrium property rather than the response to an excitation, it is (or should be) relatively simple to calculate. In particular, since

$$I = -\frac{\partial F}{\partial \phi},$$

it directly reflects the flux dependence of the free energy F.

Because the total energy is just the sum of the energies of the individual levels, the total current of all levels reflects correlations between the flux dependence of the individual energy levels. One typically finds that the total current corresponds to that of relatively few electrons at the Fermi energy, which implies strong anticorrelations between nearby levels. In strictly one-dimensional, disordered rings, a surprisingly detailed theoretical insight into such correlations can be gained using the transfer matrix technique. (See, for example [32]). Since they are accessible with relatively simple theoretical techniques, one-dimensional rings are also a good source for an intuitive understanding. In the absence of the disorder, computing their persistent current as a function of flux and chemical potential or electron number is a straightforward exercise. Since the results are laid out in some detail in Ref. [31], I will not repeat them here. The probably most important conclusion is that the typical magnitude of the current corresponds to a single electron circulating the ring at the Fermi velocity, i.e.

$$I = \frac{ev_F}{L}.$$

Such 1D results may be directly relevant for experiments on 2DEG rings, which can have few transverse channels and reach the ballistic limit ($l_e \gtrsim L$). The metallic rings of the experiments discussed in section 5.3 on the other hand are in the diffusive regime with many transverse channels, which is more complicated.

Before reviewing some of the related theoretical results in the next section, I will discuss some basic concepts. Due to the periodic nature of $I(\Phi)$, it is customary and natural to decompose persistent currents (and other flux dependent quantities) into their harmonics, I_m. Since higher harmonics are associated with electron paths circulating the ring several times in a semiclassical picture, they (and therefore any sharp features in the $\Phi - I$ relation) are more susceptible to disorder, temperature etc. Consequently, the first and second harmonics are the experimentally most accessible ones. However, since there are some fundamental differences in the physics that governs odd and even harmonics, it is sometimes essential to consider both the first and second harmonic, I_1 and I_2.

Since the $\Phi - I$ relation of any given ring depends on the particular realization of disorder, theoretical work usually deals with ensemble averages $\langle I_m \rangle$ and the fluctuations $\langle I_m^2 \rangle$. Those numbers characterize the distribution of observed amplitudes if one measures many different rings individually. This distribution is expected to be Gaussian in the diffusive regime ($l_e \ll L \ll \xi$, where ξ is the localization length) and to become log-normal at the onset of localization ($L \sim \xi$) [100]. Due to this randomness of the persistent current, a measurement of a single ring can only give order-of-magnitude information. If an experiment averages over an ensemble of N rings, the distribution of the results is given by

$$\begin{aligned} \langle I_{ensemble} \rangle &= N \langle I_{single} \rangle \quad \text{and} \\ \left(\langle I_{ensemble}^2 \rangle - \langle I_{ensemble} \rangle^2 \right)^{1/2} &= \sqrt{N} \left(\langle I_{single}^2 \rangle - \langle I_{single} \rangle^2 \right)^{1/2}. \end{aligned}$$

Thus, such an ensemble measurement will reflect $\langle I \rangle$, provided $N \gg \langle I^2 \rangle / \langle I \rangle^2$. If this condition does not hold, the interpretation of the experiment may be ambiguous, since it is not clear if the result has to be scaled by N or $\sqrt{N}$ to obtain a single-ring current.

5.1.2 Noninteracting electrons in a diffusive ring

Riedel and Von Oppen [115] have computed $\langle I_1 \rangle$ and $\sqrt{\langle I_1^2 \rangle}$ including their temperature dependence for cylinders, i.e. rings with a finite extent along the symmetry axis, in the diffusive regime at a fixed chemical potential μ. Their main results are the basis for comparison of our experimental results with theory. They find to a good approximation in the relevant temperature range

$$\sqrt{\langle I_1^2 \rangle} = \frac{E_c}{\phi_0} e^{-k_B T / E_c} = 0.52 I_0 e^{-k_B T / E_c}, \tag{5.1}$$

which does not include spin. Higher harmonics enter with a $m^{-3/2}$ prefactor and thus are practically negligible. The current scale $I_0 \equiv e l_e v_F / L^2$ can be identified with the current of a single electron traveling diffusively around the ring. Writing it as E_c / ϕ_0 is reminiscent of the fact that $E_c \equiv \pi^2 \hbar D / L^2$ is proportional to the Thouless

energy. The latter reflects the sensitivity of a single particle level to the boundary conditions in a system of size L [48]. However, this correspondence appears to be somewhat oversimplified, since a detailed analysis of the single level currents suggests that the total response is due to the contributions of the last M_{eff} levels [115]. Those M_{eff} levels are separated in energy by the correlation energy E_c. One finds that the correlations between energy levels at different energies cause an oscillatory variation of the persistent current as a function of the chemical potential μ on the scale of E_c in a given sample. These correlations also explain the scale of the temperature dependence: When the thermal broadening of the Fermi surface leads to averaging over anticorrelated levels more than E_c apart, the total persistent current is suppressed. One can also relate the exponent in Eq. 5.1 to the thermal length $L_T \equiv \sqrt{hD/k_BT}$: $k_BT/E_c \propto (L/L_T)^2$. L_T is just the distance two electrons separated by k_BT can diffuse until their relative phase changes by 2π. Thus, the phase sensitivity around the ring is thermally smoothed out if $L \gtrsim L_T$.

Eq. 5.1 is valid for spinless electrons. Taking spin into account increases $\sqrt{\langle I_1^2 \rangle}$ by a factor 2, since each spin contributes the same amount for any given realization of spin independent disorder. Based on a heuristic argument backed up with a strictly 1D calculation in Ref. [94] (see also [50]), one may expect an additional factor 1/2 for strong spin-orbit scattering ($l_{so} \lesssim L$), thus giving the same overall result as Eq. 5.1. A very similar result with an additional factor $1/\sqrt{d}$ in the prefactor was already given in Ref. [33], where d is the dimensionality of the sample with respect to l_e.

According to Ref. [33], the average h/e current is exponentially small in L/l_e:

$$\langle I_1 \rangle = \frac{2}{\pi} \sqrt{M_{eff}} e^{-L/2l_e} \frac{e l_e v_F}{L^2}.$$

For our rings, it is significantly smaller than $\sqrt{\langle I_1^2 \rangle}$. However, as Yoe Imry pointed out, it may not be entirely beyond experimental reach, since the effective number of channels $M_{eff} = Ml_e/L$ in the prefactor can be fairly large. This component is supposed to decay over a temperature scale corresponding to the longitudinal level spacing $\Delta_1 = hv_F/L \propto L/l_eE_c$ and oscillate as a function of the chemical potential μ over the same scale. Thus, one may expect it to be even smaller if an average over μ

is taken.

The contributions to the persistent current discussed so far are insensitive to whether the ensemble averaging is carried out in the canonical or grand-canonical ensemble, i.e. whether electrons are allowed to enter or leave the ring as energy levels cross μ. Several papers [2, 139, 121] predict an additional, Cooperon-related contribution $\langle I_{2m}\rangle \sim \Delta_M/\phi_0$ to the ensemble average of even harmonics, which occurs only in the canonical ensemble. Due to the small amplitude and the correspondingly small temperature scale of $\Delta_M/\hbar k_B$, this is of little experimental relevance in metallic rings. An enhancement of ensemble averages in the canonical compared to the grand canonical ensemble was also observed in large scale numerical simulations in Ref. [100], however with a parametrically different parameter dependence than the Cooperon contribution: $\langle I_2\rangle \propto ev_F l_e/\sqrt{M_{eff}}L^2$.

5.1.3 Interaction effects on $\langle I_2\rangle$

A range of papers discuss the effect of various interactions on persistent currents. Those calculations were partly motivated by the experimental results of Levy et *al.*, [83], which showed an $h/2e$ ensemble average $\langle I_2\rangle$ that was much larger than the non-interacting electron results discussed in the preceding section.

Since electron-electron interactions always involve at least two electrons, each of which picks up a phase of 2π per ϕ_0, interaction effects are usually manifest in the even harmonics $\langle I_{2m}\rangle$. The effect of direct electron-electron interactions characterized by a dimensionless coupling strength λ has been addressed in Ref. [5]. The authors find

$$\langle I_2\rangle = \frac{8\lambda}{3\pi} e^{-\frac{\pi^2 k_B T}{3E_c}} I_0. \tag{5.2}$$

For attractive interactions ($\lambda < 0$) such as the BCS interaction, one finds a diamagnetic response, whereas repulsive interactions such as the Coulomb force result in a paramagnetic response. Estimates of either kind of interaction for non-superconducting metals lead to $|\lambda| \lessapprox 0.1$ [6], which is about a factor of 5 too small to explain the experimental result of Ref. [83]. Ref. [121] suggests that the effect of repulsive interactions can be also interpreted as the consequence of a local enforcement

of charge neutrality. A similar result to Eq. (5.2), however with a parametrically larger prefactor, was reported in Ref. [120]. This calculation is based on a BCS Hamiltonian, which leads to interaction induced correlations between levels up to ω_D from the Fermi surface, where ω_D is the cutoff energy for the interactions. However, it was subsequently argued that this result is due to an unjustified approximation that violates gauge invariance [47].

Schwab [123] has considered an interaction of non-magnetic two level systems (TLS) with the local electron density. Since the latter has a periodic flux dependence, this mechanism also contributes to the persistent current. The result is similar to Eq. (5.2) with the coupling constant λ determined by the concentration of defects with suitable parameters. It appears that a 2 ppm concentration of such TLS could account for the experimental result of Ref. [83], but since little is known about such defects in microfabricated structures, this comparison is inconclusive.

Schwab and Eckern [124] predicted that an $h/2e$ component of the ensemble average may also arise from interactions of electrons with magnetic impurities. Their result is again similar to Eq. (5.2) with an interaction constant λ proportional to the impurity concentration and their susceptibility. For most of their calculations, they assumed an equilibrium susceptibility, which results in a $1/T$ temperature dependence of the persistent current. In a later paper [123], Schwab mentions that this is the reason why their theory was not suggested as an explanation of the large ensemble average measured in Ref. [83], where no low-T divergence was observed. However, it seems that the $1/T$ dependence obtained in Ref. [124] will be cut off by saturation of the spin once its electron-interaction induced level splitting becomes comparable to k_BT. The onset of Kondo physics should also lead to a cutoff for temperatures below the Kondo temperature [124]. Since the electrons provide most of the dissipation thermalizing a spin, it seems plausible that dynamic effects such as a retarded interaction may play a role, too. It has been demonstrated after publication of Ref. [124] that magnetic impurity concentrations as small as 0.1 ppm can cause excess dephasing [109, 16]. Furthermore, the rings measured by Levy *et al.* [83] were made of Cu, and there is strong evidence that Cu forms a magnetically active surface oxide [141]. Some of the earlier persistent current measurements did report

Ref.	[29]	[29]	[29]	[67]	[83]	[40]	[114]	[41]	[89]	[113]
Material	Au	Au	Au	Au	Cu	Ag	GaAs	GaAs	GaAs	GaAs
N	1	1	1	30	10^7	10^5	10^5	10^5	1	16
L (μm)	7.5	12.6	8	8	2.2	4	8	5.2	8.5	12
l_e (nm)	70	70	70	87	20	40	3000	3000	11000	8000
I_1 (nA)	30	3	6	0.35					4	0.35
I_2 (nA)				0.066	0.4	0.33	1.5	0.25		
I_0 (nA)	0.27	0.1	0.24	0.3	1.1	0.56	0.7	2	5	1.2
T_1 (mK)			20	166						
T_2 (mK)				89	80	39	190			
E_c/k_B(mK)	44	16	38	51	168	85	310	930		1320

Table 5.1: Summary of previous persistent current measurements. N: number of rings. L: ring circumference. I_1: amplitude of h/e signal. I_2: amplitude of $h/2e$ signal. $T_{1,2}$: temperatures over which $I_{1,2}$ decay exponentially. $I_0 = ev_F l_e/L^2$ (or ev_F/L for Ref. [89], where $l_e > L$), $E_c = \pi^2\hbar D/L^2$. The sign of I_2 was diamagnetic in each experiment.

a saturation of the dephasing length at relatively high temperatures, indicating that magnetic impurities indeed were present. Thus, it appears that the effect of magnetic impurities on persistent currents deserves further attention.

5.2 Review of experimental results

Table 5.1 shows a summary of the results of all experiments on persistent currents I am familiar with. In the following, I will briefly discuss each of those experiments. A short but concise summary of experimental results is also given in Ref. [46], however it does not include the works by Mailly *et al.* [89] and Deblock *et al.* [40, 41].

The first experimental evidence for persistent currents was found by Levy and coworkers [83] in an ensemble of 10^7 Cu loops. This experiment motivated a lot of the theoretical work on diffusive rings with many transverse channels. At the time of the experiment, the absence of an h/e periodic signal was surprising, but has subsequently been understood as period-halving due to ensemble averaging. The diamagnetic sign of the zero field response could only be determined without ambiguity

for the cubic nonlinear susceptibility. However, since most theory predicts only a small content of higher harmonics in the Φ_a–I curve, it seems very likely that this implies a diamagnetic sign for the linear susceptibility at $\Phi_a = 0$ as well.

The only experiment on individual metallic rings until now was carried out by Chandrasekhar *et al.* [29]. Of all experiments discussed here, its results deviate by far the most from theoretical expectations. At the same time, the sensor background appears to have been a serious problem - it was smooth enough to attempt a distinction from the persistent current signal only for some samples. A follow up experiment on 30 Au rings [67] gave results that are much closer to theoretical expectations.

Mailly *et al.* [89] measured a single ring fabricated in a GaAs/AlGaAs heterojunction near the ballistic limit. A similar experiment by Rabaud *et al.* [113] on 16 rings, which were connected by wires but could be isolated using gates, showed that the h/e component of the persistent current is not affected dramatically by connecting the rings to a reservoir. These two experiments are the only ones that show reasonable agreement (within about a factor 2) with theory.

All the experiments discussed so far used some form of SQUID gradiometer in a non-scanning configuration. Another group of experimental studies detected the change in the resonance frequencies of microfabricated, superconducting resonators due to the magnetic and/or electric response of a large number of rings placed in their vicinity. The first of them used a 310 MHz stripline resonator which was coupled both electrically and magnetically to an ensemble of 10^5 rings in a GaAs/AlGaAs 2DEG [114]. It was followed by a very similar study at 350 MHz [41], in which the magnetic and electric response could be distinguished by placing the rings on either the capacitive or inductive parts of the resonator. The same technique was also used by the same group to study the magnetic response of 10^5 Ag rings at 217 MHz [40]. All of those experiment give a diamagnetic value for the $h/2e$ ensemble average $\langle I_2 \rangle$. For the GaAs rings [114, 41], there is no known mechanism for an attractive electron interaction which would be required to explain the sign of these results as an interaction mediated effect as predicted in Ref. [5]. Nonequilibrium noise, either from the cavity tone or other sources, could produce a diamagnetic response as suggested in Ref. [80], since spin-orbit coupling is weak in GaAs. Unfortunately, the dephasing

rate $1/\tau_\phi$ was not known well enough in those experiments to check this hypothesis.

Since the RF measurement frequencies are comparable to the dephasing and diffusion rates $1/\tau_\phi$ and $1/\tau_D$, it is not clear to what extent the theory for the static case discussed in chapter 5.1 applies. The SQUID measurements on the other hand were typically carried out at a few Hz and thus should reflect the equilibrium response. However, one should keep in mind that the GHz frequency Josephson oscillations in the SQUID junctions may couple to the rings and lead to nonequilibrium effects. This possibility has not been addressed in any of the experimental papers. For a discussion regarding our experiment, see Sec. 5.4.3.

I would like to point out that with the exception of the work by Levy *et al.* [83], all of these experiments required the subtraction of a sensor background. This could be done in a fully controlled way only for the few-ring 2DEG samples by opening the rings through application of a gate voltage. In all other cases, the background could only be distinguished from the persistent current signal through its lack of periodicity. Furthermore, only Ref. [40] attempted the extraction of a Φ_a–I curve.

In conclusion, the temperature dependence of the $h/2e$ ensemble average $\langle I_2 \rangle$ shows a reasonable agreement with the exponential decay over a $0.3E_c/k_B$ predicted by Eq. 5.2. The sign and amplitude however are not well understood. The measured signals require an unexpectedly large interaction constant to be explained with Eq. 5.2, and there is no plausible explanation for the attractive interactions implied by the diamagnetic sign of $\langle I_2 \rangle$ in GaAs.

The single-ring or few-ring experiments giving access to the h/e component give inconsistent results for metallic rings, and partly show a significant disagreement with theory. Only the reported temperature dependences are within a factor of about three from the expected decay range of E_c/k_B for both Refs. [29] and [67].

5.3 Experimental results

Hendrik Bluhm, Nicholas C. Koshnick, Julie A. Bert, Martin E. Huber, Kathryn A. Moler
(to be published)

Abstract

The authors report measurements of the magnetic response of 33 individual mesoscopic gold rings, one ring at a time, at low temperatures. The rings were characterized using a scanning SQUID microscope, which also enabled in situ measurements of the sensor background. All measured rings show a paramagnetic linear susceptibility and a poorly understood anomaly around zero field, both of which are attributed to unpaired defect spins. The response of some sufficiently small rings also has a component that is periodic in the flux through the ring. Its period is close to h/e, and its sign and amplitude vary from ring to ring. Including rings without a detectable periodic response, the amplitude distribution is consistent with predictions for the typical h/e persistent current in diffusive metal rings. The temperature dependence of the response, measured for two rings, is also consistent with theory.

When a conducting ring is threaded by a magnetic flux Φ_a, the associated vector potential imposes a phase gradient on the electronic wave functions, ψ, that can be transformed into a phase factor in the boundary conditions: $\psi(L) = e^{i2\pi\Phi_a/\phi_0}\psi(0)$, where L is the circumference of the ring and $\phi_0 \equiv h/e$ the flux quantum [26]. The h/e periodicity of this phase factor is reflected in all properties of the system. Here, we focus on the persistent current I circulating the ring, which is the first derivative of the free energy with respect to Φ_a, and thus a fundamental thermodynamical quantity. For a perfect 1D ring without disorder populated by noninteracting electrons, it is relatively straightforward to show that I will be of order ev_F/L [31]. This corresponds to the current carried by a single electron circulating the ring at the Fermi velocity v_F. A more advanced calculation [33, 115] shows that this picture still applies in the diffusive limit, i.e. for a mean free path $l_e < L$. In this case, $I \sim e/\tau_D$ is set by the diffusive round trip time $\tau_D = L^2/D$, where $D = ev_F l_e/3$ is the diffusion constant. Thermal averaging leads to a suppression of the persistent current at temperatures above the correlation energy $E_c \equiv \hbar\pi^2 D/L^2 \propto \hbar/\tau_D$.

Like many other mesoscopic effects in disordered systems, the persistent current

depends on the particular realization of quenched disorder and thus varies between particular samples. Persistent currents in diffusive rings can have either sign, so that the ensemble average of the first harmonic, $\langle I_{h/e}\rangle = 12/\pi^2\sqrt{M_{eff}}(E_c/\phi_0)e^{-2L/l_e}$, is strongly suppressed [33]. The typical value on the other hand is given by [115]

$$\langle I_{h/e}^2\rangle^{1/2} = \frac{E_c}{\phi_0}e^{-k_BT/E_c}. \tag{5.3}$$

We have not included a factor 2 for spin because our Au rings are in the strong spin-orbit scattering limit [94, 50]. Higher harmonics are generally smaller because they are more sensitive to disorder and thermal averaging. However, due to interaction effects [5, 121, 120] and differences between the canonical and grand canonical ensemble [2, 139, 121], $\langle I_{h/2e}\rangle$ is expected to be larger than $\langle I_{h/e}\rangle$.

To date, there are only very few experimental results on persistent currents, and most measurements were made on ensembles of rings [83, 114, 41, 40]. The experiments are considered challenging because persistent currents can only be measured magnetically and require a very high sensitivity. Since $|\langle I_{h/2e}\rangle| \gg |\langle I_{h/e}\rangle|$ and the mean current for an ensemble of N rings scales with N, whereas the typical current scales with $\sqrt{N}$, the ensemble measurements are dominated by $\langle I_{h/2e}\rangle$. The measured amplitudes are somewhat larger than theoretically expected, and the sign and exact origin of the response are not well understood. The h/e component has been measured in a single ballistic ring, resulting in good agreement with theory [89], and in three diffusive rings [29]. The latter experiment required the subtraction of a fitted sensor background which was much larger than the response, and showed a more or less periodic component of the signal that was one to two orders of magnitude larger than expected. A later result on an ensemble of 30 rings [67] showed a better agreement. Given the very limited amount of experimental data and sometimes poor agreement with theory, a more complete experimental investigation of persistent currents can be considered a major open challenge in mesoscopic physics.

In this paper, we report measurements of the magnetic response of a total of 33 diffusive Au rings. The use of a scanning Superconducting Quantum Interference Device (SQUID) technique allowed us to measure many different rings, one by one,

with in situ background measurements. The response of some of the rings contains a flux periodic component which is fully consistent with the predicted behavior of $\langle I_{h/e}^2 \rangle^{1/2}$. However, the total nonlinear response shows additional features, which is most likely a nonequilibrium response of impurity spins. Different frequency and geometry dependences support the distinction between those two components, and thus indicate that the periodic component does reflect persistent currents.

Our samples were fabricated using standard e-beam and optical lithography, e-beam evaporation from a 99.9999 % pure source onto a Si substrate with a native oxide, and liftoff. The 140 nm thick rings were deposited at a relatively high rate of 1.2 nm/s in order to achieve a large l_e. All the rings reported here had an annulus width of 300 nm, and radii R from 0.57 to 1 μm. From resistance measurements of wires fabricated together with the rings, we obtain $D = 0.08$ m^2/s, $l_e = 160$ nm. The dephasing length L_ϕ of our samples is yet to be characterized, however even if $\tau_\phi = L_\phi^2/D$ saturates at a relatively small value of 1 ns, L_ϕ would exceed the ring circumference by more than a factor 2 for our most important rings with $R = 0.67$ μm. Some of our rings were connected to large metallic banks [See Fig. 5.1(b)] for diffusive cooling of the heat load due to the inductively coupled Josephson oscillations of the sensor SQUID.

The experiment was carried out using a dilution-refrigerator based scanning SQUID microscope [17]. In order to prevent effects of thermal or technical radiation on the sample, all electrical lines leading into the copper shield containing the sample and scanner assembly were heavily filtered above 10 MHz (see chapter 2.1). Our sensors [62] have an integrated field coil of 13 μm mean diameter, which are used to apply a field to the sample. The sample response is coupled into the SQUID via a 4 μm diameter pickup loop. These concentric loops are near a corner of the chip, so that they can be brought to within about 1 μm of the sample. A second, counter-wound pair of coils, separated by 1.2 mm on the sensor chip, cancels the response of the SQUID to the applied field to within one part in 10^4 [78]. The sensor response to a current I in a ring is $\Phi_{SQUID} = MI$, where M is the pickup-loop–ring inductance. From previous experiments [78],[chapter 3] and modeling, we estimate $M = R^2 \times 0.3\phi_0/\mu\text{m}^2\text{mA}$. Using the measured D, Eq. 5.3 thus predicts a typical h/e response from persistent

currents of $M\langle I_{h/e}^2\rangle^{1/2} = 0.15\ \mu\Phi_0 \times e^{-k_BT/E_c}$, with a prefactor independent of R. In the following, we will specify Φ_{SQUID} in units of the superconducting flux quantum $\Phi_0 \equiv h/2e$.

To navigate around the sample and to identify individual rings, we scan the magnetic field of a current carrying meander wire fabricated on the sample. Finding the exact location of a ring is facilitated by a paramagnetic susceptibility of our metal structures, which shows up in scans of the linear response to an applied field [Fig. 5.1(a)]. Its origin will be discussed further below and elsewhere [21].

To measure the complete nonlinear response of a ring, we recorded time traces of the SQUID signal at a fixed position while supplying a sinusoidal current at typically 111 Hz to the field coil, and averaged over many cycles. This raw signal of a few mΦ_0 is dominated by nonlinearities in the sensor background and a small phase shift between the fluxes applied to the two pickup loop/field coil pairs. To extract the response of a ring, we carried out this measurement at different positions as indicated in Fig. 5.1(a), and subtracted the datasets obtained far from the ring (o) from those near the ring (+). Intermediate positions were taken into account with a smaller prefactor reflecting the reduced coupling to the SQUID. The cross-shaped arrangement of the measurement positions makes the measurement insensitive to linear variations of the sensor background, which in some cases are larger and more irregular than the final signal. Furthermore, it helps to asses the reliability of the final result, which can be attributed to the ring if its features (typically characterized by higher harmonics of the sensor response) show a spatial dependence similar to that of the ring–pickup-loop coupling. In some areas of the sample, we obtained very irregularly shaped response curves with features of $\sim 1\ \mu\Phi_0$, which did not correlate with the ring position and were discarded.

The response of our rings is dominated by a paramagnetic linear component of up to about 150 $\mu\Phi_0$ at an applied field of 45 G, whose temperature dependence is shown in Fig. 5.1(c). The linear response of heatsunk ring shows approximately a $1/T$ dependence, as do the heat sinks (not shown). Thus, it is most likely due to spins. Evidence for a relatively slow relaxation time [21] and the absence of a low T saturation of the susceptibility due to the Kondo-effect suggest that those spins

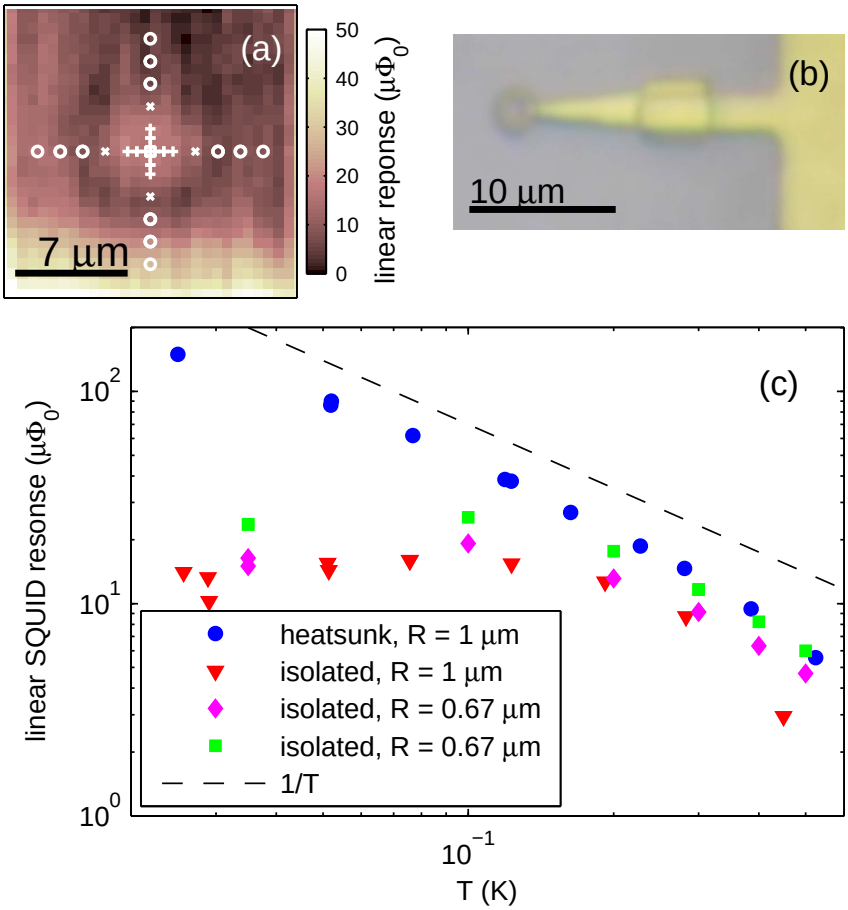

Figure 5.1: (a) Susceptibility scan of an isolated ring used to locate the ring and to define the indicated measurement positions. Background measurements at positions "o" are subtracted from the data taken at positions "+" to obtain the ring response. (b) Optical micrograph of a heatsunk ring with $R = 1$ μm. (c) Temperature dependence of the linear response of one heatsunk and three isolated rings. The data in (a) and (c) reflect the total amplitude of the linear response to a sinusoidal excitation of ± 45 G for (a) and the 0.67 μm rings in (c), and ± 35 G for the 1 μm rings.

are not strongly (exchange) coupled to the conduction electrons. Together with their large concentration (≈50 ppm assuming spin 1/2) estimated from the susceptibility $\chi = \mu_0 n(g\mu_B)^2 J(J+1)/3k_B T$, this indicates that they are likely different from the magnetic impurities that often cause excess dephasing [109, 16]. The linear response of isolated rings flattens out below about 150 mK. This indicates a saturation of the electron temperature at about 150 mK, in good agreement with estimates of the heating effect of the 10 μA, 10 GHz Josephson current in the SQUID pickup loop (see section 5.4.3). While it is not a priori clear whether the spins are coupled more strongly to the electrons or phonons, the different behavior of heatsunk and isolated rings indicates that the linear susceptibility does reflect the electron temperature. In the following, we will focus on the much smaller nonlinear response, obtained after eliminating the linear response (including its out of phase component) by subtracting a fitted ellipse. We note that the linear component varies by up to a factor of 2 between nominally identical rings.

Fig. 5.2 (a) shows data from fifteen isolated rings with $R = 0.67$ μm. A prominent feature is a step-like shape near $\Phi_a = 0$. This feature, which we believe to be due to nonequilibrium effects in the spin response, appeared in nearly all measured rings, and was most pronounced in heatsunk rings [5.2 (c)]. However, there is also an oscillatory component. Motivated by the idea that the spin signal could be the same for all rings, whereas persistent currents are expected to fluctuate around a near zero mean, we have computed the average of all fifteen datasets and subtracted it from each individual curve. The results shown in Fig 5.2(b) show a clear oscillatory response for the majority of the rings. In most cases, it can be fitted with a sine curve of the expected period. However, the lowest two datasets in the left column give much better fits with a 30 % larger period, which would correspond to an effective radius close to the ring's inner radius. The apparent presense of a signal with a much larger period in two datasets appears to be due to a different magnitude of the zero-field anomaly in these rings.

From the sine curve fits to 13 datasets, we obtain an estimate for $M\langle I_{h/e}^2\rangle^{1/2}$ of 0.11 $\mu\Phi_0$ if fixing the period at the value expected for the mean radius of the rings, or 0.12 $\mu\Phi_0$ if treating the period as a free parameter. This is in good agreement

with the theoretical value of 0.1 $\mu\Phi_0$ from Eq. 5.3 for $T = 150$ mK. We checked that the response of four of these rings was reproducible over a timescale of several weeks without warming up the sample.

An alternative way to largely eliminate the step-like feature is to subtract fits to a phenomenological model consisting of two Fermi functions whose center is offset from zero to account for the hysteresis. This procedure gives somewhat different results, but does not change the overall picture when applied to the data in Fig. 5.2(a).

Out of five measurements of rings with $R = 0.57$ μm, four gave similar results after subtracting their mean response as the $R = 0.67$ μm rings. The rms value of the fitted sine amplitudes was 0.06 and 0.07 $\mu\Phi_0$ for variable and fixed period, respectively. A fifth ring was excluded from this analysis because it had a significantly larger zero field anomaly. Data from additional three rings were rejected because of a large variation of the sensor background that was not connected with the rings.

We have also measured eight isolated rings with $R = 1$ μm. The magnitude of the zero-field anomaly seen in these rings varies significantly, so that the mean subtraction procedure cannot fully remove it. One of these rings shows a sinusoidal signal with a period of 1 to 1.15 ϕ_0 and an amplitude of up to 0.1 $\mu\Phi_0$, however with a poor reproducibility. The other seven rings do not show any clear oscillations, either in the raw data or after subtracting the fitted model or the mean of some or all of those datasets. Blind sine curve fits give $M\langle I_{h/e}^2\rangle^{1/2} = 0.03$ $\mu\Phi_0$. Most important, none of those rings show a signal at a period similar to those in Fig. 5.2, which establishes the ring size dependence and thus supports the interpretation as persistent current.

Subtracting fitted steps from the data from four heatsunk rings results in some aperiodic residuals mostly near zero field, with an amplitude of less than 0.2 $\mu\Phi_0$. In those rings, the step-feature was more pronounced than in any others, and varied significantly from ring to ring. Data from a representative ring are shown in Fig. 5.2(c),(d). Since the electronic wave functions extend coherently into the heat sinks, which capture a significant amount of flux, it is not clear to what extent one may expect a periodic response from our heatsunk rings. Thus, both a persistent-current like orbital response and an imperfect elimination of the step feature may contribute to the aperiodic residual signal.

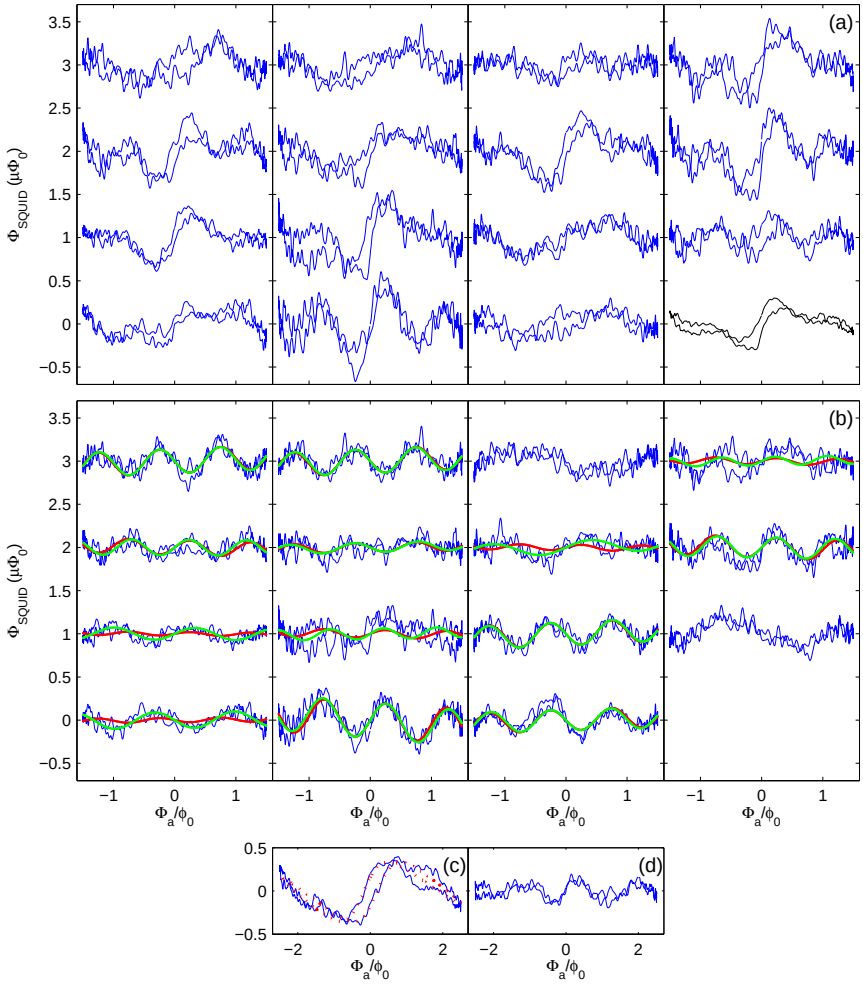

Figure 5.2: (a) Response of 15 nominally identical rings with R= 0.67 μm after subtracting the in- and out-of-phase component of the linear response. The lower right (black) curve is the mean of all other datasets. (b) Results of subtracting the mean from the other datasets in (a). The smooth lines are sinusoidal fits (including a linear background term) with fixed (red) and fitted period (green). The datasets for which no fits are shown were excluded from the analysis because they appear to be strongly affected by a residual of the zero field anomaly. The rms amplitude estimated from the fits is 0.11 and 0.12 $\mu\Phi_0$, respectively, compatible with the expected value of $\langle I^2_{h/e}\rangle^{1/2}$. (c) Data from a representative heatsunk ring after subtracting the in- and out-of-phase component of the linear response. (d) Result of subtracting a fitted phenomenological model for the step-like feature of the form $a_1 \tanh(a_2\Phi_a - a_3 \mathrm{sgn}(d\Phi_a/dt))$ + ellipse (dotted line in (c)) from the data in (c).

We have measured the temperature dependence of the responses of two 0.67 μm rings with large oscillatory signals of opposite sign. Their linear components are included in Fig. 5.1(c). Taking the difference between their nonlinear responses at each temperature, which would also eliminate a common background signal, leads to predominantly sinusoidal curves at most temperatures, as shown in Fig. 5.3(a). The period appears to be T-independent, and amplitudes from fits with a fixed period are consistent with an $e^{-k_B T/E_c}$ dependence with $E_c/k_B = 340$ mK, as obtained from the measured D [Fig. 5.3 (b)]. While those amplitudes appear to increase down to the lowest T, a saturation below 150 mK as indicated by the horizontal dashed line is compatible within the estimated errors, which are mostly due to an imperfect sensor background rejection. Reducing the field sweep range from 45 to 35 and 25 G or varying the frequency between 13 and 333 Hz (at base temperature) changed the size of the step feature, but the oscillatory component in the difference between the responses of those two rings remained more or less unchanged (see section 5.4.1).

Given the variations in the fitted period, one may ask whether persistent currents in rings with a finite line width could exhibit fluctuations in the period. A simple model based on estimating the variation of the area enclosed by diffusive semi-classical paths indicates that periods corresponding to effective radii between the inner and the outer radius are indeed quite plausible. A similar effect was observed in a previous measurement on an ensemble of 30 rings [67], where the oscillation amplitude decreased beyond a few periods from zero applied field. Thus, the deviations from the period corresponding to the mean radius, which may also partly be due to an imperfect background elimination, are consistent with the interpretation of our data as persistent currents.

In conclusion, we have measured the magnetic response of 33 mesoscopic Au rings, one by one. After phenomenologically eliminating a step-like component in the nonlinear response, some of the rings also display an oscillatory component, whose period, typical amplitude and temperature dependence are fully consistent with the predicted behavior of the typical h/e periodic persistent current, $\langle I_{h/e}^2 \rangle^{1/2}$. The interpretation of this periodic component as persistent currents is supported by its independence on temperature and field sweep range, and its geometry dependence: larger rings had

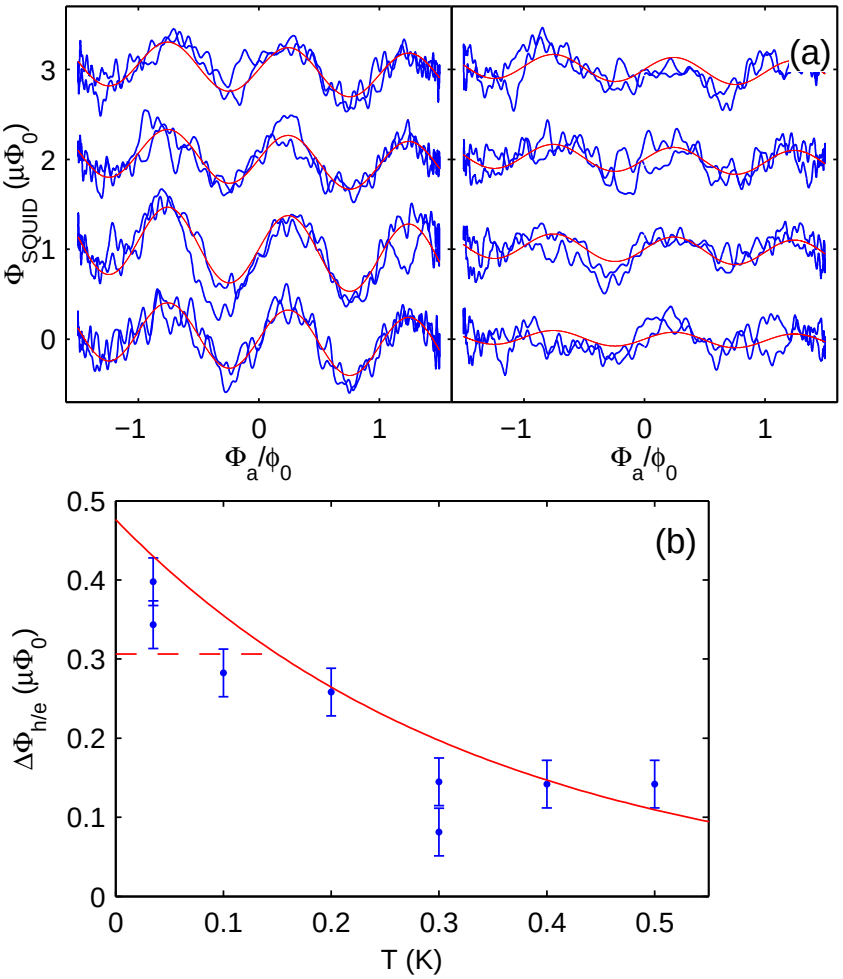

Figure 5.3: (a) Difference between the nonlinear responses of two rings with a large oscillatory component (top first column and bottom second column in Fig. 5.2) at T = 0.035 K, 0.035 K, 0.1 K, 0.2 K, 0.3 K, 0.3 K, 0.4 K and 0.5 K, from lower left to upper right. (b) Temperature dependence of the amplitude of the sinusoidal fits in panel (a). The exponential curve is a fit to $e^{-\min(T,0.15K)/0.34K}$, taking the the saturation of the electron temperature into account. The error bars reflect the rms difference between the results of a separate analysis of the x and y scan across the ring [cf. Fig. 5.1(a)].

either no distinguishable periodic response, which can be attributed to their smaller E_c, or a periodic response within the expected period range.

This work was supported by NSF Grants No. DMR-0507931, DMR-0216470, ECS-0210877 and PHY-0425897 and by the Packard Foundation. Work was performed in part at the Stanford Nanofabrication Facility, which is supported by NSF Grant No. ECS-9731293, its lab members, and industrial affiliates.

5.4 More data and further considerations

5.4.1 Consistency checks

The most important evidence that the oscillatory signal found in the $R = 0.67$ μm rings does indeed reflect persistent currents is the absence of a similar signal in $R = 1$ μm rings. Data from both kinds of rings is shown in Fig. 5.4, before and after eliminating the zero field anomaly. The larger rings are expected to have a slightly larger electron temperature because they are coupled more strongly to the SQUID, and have a smaller E_c of 150 mK. This reduces the expected value of $M\langle I_{h/e}^2\rangle^{1/2}$ to about 0.05 $\mu\Phi_0$. Even though the 1 μm rings do not show clear oscillations, we have fitted the data with the step subtracted with sine curves in order to estimate the amplitude of an oscillatory response that would be consistent with the data. Fits with the period variable and fixed at the expected value of 14 G give $M\langle I_{h/e}^2\rangle^{1/2} =$ 0.03 $\mu\Phi_0$ and 0.024 $\mu\Phi_0$, respectively.

Fig. 5.5 shows additional data from $R = 0.57$ μm rings, which give a similar picture as the $R = 0.67$ μm rings shown in Fig. 5.2. Fitting sine curves to the data in Fig. 5.5(b) gives typical amplitudes of 0.07 and 0.06 $\mu\Phi_0$ for variable and fixed period, respectively. The difference from the theoretical value of 0.12 $\mu\Phi_0$ is not statistically significant.

As a consistency check, we have repeated the measurements of the two $R =$ 0.67 μm rings with the largest oscillatory signal at different field sweep frequencies and amplitudes. The data in Fig. 5.6(a),(b) show that the response of each ring changes significantly as a function of frequency. The difference between the two

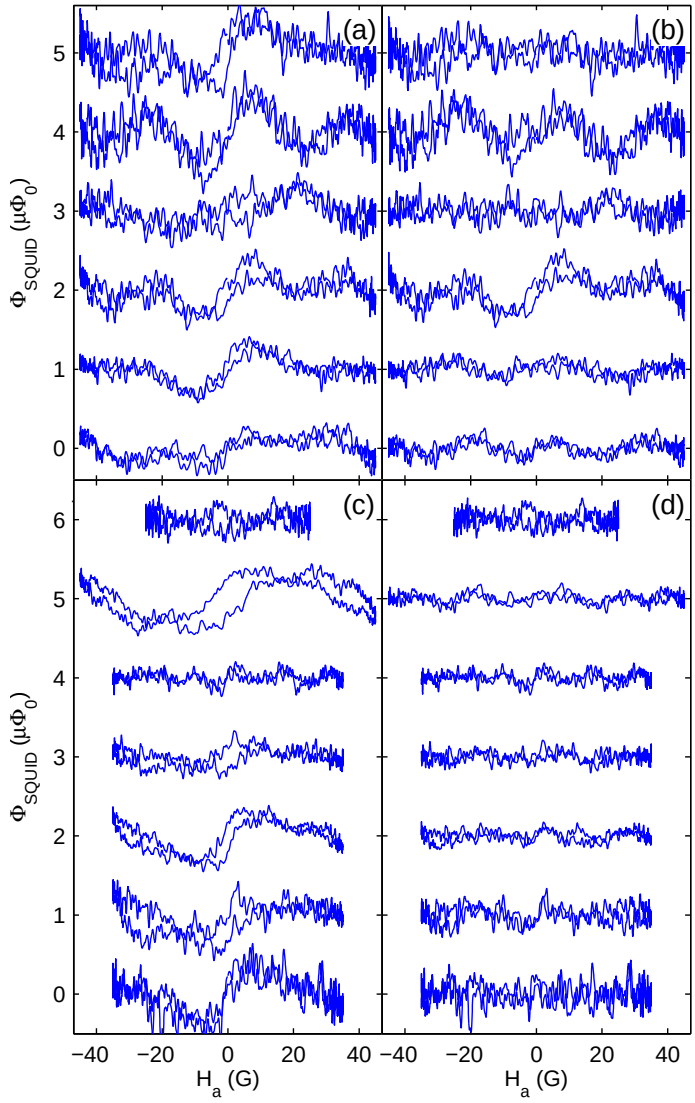

Figure 5.4: Comparison of data from rings with $R = 0.67$ μm [(a), (b), first six rings from Fig. 5.2] and $R = 1$ μm [(c), (d)]. The top three datasets in (c) and (d) are from the same rings, but were taken at different field ranges. The left panels [(a), (c)] show data from which only the linear component (in- and out-of-phase) has been subtracted. The right panels [(b), (d)] show the same data after subtracting the phenomenological step model (see caption of Fig. 5.2). None of the 1 μm rings shows oscillations comparable to those seen in the 0.67 μm rings.

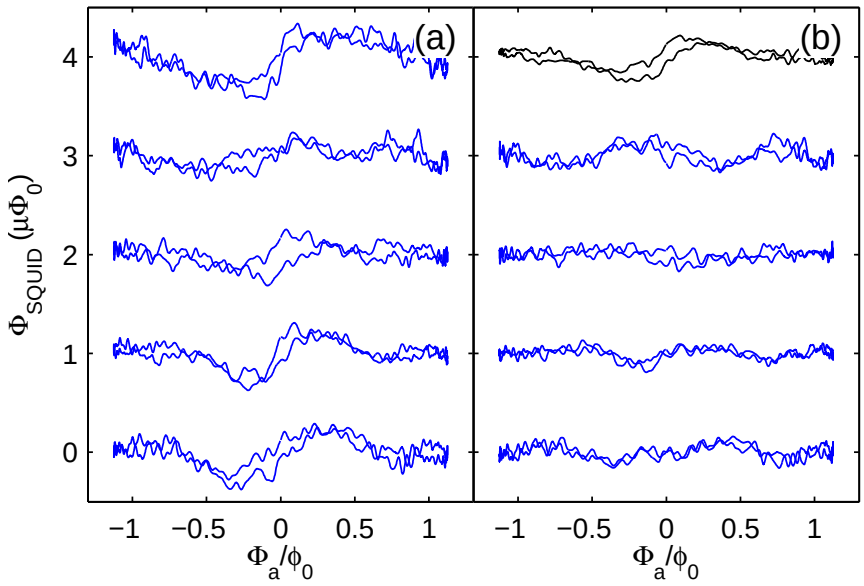

Figure 5.5: (a) Nonlinear response of five $R = 0.57$ μm rings. (b) Mean of the lower four curves shown in (a) (top, black curve) and results of subtracting this mean from each of those curves. The topmost dataset from (a) was excluded because it shows a significantly larger zero field anomaly.

responses at the same frequencies on the other hand only show minor variations [Fig. 5.6(c)]. Computing this difference eliminates any background signal that is the same in both rings. The zero field anomaly is smaller at lower frequency, consistent with the hypothesis that it is a nonequilibrium effect in the spin-response, for which millisecond relaxation times are quite plausible at the low measurement temperatures [76]. The orbital response on the other hand is expected to be governed by the nanosecond-scale electronic relaxation times, and should thus be frequency independent at the much lower measurement frequency. The consistency of the data with those expectations supports the interpretation that the oscillatory component is not related to the zero field anomaly. There may also be a slight amplitude dependence of the step feature, however it is much less pronounced than the frequency dependence, so that we only show the difference data in Fig. 5.6(d). It is consistent with the response at any given field being independent of the field sweep amplitude.

5.4.2 Discussion of the zero-field anomaly

The origin of the step-like feature in the nonlinear response is currently not well understood. It appears that the most likely explanation is a nonequilibrium effect of the spin response. Experimentally, the non nonequilibrium nature of the zero field anomaly is supported by the splitting between the up and down sweep, seen for example in Fig. 5.2(a),(c), and the frequency dependence discussed in section 5.4.1. While there is no direct evidence for the step-feature being caused by spins, it seems natural to suspect a connection to the observed spin-like susceptibility. The latter had a measurable out-of-phase component [21], which suggests that the linear response is affected by nonequilibrium effects as well.

Theoretically, spins may provide an explanation along the following lines: Assuming a finite matrix element for tunneling between spin-up and spin-down states, there will be an avoided crossing at zero field. Depending on whether the Zeeman splitting is larger or smaller than the zero-field level splitting, the mechanism leading to a paramagnetic susceptibility is either the relaxation of the up and down population numbers towards a thermal equilibrium distribution, or a change of the magnetic

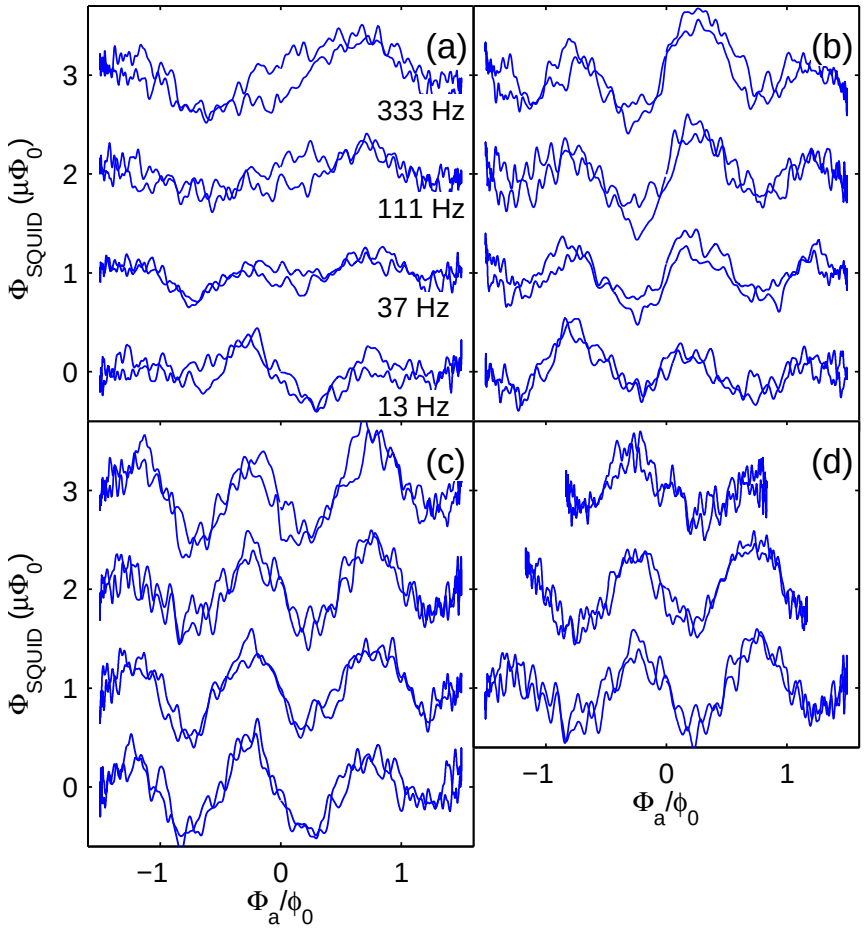

Figure 5.6: (a), (b) Data from the two $R = 0.67$ μm rings with the strongest oscillatory signal at field sweep frequencies 13, 37, 111 and 333 Hz (bottom to top). (c) Difference between data in (a) and (b). While the raw data changes noticeably, the difference remains nearly constant. (d) Difference between the responses of the same two rings at field sweep amplitudes 45, 35 and 25 G, taken at 111 Hz. Note that the fitted linear component that was subtracted is not the same for all datasets and leaves a significant slope for the topmost dataset.

moment of each state with nearly constant occupation numbers. The relaxation of spins at low temperature can be slower than our sub-kHz experimental frequencies [76], whereas the adiabaticity condition for a level splitting corresponding to, say, 10 G is compatible with MHz-scale frequencies. Hence, it is plausible that the response is faster near zero field, and thus leads to a slight enhancement of the paramagnetic differential susceptibility at small fields.

However, one may wonder if an orbital response might also contribute to the zero field anomaly. Such an effect could be closely related to persistent currents, just as weak localization effects in wires are related to Aaronov-Bohm oscillations in the conductance of mesoscopic rings. While a ring geometry leads to an oscillatory response with a well defined period, the superposition of contributions with a wide range of periods from a geometry without a characteristic area would lead to a total response that is most pronounced near zero field. The mostly consistent sign of the zero-field anomaly would imply that one would have to look for an effect with a finite ensemble average, such as the $h/2e$ component of persistent currents.

Since both weak localization corrections to the conductance of wires and ensemble averages of persistent currents depend on the Cooperon, it seems reasonable to estimate the field range over which an orbital response would decay by comparison with the magnetoresistance due to weak localization. The resistance change of a one dimensional wire (in the absence of spin-orbit coupling) as a function of magnetic field is proportional to $(1+(2\pi L_\phi wB/\sqrt{3}\phi_0)^2)^{-1/2}$. Thus, its characteristic field scale corresponds to about 0.3 ϕ_0 captured in a wire section of length L_ϕ. Replacing L_ϕ with the circumference $L = 4.3$ μm, this corresponds to a field of about 10 G, which is about twice as large as the half-width of the zero field anomaly. However, one should keep in mind that the Cooperon may enter the expressions for the weak localization effect and the orbital response in different ways, which may add additional factors of order unity.

The relatively large amplitude of the zero-field anomaly, which is comparable to the (expected and measured) persistent current signal, seems difficult to explain theoretically in terms of an orbital response. However, given the large $h/2e$ response seen in previous ensemble measurements (see section 5.2), the current theoretical

understanding might be incomplete.

Most important, the emergence of hysteresis and a frequency dependence at sub-kHz frequency seem rather unlikely for any orbital mechanism, which should be governed by the much faster electronic relaxation times. Nevertheless, it is possible that a nonequilibrium spin response masks a comparable or smaller orbital contribution.

5.4.3 Effect of Josephson oscillations in the SQUID

A particular concern in our experiment is the effect of the microwave frequency flux coupled into the sample rings from an ac current in the SQUID pickup loop. This oscillating current is generated by Josephson oscillations in the SQUID junctions. For a typical SQUID bias voltage of 20 μV, it would have a frequency of $\omega/2\pi = 10\ \mu\mathrm{V}/\Phi_0$ = 10 GHz, and its amplitude should be on the order of the critical current, i.e. 10 μA. This corresponds to a flux Φ_{ac} of a few mΦ_0 in a typical sample ring. A simple estimate of the power P dissipated in the ring as $P = (\omega\Phi_{ac})^2/2R_{ring}$, where $R_{ring} \sim 1\ \Omega$ is the resistance of the ring, leads to $P \sim 10^{-14}$ W, which would heat the electrons in the ring to 100 - 200 mK if the cooling is assumed to be limited by electron-phonon coupling, for which one expects $T = (P/wdL\Sigma)^{1/5}$, with $\Sigma \approx 10^9$ W/(m^{3}K^5).

An interesting question is whether this estimate of P is adequate for a ring smaller then the dephasing length L_ϕ. It is lacking the instantaneous dephasing that would occur in a wire connecting two reservoirs as soon as an electron diffuses into a reservoir. For the wire, the total dissipated power thus only depends on the elastic scattering in the wire, but not the details of the dephasing and inelastic relaxation processes. In an isolated ring on the other hand, relaxation processes are confined to the ring itself and play a crucial role in determining the amount of dissipation. This has been shown explicitly by Trivedi and Browne [134] for a one-dimensional ring (M = 1). Starting from a phenomenological relaxation of the density matrix to its flux dependent equilibrium value, they show that the dissipative response of the ring is proportional to the relaxation rate. It is clear that in the absence of any relaxation and for the flux changing slowly on the scale of the typical level spacing, one simply encounters Bloch oscillations in the bands formed by the flux dependent energy levels,

and there will be no dissipation. For faster changes in the flux, one has to take into account Landau-Zener transitions between those bands, and how reversible they are. I am not aware of any treatment of this problem for a many-channel diffusive ring. Experimentally, the saturation of the spin-response from our rings below about 150 mK discussed in section 5.3 is consistent with the above heating estimate.

One may also ask whether the high frequency flux can lead to nonequilibrium effects that cannot be accounted for with an elevated electron temperature. For example, Kravtsov and Altsuler [80] predicted a direct relation between a contribution to $\langle I_2 \rangle$ by nonequilibrium noise, and the excess dephasing caused by the same noise in long wires. They find that $\langle I_2 \rangle = C(e/\tau_\phi)e^{-L/2L_\phi}$ with $|C| \approx 1$, and propose that this might provide a common explanation for both the large persistent currents seen in experiments (see section 5.2) and the excess dephasing observed in weak localization measurements [98]. In the meantime, the latter has been shown to be due to small concentrations of magnetic impurities [109, 16]. However, we can use this result to estimate the effect of the Josephson oscillations on the ring. Altshuler, Aronov and Spivak ([1], see also [143]) have shown that an ac electric field E at frequency $\omega/2\pi$ can lead to a dephasing-like effect which is characterized by a phase breaking rate $\tau_{MW}^{-1} \approx \alpha\omega$ for $\alpha \equiv 2e^2DE^2/\hbar^2\omega^3 \ll 1$. For typical ring and SQUID parameters, this leads to $\tau_{MW} \sim 1$ μs, corresponding to a sub-pA persistent current. This estimate suggests that at least this particular effect is not significant for our experiment.

Chapter 6

Scanning Hall probe imaging of $ErNi_2B_2C$

Hendrik Bluhm, Suchitra E. Sebastian, Janice W. Guikema, I. R. Fisher, Kathryn A. Moler,
Phys. Rev. B, **73**, 014514 (2006).

Abstract

We report scanning Hall probe imaging of $ErNi_2B_2C$ in the superconducting, antiferromagnetic, and weakly ferromagnetic regimes in magnetic fields up to 20 Oe, well below H_{c1}, with two results. First, imaging isolated vortices shows that they spontaneously rearrange on cooling through the antiferromagnetic transition temperature $T_N = 6$ K to pin on twin boundaries, forming a striped pattern. Second, a weak, random magnetic signal appears in the ferromagnetic phase below $T_{WFM} = 2.3$ K, and no spontaneous vortex lattice is present down to 1.9 K. We conclude that ferromagnetism coexists with superconductivity either by forming small ferromagnetic domains or with oscillatory variation of the magnetization on sub-penetration depth length scales.

6.1 Introduction

Magnetic order and superconductivity were once thought of as incompatible phenomena. The Meissner state excludes a magnetic field from the bulk, and superconductivity is destroyed by sufficiently high fields. However, two forms of coexistence are theoretically possible. First, if the orientation of local moments varies on a length scale shorter than the penetration depth, λ, the resulting internal field is not screened by the Meissner response, which is only effective over length scales of order of λ or larger [57, 20]. This form of coexistence is found in $ErRh_4B_4$ and $HoMo_6S_8$. [99, 86] The second possible form of coexistence is a so-called spontaneous vortex lattice which carries the field generated by the magnetization [104, 57, 81]. Such a spontaneous vortex lattice has never been observed in a zero-field-cooled sample, but $ErNi_2B_2C$ was suggested as a strong candidate [104]. Evidence for the existence of a vortex lattice in $ErNi_2B_2C$ after magnetic cycling has been reported [70] based on Small-Angle Neutron Scattering (SANS). The form of the coexistence in the zero-field-cooled state remains unclear.

In this work, we present local scanning Hall probe measurements of $ErNi_2B_2C$ at low fields with single-vortex resolution. Our results show clearly that no spontaneous vortex lattice forms after cooling in zero field. Instead, we observe a weak, random magnetic field, indicating that the magnetization is inhomogeneous on a sub-micron length scale. In addition, we show that vortices tend to locate along twin boundaries in the antiferromagnetic state. Earlier and recent work [118, 135] using Bitter decoration demonstrated the tendency of vortices to locate along twin boundaries below T_N. With our technique we were able to examine the behavior of individual vortices in the three different phases of $ErNi_2B_2C$ and at the phase transitions.

$ErNi_2B_2C$ is a member of the quaternary rare earth compounds RNi_2B_2C (R=rare earth), which show a variety of both magnetically ordered and superconducting states. Since their discovery one decade ago [125, 49, 28], this family of materials has been under extensive study using a wide range of experimental techniques. $ErNi_2B_2C$ has a superconducting onset T_c of ≈ 11 K, becomes antiferromagnetic below $T_N \sim 6$ K, [35] and exhibits weak ferromagnetism below $T_{WFM} \approx 2.3$ K [27]. The magnetic

phases at $T < 6$ K are orthorhombic due to strong magnetostriction [42], and the magnetism significantly enhances flux pinning [53, 43, 66]. Neutron scattering experiments [71, 36] show that in $ErNi_2B_2C$, the antiferromagnetism in the temperature range $T_{WFM} < T < T_N$ occurs with an incommensurate wave vector of 0.553 a^* (where $a^* = 2\pi/a$) along the a-axis with moments pointing in the $\pm b$ direction. At T_{WFM}, a lockin transition to a commensurate wave vector of 0.55 a^* takes place, suggesting that every 20th moment is left at a node of the staggered field and thus free to order ferromagnetically [71, 36]. The resulting average ferromagnetic component of $0.39\mu_B$/Er is relatively weak and the self-field of $4\pi M = 700$ G is comparable to the lower critical field $H_{c1} \approx 500$ Oe estimated from magnetization measurements in Fig. 6.1 and Ref. [35]. The similarity of the self-field and H_{c1}, together with the persistence of superconductivity down to the lowest temperature explored so far, is the reason for suspecting a spontaneous vortex lattice. [104]

Possible scenarios for the interplay between superconductivity and ferromagnetism have been analyzed in Refs. [57, 20, 104, 81] based on the Ginsburg-Landau free energies of a superconductor and a ferromagnet with magnetization $\vec{M}$ occupying the same space and coupled by a purely magnetic interaction term $1/4\pi \int \vec{B} \cdot \vec{M}$. Terms corresponding to pair breaking effects were considered less important since the magnetic moments are due to the partially filled $4f$ shells of the Er, which are not part of the conduction band. Ref. [20] shows that supercurrents would screen out any magnetic field on length scales larger than the London penetration depth λ, so a phase transition leading to a homogeneous magnetization would be suppressed due to the screening of the magnetic coupling between the magnetic moments. Two different kinds of coexisting phases could emerge, depending on the coefficients of the model (particularly the magnetic coherence length ξ_M). First, if magnetic gradients are energetically cheap so that $\xi_M \ll \lambda$, $\vec{M}$ will oscillate with a wave vector of order $(\lambda\xi_M)^{-1/2}$. In an isotropic magnet this will always happen with a circular polarization so that $|\vec{M}|$ is constant and only gradient energy needs to be afforded. This spiral state has been reported in $ErRh_4B_4$ [99] and $HoMo_6S_8$ [86]. In the case of $ErNi_2B_2C$, however, a strong crystal electric field aligns the magnetic moments along the b-axis, [71, 36] so that the ordering is theoretically more likely to happen in a

linearly polarized wave. [57] Second, if such a variation in $\vec{M}$ would be too costly and $4\pi M > H_{c1}$, a spontaneous vortex lattice may form, leading to a spatially varying $\vec{B}$ of uniform direction which can support a similar $\vec{M}$. [104, 57] SANS experiments reported on cond-mat in 2001 [70] give evidence for such a vortex lattice in $ErNi_2B_2C$ after cycling to high fields. The vortex lattice peaks are absent after cooling in zero field, leaving open the question of the nature of the zero-field-cooled state.

6.2 Sample preparation and methods

We have grown single crystals of $ErNi_2B_2C$ using a flux growth technique with Ni_2B as the flux [35]. Measurements were made on plates of typical size 3 x 3 x 0.5 mm^3, where the crystallographic c-axis is perpendicular to the plate surface. We measured magnetization and resistance using a Quantum Design SQUID magnetometer to confirm values of T_N, T_c and T_{WFM} obtained in previous work. [35, 27, 71, 36] The value of the superconducting transition temperature T_c is obtained from zero-field resistivity and low-field (H = 25 Oe) magnetization measurements. From Fig. 6.1, zero resistance and the sharp increase in diamagnetism which have previously been used to identify T_c[35] appear at 10 K. The magnetization as a function of field at 1.8 K [Fig. 6.1(d)] indicates that $H_{c1,ab}$ is lower than 500 Oe. An extrapolation of the virgin curve magnetization data as indicated by the dashed line and the remnant magnetization give evidence for a ferromagnetically ordered moment of about 0.4 μ_B/Er, consistent with Ref. [71]. The temperature at which this weak ferromagnetic order sets in is inferred to be T_{WFM} = 2.2 K from the sharp break in the slope of magnetization as a function of temperature in an applied field of 1 kOe [Fig. 6.1(c)], indicating a phase transition at this temperature. The bump between 5 and 6 K in this figure can be attributed to the antiferromagnetic ordering at T_N, consistent with earlier work [35, 27, 71, 36].

To measure the local magnetic field component perpendicular to the sample surface, we used a scanning Hall probe microscope (SHPM) in a ^{4}He flow cryostat [58]. A 0.5 μm wide Hall probe defined using e-beam lithography on a 140 nm deep

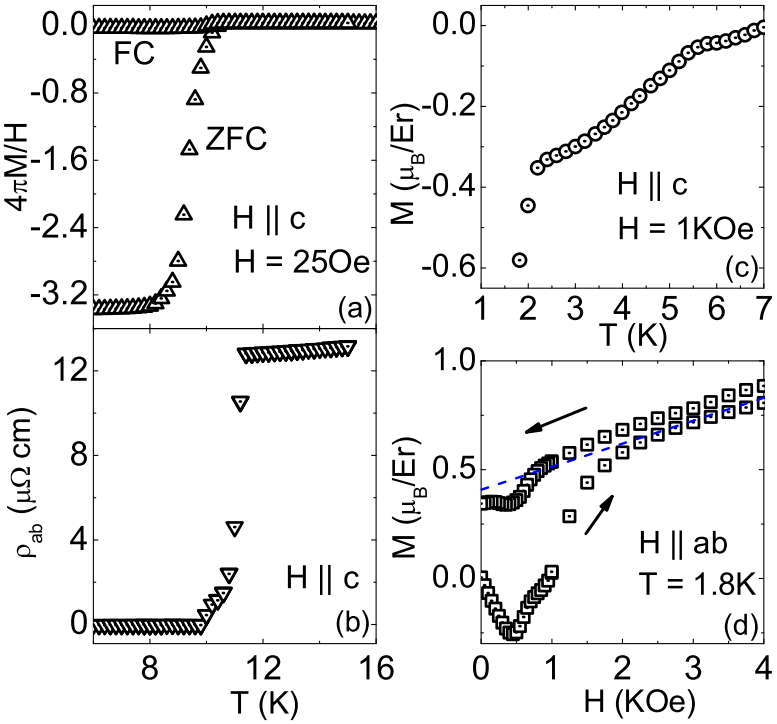

Figure 6.1: (Color online) Sample characterization: (a) Volume magnetization as a function of temperature in a magnetic field of 25 Oe applied parallel to the c-axis. Both the zero-field-cooled (ZFC) and field-cooled (FC) data were taken on warming. (b) Zero field electrical resistivity in the ab-plane ρ_{ab} as a function of temperature. (c) Temperature dependence of the magnetization in an applied field of 1 kOe applied parallel to the c-axis, measured on warming following initial zero-field-cooling. (d) Magnetization as a function of applied field perpendicular to the c-axis at $T = 1.8$ K for increasing and decreasing field after zero-field-cooling.

GaAs/AlGaAs heterostructure is scanned over the sample surface using a piezoelectric scanner. For some images requiring a good field resolution, we have averaged over several tens of scans and removed switching noise from the Hall probe from the raw data. The field sensitive area of the probe is located near a corner of the substrate so that an angle of a few degrees between the probe substrate and the sample lead to a probe-sample distance between 0.5 and 1 μm when the substrate corner touches the sample. Field components varying with a wave vector k in the xy-plane are theoretically known to be attenuated as e^{-kz} at a height z above the sample [116]. The measured Hall voltage is proportional to the magnetic field averaged over the active area of the probe. Thus, both the probe's size and its height above the sample effect the spatial resolution.

This technique offers higher spatial resolution than magneto-optical measurements, is significantly faster and less dependent on surface quality than scanning tunneling spectroscopy, and allows many scans under different parameters in one cooldown. The information is easier to interpret than force gradients obtained from magnetic force microscopy (MFM).

Magnetic scans of the ab-face were taken on a sufficiently large and smooth natural crystal face. Due to the crystal growth process, an area suitable for scanning was not available on a natural (010) plane. Thus we cut and polished the crystal along the ac (bc) face in order to scan there.

6.3 Experimental results

We first discuss the data taken on the ab face. Upon cooling the sample below T_c in a weak applied field, H_a, normal to the sample surface, vortices appear in a random configuration [Fig. 6.2(a)]. The vortex distribution is inhomogeneous, with a vortex density of H_a/Φ_0 (where $\Phi_0 = h/2e$) within a factor of two, as expected for a type II superconductor with pinning sites. Because of the large vortex spacing at $H_a \ll H_{c1}$, the repulsive interactions between the vortices are too weak to order the vortices into a lattice. Individual vortices occasionally move during scans. The apparent shape of the vortices, which depends mostly on the probe-sample separation, can be fitted

well with a monopole model [106] for the vortex field in vacuum. The resulting flux per vortex is $0.9 \pm 0.2\ \Phi_0$ with the systematic uncertainty lying mostly in the spatial calibration of our microscope.

As the temperature is lowered below T_N, the vortices spontaneously line up along stripes with a typical separation between stripes of 3 to 8 μm [Fig. 6.2(b)]. Between different cycles through T_N, their position varies and the orientation changes between the [110] or [$\bar{1}$10] [Fig. 6.2(c)] direction. As the largest stress due to the change in lattice parameters is likely to occur when only part of the sample has gone through the AFM transition, the exact configuration of the stripes can be expected to depend on such factors as temperature gradients and cooling rate during the transition. Further lowering the temperature below T_{WFM} has no effect on the vortices down to 1.9 K, the lowest temperature measured. As the temperature is raised above T_N, they move back into a nearly static disordered configuration [Fig. 6.2(d),(e)]. This relaxation happens gradually over the course of several scans at 6 K. The remnants of the vortex alignment in Fig. 6.2(e) disappeared a few scans later without changing the temperature.

At temperatures above approximately 5 K, the vortices are still mobile enough to occasionally hop between different sites, both along and between twin boundaries, under the influence of the probe during scans. On the other hand, we observed no motion between two scans taken at 4 K, although the temperature was raised to 5.3 K for several hours in between. Thus, there is no evidence for thermally activated vortex motion. The depinning mechanism could be interaction with the field on the order of 0.5 Oe at the sample surface generated by the 10 μA rms AC bias of the Hall probe or mechanical or thermal effects due to local heating of the sample by the probe. Indeed, the depinning probability at a given T strongly depends on the probe-sample distance.

Below about 5 K, no vortex motion was observed. This is in good qualitative agreement with the depinning data in Refs. [53, 43, 66], where a gradual increase of the pinning strength with decreasing temperature above T_{WFM} and a relatively sharp increase upon cooling below T_{WFM} is reported.

Our crystal growth process only yields natural faces at the (001) and what seems

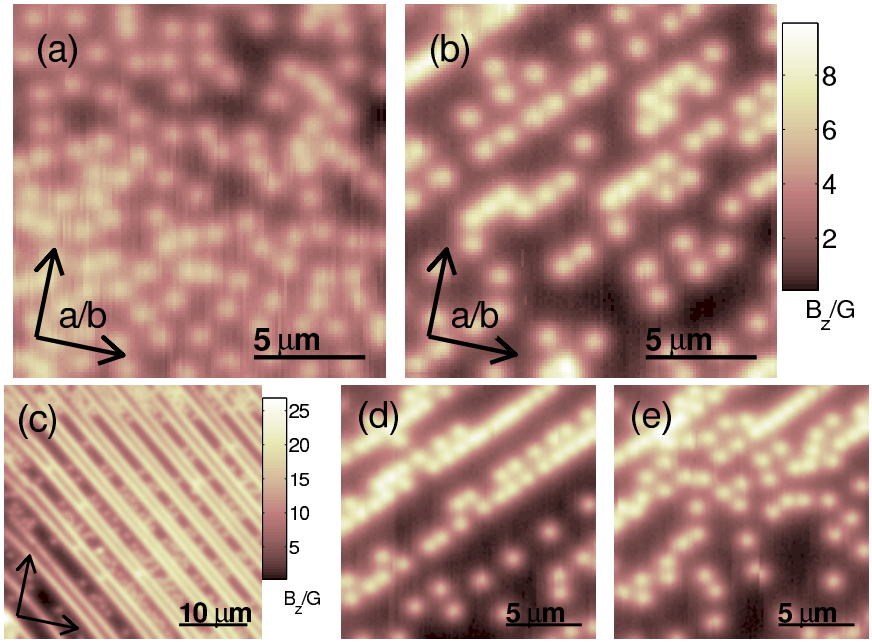

Figure 6.2: (Color online) After cooling below T_c in a weak field [2.4 Oe in (a), (b), (d), (e), 18 Oe in (c)], a vortex distribution consistent with random pinning is observed on the *ab*-face [(a), 7.3 K]. Upon reducing the temperature below T_N, the vortices spontaneously organize along twin domain walls along the [110] [(b), 5.3 K] or [$\bar{1}$10] [(c), 4.2 K] direction. The pattern gradually disappears as the temperature is raised again [(d), 5.7 K, (e), 6.0 K, different cycle than (a) and (b)]. The distance between the domain walls varies between typically 3 to 8 μm and their position and orientation changes after cycling above T_N. No further change is observed when cooling below T_{WFM}.

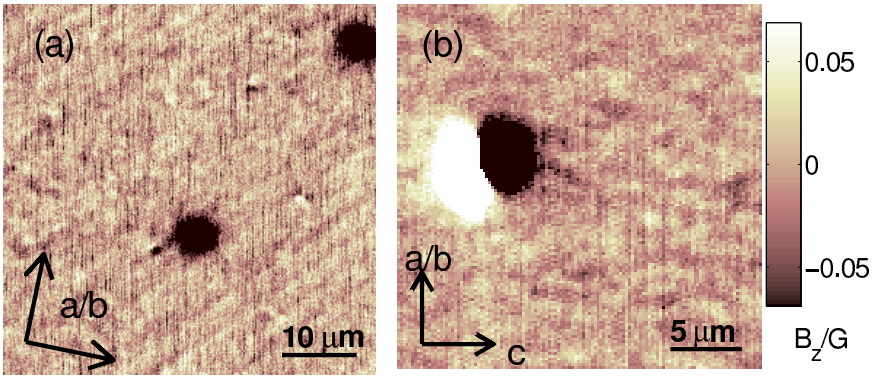

Figure 6.3: Magnetic images of the *ab*-face (a) and *bc*-face (b) at 1.9 K. Below T_{WFM} a weak random field of the order of 20 mG rms amplitude appears after (nominally) zero-field-cooling. The blobs are vortices which saturate the color scale. If the random signal were due to the formation of an (unresolved) vortex lattice below T_{WFM}, one would expect any single vortex to be incorporated in the vortex lattice and disappear. The *ab*-face (a) shows a structure at the same length scale and angle as the vortex lines revealing twin boundaries. Magnetic dipoles as in (b) have been observed only on the polished *bc*-plane. We believe that they are vortex-antivortex pairs pinned on surface imperfections.

to be the (101)[(011)] plane, but with much smaller smooth patches in the latter case which makes imaging difficult. Scans along such a (101) face showed that vortices relocate there too as the temperature is changed, but we found no evidence for pinning in an ordered way, which is not surprising as the twin domains intersect the sample surface approximately at a 45° angle. Similar behavior was found on a cut and polished (100)[(010)] face, however obscured by vortex pinning at specific sites, which we attribute to crystal defects or surface damage probably due to the polishing process.

Upon cooling below T_{WFM}, a very weak magnetic signal with a seemingly random spatial variation of about 20 mG rms amplitude appears between the vortices, both on the *ab* and *ac*(*bc*) face [Fig. 6.3]. However, we observe no change in the vortices on either surface at or below this transition. The scans on the *ab*-plane show stripes in this signal which have the same typical width and angle as the twin domains revealed by vortices. No such striped structure is apparent on the *ac*(*bc*) face.

6.4 Discussion

In the following, we will first discuss the implication of our results for possible pinning mechanisms in the AFM and WFM regime and then proceed to the question of the ground state in the WFM phase.

The observed reorganization of the vortices along lines in the AFM phase was attributed in Refs. [118] and [135] to twin domain walls resulting from the strong magnetostriction in the magnetically ordered regime [42]. It was suggested there that the pinning is due to canting of the magnetic moments at the twin domain walls where the magnetically easy axis and thus the orientation of the moments has to change by 90°. Ref. [118] also reports SHPM measurements at larger fields and without single vortex resolution. They observed an enhanced field near the domain walls, which they interpreted as "convincing evidence for local ferromagnetism at the domain walls". [118] Our data and also more recent Bitter decoration work [135] strongly suggest that this field variation is due to a higher vortex density at the twin boundaries.

The questions arise as to why vortices pin on domain walls, and to what extent canting moments at the domain walls are consistent with our results. We do not find any evidence for magnetic fields emerging from the twin boundaries beyond that of the vortices, so we can set a limit on the local magnetization strength at the twin boundaries. From the data in Fig. 6.3, we conclude that we would be able to detect a variation of B_z of 20 mG at the scan height z_0 above the sample. If the magnetization has a z-component $M_{z,0}$ over a width d along a domain wall and at least a few penetration depths into the sample, but vanishes away from the wall, the resulting far field at $z_0 \gg \lambda$, including the contribution of screening currents, is that of a quadrupole line and will have a maximum value of $8M_{z,0}d\lambda^2/(z_0+\lambda)^3$ [chapter 7]. With $\lambda = 70$ nm[54] and $z_0 = 0.7$ μm, we conclude that $M_{z,0}d < 0.3$ Gμm^2. For a plausible d of 10 nm, this gives upper limits $M_{z,0} < 30$ emu/cm^3 and $B_z = 4\pi M_{z,0} <$ 400 G at the domain wall. The linear flux density of 4 Gμm of such a domain wall would correspond to only one vortex every 5 μm, which is much less than the vortex accumulation seen in Fig. 6.2(c), for example. This upper limit to the flux density suggests that some pair breaking mechanism rather than a purely magnetic

interaction plays an important role in pinning the vortices at twin boundaries.

Similar considerations apply to the much stronger pinning mechanism below T_{WFM} [53, 66]. Strong gradients in $\vec{M}$ could lead to enhanced pair breaking and a reduced condensation energy at domain walls. Alternatively, shielding currents at the domain walls might pull vortices into domains with $\vec{M}$ aligned with the vortex field. However, the latter effect is likely to be weak if $\vec{M}$ varies on a sub-penetration-depth length scale and one would expect a clearly reduced pinning strength for vortices along the c-axis as they would be orthogonal to $\vec{M}$, contrary to observation. [53]

We now turn to the implications of our results regarding the existence of a spontaneous vortex phase. The fact that no vortex relocation is observed when cooling through T_{WFM} clearly indicates that no vortex lattice or other vortex state is formed. If the random signal seen at 1.9 K were due to the formation of vortices, which might in principle happen in a disordered manner without a net magnetization, the previously isolated vortices would interact with the newly formed ones and should be annihilated or screened. Thus we conclude that the magnetization must vanish when averaged over several μm, but has local variations that are not fully screened and appear in our data.

To extract information about the magnetization $\vec{M}$ in the sample from this random signal, the following has to be considered: Due to the separation between the sensor and the sample surface, z_0, components in the spectrum of the image with a large wave number k will be attenuated exponentially by a factor e^{-kz_0} [116]. In addition, averaging occurs due to the finite probe size. This effective absence of large k information makes a deconvolution of the data to obtain the magnetic field at the sample surface impossible. On the other hand, any slow variation of $\vec{M}$ with $k \lesssim 1/\lambda$ will be screened by shielding currents [chapter 7].As $\lambda \approx 70\text{nm} \ll z_0$ [54], only the strongly attenuated small wave vector region of the spectrum of $\vec{M}$ is manifest in our data. This means that there is a wide range of possible scenarios for the behavior of $\vec{M}$ which would be consistent with our data. Yet, there must be some degree of randomness, because the correlation length of the ferromagnetic oscillation must be less than a few μm to explain the random signal we see. We conclude that after cooling in zero field, the ferromagnetism has either a domain like or an oscillatory

structure similar to that found in $ErRh_4B_4$ and $HoMo_6S_8$, where a relatively broad peak in the neutron spectrum is observed [99, 86] at long wave lengths. Neutron scattering [71, 36] and high field susceptometry [27] data on $ErNi_2B_2C$ show that well below T_N, the spins are fixed in direction (up to twinning) and can only change sign. Therefore, this ferromagnetic structure is likely to be squared up, just as the antiferromagnetic spin density wave. If the local magnetization strength is on the order of the bulk remnant magnetization observed after field cycling, the domains must be much smaller than 1 μm to explain the low signal level. A model with the magnetic domains coinciding with the several μm large twin domains (regardless of the strong shielding over such length scales) would lead to an about 3 orders of magnitude larger signal at the domain walls [chapter 7] and thus can be ruled out.

For a more quantitative analysis, we estimated the spectral densities $S_{B_z} = \int d^2\vec{r}\langle B_z(\vec{r})B_z(\vec{r}+\vec{r}')\rangle e^{-i\vec{q}\cdot\vec{r}'}$ of the magnetic scans in Fig. 6.3 by averaging the modulus square of the FFT of segments of the image. The segments were chosen half as big as the image and multiplied with a windowing function. To obtain the spectrum of Fig. 6.3 (a), fits of the vortices were subtracted so that the whole image could be used. For Fig. 6.3(b), fitting attempts lead to large residuals so that we used only segments not strongly affected by the vortex field. The results are shown in Fig. 6.4. To come up with a theoretical model, we assume that the magnetization pattern can be described by a spectral density $S_{M,\alpha\beta}(\vec{q}) = \int d^3\vec{r}'\langle M_\alpha(\vec{r})M_\beta(\vec{r}+\vec{r}')\rangle e^{-i\vec{q}\cdot\vec{r}'}$ with $\alpha, \beta = x, y, z$. According to the arguments of section 6.1, it is reasonable to furthermore assume that the characteristic length scales of the variation of $\vec{M}$ are much shorter than λ and z_0, so that $S_{M,\alpha\beta}(\vec{k})$ will not have a strong $\vec{k}$ dependence for $k \lesssim 1/\lambda$. One can show that under those assumptions and with a predominantly in plane orientation of $\vec{M}$, say along the x-direction, $S_{B_z}(\vec{k}) = 8\pi^2\lambda k_x^2 e^{-2k(z_0+\lambda)} S_{M,xx}(0)$ [chapter 7].

A comparison of this model [Fig. 6.4(c)] and the the spectral density [Fig. 6.4(b)] of the $ac(bc)$-face scan from Fig. 6.3(b) demonstrates a good qualitative agreement. The large fluctuations in the experimental spectrum due to lack of better statistics forbid a more quantitative comparison. By comparing the magnitude of the data and the model, we obtain $S_{M,xx}(0) \approx 5 \cdot 10^{-4}$ G$^2\mu$m^3. If the variation in the domain

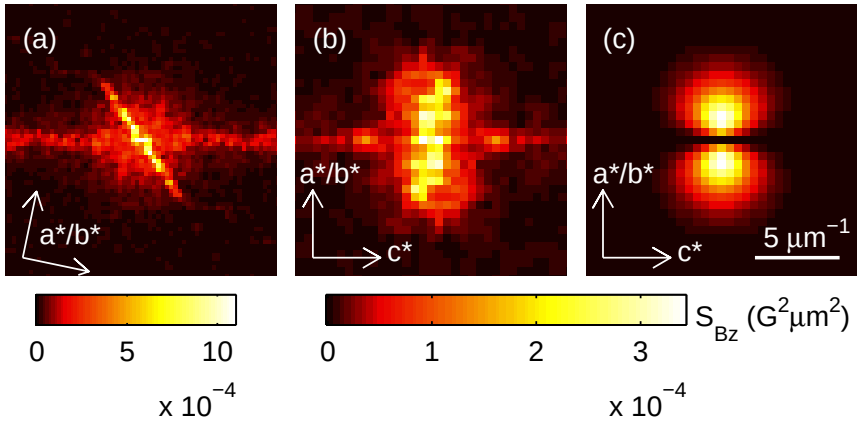

Figure 6.4: Panels (a) and (b) show estimates of the spectral densities of Fig. 6.3 (a) and (b). The faint horizontal lines at $k_y = 0$ and the sharp peak at the origin are scanning artifacts due to sensor noise. Panel (c) shows the spectrum $S_{B_z}(\vec{k})$ expected for a magnetization in the b/c-direction with all characteristic length scales of M shorter than $\min(\lambda, z_0)$. This model shows reasonable agreement with the data in (b). All plots are shown on the same scale with $k = 0$ in the center.

size is on the order of their typical size so that the correlator $\langle M_x(\vec{r})M_x(\vec{r}+\vec{r}')\rangle$ is mostly positive, $S_{M,xx}(0)$ can be interpreted as the product of a coherence volume with the typical magnetization strength $\langle M_x^2\rangle$. Using $4\pi\sqrt{\langle M_x^2\rangle} = 700$ G, one obtains an estimate of 400 nm^3 or 3000 unit cells for the domain volume. However, one should keep in mind that this interpretation is meaningless for an oscillatory magnetization.

The spectral density obtained from the *ab*-face scan [Fig. 6.3(a)] as shown in Fig. 6.4(a) on the contrary is dominated by the diagonal feature near $\vec{k} = 0$, which stems from the stripes in the scan. Its narrow shape indicates a long correlation length on the order of the scan size or larger parallel to the stripes. This suggests that there is a net average magnetization related to the twin boundaries which does not change signs over at least tens of μm. It is interesting to note that this observation implies that there is a preferred field direction attached to either the twin domains or their boundaries. Additionally, Fig. 6.4(a) shows a broader, isotropic peak. This is probably of similar origin as the peaks in Fig. 6.4(b). The lack of anisotropy can be explained by averaging over different orientations of the easy axis in different twin

domains.

Our main result is thus that in near zero field, no magnetization-induced vortices appear down to 1.9 K. In other words, $ErNi_2B_2C$ shows no spontaneous vortex lattice in the strictest sense, which would form upon cooling below the ferromagnetic transition temperature in zero field. However, the term "spontaneous" has also been used to describe a vortex lattice that forms only when aligning the magnetic domains with a sufficiently large magnetic field, but persists after returning to zero field. SANS experiments [70] on $ErNi_2B_2C$ indeed detect a lattice after, but not before cycling the field. However, the absence of the SANS vortex lattice signal in a zero-field-cooled process does not imply the absence of vortices. Their configuration could be too disordered, or the vortex density could be too low because of hysteresis for a distinct signal to appear in the neutron data. In contrast, our results clearly indicate that there are no magnetization-induced vortices in the zero-field-cooled WFM state.

Combining our results with the SANS observation of a vortex lattice after cycling in a field, it appears that there are two metastable states at zero field in the superconducting ferromagnetic regime. It remains unclear which one of these is the true ground state. The strong vortex pinning could prevent a relaxation of the vortex state into the vortex free state after cycling the field, even if the latter would have a lower energy. In the spatially resolved magnetization data of Ref. [66], a maximum of some 850 G in the magnetic field was found in the middle of the sample when reducing the applied field from higher values to about 700 Oe, giving evidence for strong bulk pinning, rather than edge barrier effects. The pinning-induced field gradients reported there are on the order of 3 G/μm. This suggests that vortex pinning might be sufficient to maintain the magnetization after field cycling and possibly cause a vortex lattice to persist. If so, one would expect the field cycled zero field average magnetization to depend strongly on the sample size. Comparing the data from Refs. [53, 71]] and Fig. 6.1(d) indeed show variations by about a factor of two, but not as large as one might expect from the differences in sample size. However, pinning alone cannot explain the observed anisotropy of the remnant magnetization because the flux pinning appears to be relatively isotropic. [70] This suggests that the *ab*-plane ferromagnetism does play a role in stabilizing the vortex lattice by reducing the

vortex repulsion or the attraction of vortices to the sample edges and thus lowering the vortex energy. In a simple picture, once the ferromagnetic domains are aligned it would be unfavorable for a single vortex to leave the crystal below a certain vortex density even with no applied field because the internal magnetization acts as an applied field. This explanation would come very close to the notion of a spontaneous vortex lattice. It should be possible to test this hypothesis by observing the behavior of the magnetic induction (likely carried by vortices) near the edges of the sample near zero applied field after field cycling. If only bulk pinning is relevant, the field (and hence vortex density) should tend to zero approximately linearly towards the edge of the sample over macroscopic distances. If, on the other hand, the vortices are stabilized by an internal magnetization, one would expect a significant flux density penetrating the samples near the edges. Such an experiment could be carried out using scanning Hall probes, but magneto-optical imaging may also be suitable.

If the energy of the field-cycled zero field vortex state is indeed lower than that of the zero-field-cooled state observed in this work, one may ask why the transition between the two states upon reducing the temperature at zero field seems inhibited, that is why there is no accessible transition pathway. As the superconductivity is already fully developed at T_{WFM}, the only way for vortices to form would be to enter through the sample edge. Just as in ordinary superconductors, this requires an edge barrier to be overcome, which however may be modified in a nontrivial way by the ferromagnetism. Furthermore, it is not a priori clear if the energy of an isolated vortex with the moments aligned only in the region with a substantial field near its core is lower than that of the Meissner state, even if this would be the case for a fully developed spontaneous vortex lattice. Indeed, an attractive long range vortex interaction was predicted under certain assumptions in Ref. [81] in the presence of ferromagnetism.

Another interesting consideration is that with a fully developed internal field, the magnetic energy is $2 \cdot 700\text{G} \cdot 7.8\mu_B/k_B = 0.7\ \text{K}/k_B$ per Er atom. Thus, the Meissner screening might suppress the ferromagnetic transition by roughly the same amount from the value of 2.2 K obtained from magnetization measurements well above H_{c1}. This might explain the hysteresis in the ferromagnetic transition mentioned by

Kawano et al. [71] and suggests that experiments extending to lower temperatures might reveal interesting effects. A hint of those has been given in Ref. [34] where a peak in a 21 MHz $\Delta\lambda$ measurement appears at 0.45 K. This effect has been interpreted as thermally activated switching of a vortex lattice, but given the indirectness of the measurements, it is not clear that this is the only possible interpretation. Furthermore, measurements with smaller probes and a reduced sample-to-probe separation may provide more quantitative data about the domain structure and would allow single vortex resolution at higher applied fields. The observation of interacting vortices along the twin domain walls and attempts to systematically manipulate them might reveal information about the pinning potential.

In conclusion, we have observed the pinning of vortices and the development of ferromagnetism in $ErNi_2B_2C$ in small applied fields. In the antiferromagnetic phase, vortices are weakly pinned on twin domain boundaries due to the magnetostriction-induced orthorhombic to tetragonal transition associated with the antiferromagnetic order. In the ferromagnetic regime, no spontaneous vortex lattice is seen, and a very weak random magnetic signal develops, indicating the formation of domains or oscillatory order which might explain the strong increase in pinning.

Acknowledgments

We would like to thank Paul Canfield for useful discussions and providing the manuscript of Ref. [135] before publication. This work has been supported by the Department of Energy under contract DE-AC02-76SF00515. IRF and SS are supported by the National Science Foundation, Division of Materials Research under grant DMR-0134613.

Chapter 7

Magnetic fields above the surface of a superconductor with internal magnetism

Hendrik Bluhm,
Phys. Rev. B, **76**, 144507 (2007).

Abstract

The author presents a method for calculating the magnetic fields near a planar surface of a superconductor with a given intrinsic magnetization in the London limit. He computes solutions for various magnetic domain boundary configurations and derives relations between the spectral densities of the magnetization and the resulting field in the vacuum half space, which are useful if the magnetization can be considered as a statistical quantity and its features are too small to be resolved individually. The results are useful for analyzing and designing magnetic scanning experiments. Application to existing data from such experiments on Sr_2RuO_4 show that a domain wall would have been detectable, but the magnetic field of randomly oriented small domains and small defects may have been smaller than the experimental noise level.

7.1 Introduction

Starting with the discovery of ferromagnetic order in the superconductors $HoMo_6S_8$ [85, 63] and $ErRh_4B_4$ [51] about three decades ago, there has been increasing interest in superconductors with an intrinsic magnetization. In the above cases and some of the RNi_2B_2C compounds (R = rare earth), the magnetization is due to localized moments of the rare earth ions and coexists with superconductivity in some temperature range. In other materials, the conduction electrons may not only superconduct, but also carry some magnetization. A prominent example is Sr_2RuO_4 [88], which is believed to have a complex, time reversal symmetry breaking p-wave order parameter, [87] so that the orbital angular momentum of the Cooper pairs creates a magnetic moment. This is theoretically expected to cause edge currents at sample boundaries and domain walls[92, 126]. A similar effect has been suggested to occur in the d-wave superconductor $Na_xCoO_2 \cdot yH_2O$[13].

The traditional experimental techniques for studying magnetic ordering phenomena are bulk probes such as muon spin rotation (μSR) or (spin polarized) small angle neutron scattering (SANS). An alternative approach is to use magnetic scanning techniques such scanning Hall probe microscopy (SHPM), [30] scanning SQUID microscopy [74], magnetic force microscopy (MFM) [117, 102] and magneto-optical techniques[75]. These techniques measure the magnetic field some small distance above the surface of the sample as a function of position. In many cases, their resolution, which is limited by the probe size and probe–sample distance, does not quite reach the length scales typical for the magnetic structure. For example, one finds evidence for oscillatory magnetic order with a sub-penetration depth length scale in $HoMo_6S_8$ [85, 63] and $ErRh_4B_4$ [51]. For larger wave lengths, the Meissner effect in the coexisting state would screen the field and thus suppress magnetic interactions and destabilize the magnetic order. A similar situation has been observed in the superconductor $ErNi_2B_2C$ using SHPM [chapter 6]. The direct observation of the magnetic fields generated by edge currents or domain walls in Sr_2RuO_4 is an ongoing effort which has not produced any evidence so far [18, 73].

To plan such scanning experiments and to interpret the resulting data, it is important to understand to what extent the magnetic field generated by a spatially varying magnetization inside the sample is propagated to the probe. In normal materials, this is a straightforward magnetostatics problem. In superconducting samples, however, it is complicated by the Meissner screening. In this work, I present solutions for an infinite planar sample surface by incorporating the presence of a magnetization $\mathbf{M}(\mathbf{x})$ into a London model and solving the resulting equations, using a 2D Fourier transform. This approach follows earlier theoretical work on superconductors with an internal magnetization due to localized magnetic moments, [57, 20, 104, 81] but should also apply if the magnetism is of different origin, such as a spin or orbital moment of the Cooper pairs. To consider the practically very likely case where the limited measurement resolution leads to significant averaging over several domains or other features with some degree of randomness, I present a spectral analysis. The resulting relations were employed for the analysis of the data in chapter 6 and may also be used to analyze null results where no field variation is detectable at the experimental noise level. A similar analysis may also be useful for interpreting surface sensitive μSR experiments, which only average over a thin layer at the sample surface [101].

The paper is organized as follows: In section 7.2, I derive the main equations of our model from a generalized Ginzburg-Landau (GL) functional. Those equations are solved in a general framework in section 7.3. In section 7.4, I discuss simple domain wall and dipole configurations as examples. Relations between the spectral densities of the magnetization and the magnetic field in vacuum are computed in section 7.5. Section 7.6 applies the results to recent magnetic scanning work [18] on Sr_2RuO_4.

7.2 Model

In order to fully describe the interplay between magnetism and superconductivity in a phenomenological approach, the magnetization $\mathbf{M}$ and the superconducting order parameter ψ have to be computed self consistently, taking mutual interactions into account. This has been done in Refs. [57, 20, 104, 81] using the generalized GL

functional

$$F[\psi, \mathbf{M}, \mathbf{A}] = \int d^3\mathbf{r} \left[\frac{1}{2}\, a|\psi|^2 + \frac{1}{4} b|\psi|^4 + \frac{\hbar^2}{2m^*} \left| \left(i\nabla + \frac{2e}{\hbar c}\, \mathbf{A} \right) \psi \right|^2 + \frac{1}{2}\, \alpha|\mathbf{M}|^2 + \frac{1}{4}\beta|\mathbf{M}|^4 + \frac{1}{2}\gamma^2|\nabla \mathbf{M}|^2 + \frac{1}{8\pi}\mathbf{B}^2 - \mathbf{B}\cdot\mathbf{M} \right], \quad (7.1)$$

where $\mathbf{B} = \nabla \times \mathbf{A}$. In this work, I will assume this task to be partially solved by starting with a given $\mathbf{M}(\mathbf{x})$ and computing the resulting magnetic field, taking shielding currents into account. This approach is clearly justified if the magnetic energy scale is much larger than the superconducting one, so that the effect of superconductivity on magnetism can be neglected. However, it is also reasonable if the result of a self consistent calculation for $\mathbf{M}$ is (approximately) known, for example from bulk calculations, and one is mainly concerned with the effect of the reduced screening at the surface on the observable field. The errors introduced by this treatment will then primarily be due to the effect of the surface and the modified screening on $\mathbf{M}$.

Writing the order parameter as $\psi = |\psi|e^{i\phi}$ and introducing the London penetration depth defined by $\lambda^{-2} = 4\pi(|\psi|^2/m^*)e^{*2}/c^2$, variation of Eq. (7.1) with respect to $\mathbf{A}$ leads to

$$\nabla \times (\nabla \times \mathbf{A} - 4\pi\mathbf{M}) + 1/\lambda^2 \mathbf{A} = (\Phi_0/2\pi\lambda^2)\nabla\phi.$$

By performing a line integral over a closed loop after multiplying by λ^2 and using the Stokes theorem, one obtains

$$\nabla \times (\lambda^2 \nabla \times \mathbf{B}) + \mathbf{B} = 4\pi\nabla \times (\lambda^2 \nabla \times \mathbf{M}) + \Phi_0 \mathbf{f}. \quad (7.2)$$

$\mathbf{f}$ is a sum of 2D δ - functions representing vortex cores, which will be ignored in the following. This result can be obtained directly by treating the supercurrent density $\mathbf{j}_s$ as macroscopic current in the macroscopic Maxwell equation and thus substituting $\nabla \times (\mathbf{B} - 4\pi\mathbf{M}) = 4\pi/c\ \mathbf{j}_s$ into the London equation $\nabla \times (4\pi\lambda^2/c\ \mathbf{j}_s) + \mathbf{B} = \Phi_0 \mathbf{f}$. Although the above is valid for a spatially varying superfluid density $n_s = |\psi|^2/m^*$, I

will assume λ to be constant, which leads to the more familiar form

$$\nabla \times \nabla \times \mathbf{B} + 1/\lambda^2 \mathbf{B} = 4\pi \nabla \times \nabla \times \mathbf{M}. \tag{7.3}$$

I assume the magnetic superconductor to occupy the lower half space $z < 0$. In vacuum ($z > 0$), the magnetic field must satisfy $\nabla \cdot \mathbf{B} = 0$ and $\nabla \times \mathbf{B} = 0$. At the interface, the normal component of $\mathbf{B}$ and the tangential component of $\mathbf{H} = \mathbf{B} - 4\pi\mathbf{M}$ must be continuous. Note that $\mathbf{M}$ enters Eq. 7.3 only through the microscopic current density $\mathbf{j_M} = c\nabla \times \mathbf{M}$. Thus, one may also start directly from an intrinsic current density $\mathbf{j_M}$ rather than $\mathbf{M}$, which is more natural if an edge current is known from microscopic calculations, for example. The appearance of $\mathbf{M}$ in the tangential boundary condition can also be eliminated by replacing it with a discontinuity in $\mathbf{M}$ just below the surface.

7.3 Solution

In Ref. [77], the field geometry of a vortex penetrating the surface of an anisotropic superconductor for a general orientation of the vortex and the main axis of the effective mass tensor with respect to the interface has been computed. In the vortex problem, the right hand side appearing in the London equation Eq. (7.3) is a 2D delta function instead of the magnetization term. I use the same technique, but only present the calculations for the isotropic case for the sake of simplicity.

The Maxwell equations in vacuum can be satisfied by writing the magnetic field as $\mathbf{B} = -\nabla\Phi$ with $-\nabla^2\Phi = 0$. A suitable solution has to be matched to a solution of Eq. (7.3) at z = 0. I solve this problem using a 2D Fourier transform (FT) in the xy-plane, i.e. by writing a function $A(x, y, z)$ as $A(\mathbf{r}_{||}, z) = (2\pi)^{-2} \int d^2\mathbf{k} \tilde{A}(\mathbf{k}, z) e^{i\mathbf{k}\cdot\mathbf{r}_{||}}$, with $\mathbf{r}_{||} = (x, y)$ and $\mathbf{k} = (k_x, k_y)$. (Note that I use the same symbol for 2 and 3 dimensional vectors, implying that the z- component vanishes for the latter.) For $z < 0$, the field $\mathbf{B}$ is decomposed as $\mathbf{B}_0 + \mathbf{B}_1$. $\mathbf{B}_0$ is a particular solution of the inhomogeneous London equation (7.3) in full space with boundary conditions at infinity and with the right hand side suitably extended to $z > 0$. $\mathbf{B}_1$ is a general homogeneous solution

chosen to satisfy the matching condition at the interface. Under the 2D FT, Eq. (7.3) transforms into $(k^2 + 1/\lambda^2 - \partial^2/\partial z^2)\tilde{\mathbf{B}}_1 = 0$, so that $\tilde{\mathbf{B}}_1(\mathbf{k}, z) = \mathbf{B}_\mathbf{k} e^{Kz}$ with $K = \sqrt{k^2 + 1/\lambda^2}$. In vacuum, $-\nabla^2\Phi = 0$ has the solutions $\tilde{\Phi}(\mathbf{k}, z) = \Phi_\mathbf{k} e^{-kz}$ so that at $z > 0$, $\tilde{\mathbf{B}}(\mathbf{k}, z) = (-i\mathbf{k} + k\hat{\mathbf{e}}_z)\Phi_\mathbf{k} e^{-kz}$.

Hence, $\nabla \cdot \mathbf{B}_1 = 0$ together with the $\hat{\mathbf{e}}_z$, $\hat{\mathbf{k}}$ and $\hat{\mathbf{k}} \times \hat{\mathbf{e}}_z$ components of the continuity conditions for $\mathbf{B}$ and $\mathbf{H} = \mathbf{B} - 4\pi\mathbf{M}$ at $z = 0$ read

$$\begin{aligned} 0 &= i\mathbf{k} \cdot \mathbf{B}_\mathbf{k} + K\hat{\mathbf{e}}_z \cdot \mathbf{B}_\mathbf{k} \\ k\Phi_\mathbf{k} &= \hat{\mathbf{e}}_z \cdot \left(\mathbf{B}_\mathbf{k} + \tilde{\mathbf{B}}_0(\mathbf{k}, 0)\right) \\ -ik\Phi_\mathbf{k} &= \hat{\mathbf{k}} \cdot \left(\mathbf{B}_\mathbf{k} + \tilde{\mathbf{B}}_0(\mathbf{k}, 0) - 4\pi\tilde{\mathbf{M}}(\mathbf{k}, 0)\right) \\ 0 &= \left(\hat{\mathbf{k}} \times \hat{\mathbf{e}}_z\right) \cdot \left(\mathbf{B}_\mathbf{k} + \tilde{\mathbf{B}}_0(\mathbf{k}, 0) - 4\pi\tilde{\mathbf{M}}(\mathbf{k}, 0)\right). \end{aligned}$$

The last equation for the in-plane transverse component of $\mathbf{B}_\mathbf{k}$ is already decoupled and can be dropped if only the vacuum field is to be computed. Solving the first three equations for $\Phi_\mathbf{k}$ leads to

$$k(K + k)\Phi_\mathbf{k} = K\hat{\mathbf{e}}_z \cdot \tilde{\mathbf{B}}_0(\mathbf{k}, 0) + i\ \mathbf{k} \cdot \left(\tilde{\mathbf{B}}_0(\mathbf{k}, 0) - 4\pi\tilde{\mathbf{M}}(\mathbf{k}, 0)\right) \tag{7.4}$$

If the 2D FT of the inhomogeneous solution, $\tilde{\mathbf{B}}_0$, cannot be obtained directly, the 3D FT $\mathbf{B}_0(\mathbf{q})$ of $\mathbf{B}_0(\mathbf{r})$ can be obtained from $\mathbf{M}(\mathbf{q})$ by solving the 3×3 linear system

$$-\mathbf{q} \times (\mathbf{q} \times \mathbf{B}_0(\mathbf{q})) + 1/\lambda^2 \mathbf{B}_0(\mathbf{q}) = -4\pi\mathbf{q} \times (\mathbf{q} \times \mathbf{M}(\mathbf{q}))$$

The solenoidal condition $\nabla \cdot \mathbf{B}_0 = 0$ will always hold as $\mathbf{q} \cdot \mathbf{B}(\mathbf{q}) = \lambda^2\ \mathbf{q} \cdot [\mathbf{q} \times (\mathbf{q} \times \mathbf{B}(\mathbf{q})) - 4\pi\mathbf{q} \times (\mathbf{q} \times \mathbf{M}(\mathbf{q}))] = 0$. The 2D FT at $z = 0$ is then simply $\tilde{\mathbf{B}}_0(\mathbf{k}, 0) = (1/2\pi) \int dq_z \mathbf{B}_0(\mathbf{q})$ with $\mathbf{q} = \mathbf{k} + q_z\hat{\mathbf{e}}_z$. While this approach to the inhomogeneous problem is very convenient for numerical evaluation and can be generalized to the anisotropic case (cf. Ref. [77]), it is useful to derive an explicit solution. The component of $\mathbf{M}$ parallel to $\mathbf{q}$ does not contribute to $\mathbf{q} \times \mathbf{M}$. For components of $\mathbf{B}_0$ and $\mathbf{M}$ orthogonal to $\mathbf{q}$, $\mathbf{q} \cdot \mathbf{B}_0 = 0$ automatically and the vector products simplify to scalar multiplication. By decomposing $\mathbf{M}$ and $\mathbf{B}_0$ into components along the unit

vectors $\hat{\mathbf{e}}_{xy} = \mathbf{q} \times \hat{\mathbf{e}}_z / |\mathbf{q} \times \hat{\mathbf{e}}_z|$ orthogonal to $\mathbf{q}$ in the xy-plane and $\hat{\mathbf{e}}_\perp = \hat{\mathbf{q}} \times \hat{\mathbf{e}}_{xy}$, the inhomogeneous solution thus simplifies to

$$\begin{aligned} B_{0,\perp} &= \frac{k^2 + q_z^2}{1/\lambda^2 + k^2 + q_z^2} 4\pi M_\perp \\ B_{0,xy} &= \frac{k^2 + q_z^2}{1/\lambda^2 + k^2 + q_z^2} 4\pi M_{xy} \end{aligned} \tag{7.5}$$

To evaluate Eq. (7.4), the inverse z-FT must be carried out in order to obtain the values at $z = 0$, unless $\mathbf{M}$ is z- independent. It turns out that $B_{0,xy}$ does not enter Eq. (7.4) because of the dot product with $\mathbf{k}$. Projecting $B_{0,\perp}$ onto the z and $\hat{\mathbf{k}}$ direction, substituting Eq. (7.5), and expressing everything in terms of M_z and $\hat{\mathbf{k}} \cdot \mathbf{M}$ using $M_\perp = \frac{-k}{\sqrt{q_z^2+k^2}} M_z + \frac{q_z}{\sqrt{q_z^2+k^2}} \hat{\mathbf{k}} \cdot \mathbf{M}$ leads to

$$\begin{aligned} k(K+k)\Phi_{\mathbf{k}} = 2 \int dq_z \, \frac{k^2(K - iq_z)}{1/\lambda^2 + k^2 + q_z^2} M_z(\mathbf{q}) \\ - 2i \int dq_z \, \frac{K(K - iq_z)}{1/\lambda^2 + k^2 + q_z^2} \mathbf{k} \cdot \mathbf{M}(\mathbf{q}) \end{aligned} \tag{7.6}$$

The iq_z terms in the numerator of the fractions can be dropped if one uses the convention that $\mathbf{M}$ is extended to $z > 0$ as an even function so that those terms do not contribute to the integrals. Eq. (7.6) can be summarized qualitatively as follows: For in-plane components of $\mathbf{M}$, the source of $\mathbf{B}$ outside the superconductor is the divergence of $\mathbf{M}$ averaged over one penetration depth below the surface. For the normal component, an additional derivative is taken, thus increasing the multipole order of the vacuum field by one. The small k components of the field are just those resulting from the subsurface magnetization and its image obtained by reflection about a plane λ below the surface.

I would like to point out that for the solution method to work as described, the interface must be planar and λ^2 should be constant. $\mathbf{M}$ on the contrary can be an arbitrary function. However, if $\nabla \times \mathbf{M} = 0$ so that $\mathbf{B}_0 = 0$ solves Eq. (7.2), the requirement that λ^2 may not depend on z can be dropped at the expense of solving a more complicated ordinary differential equation instead of the Laplace equation

to obtain $\tilde{\mathbf{B}}_1(\mathbf{k}, z)$. For example, discontinuities in λ^2 as a function of z could be treated by matching additional continuity conditions. A dependence of λ^2 on x or y on the other hand would mix different $\mathbf{k}$ components and thus generally forbid a simple analytic solution.

7.4 Examples

7.4.1 Discussion of Table 7.1

As examples for various simple, representative configurations in $\mathbf{M}$, I have calculated the field of ferromagnetic domain walls, where $\mathbf{M}$ changes sign, and dipoles at the surface. For $z \gg \lambda$, simple approximate expressions in real space can be obtained. The results are shown in table 7.1. The approximations are based on the fact that for $z \gg \lambda$, only $k_x \ll 1/\lambda$ contributes to the Fourier integral $B_z(x, z)$. To second order, $1/(K+|k|) \approx \lambda e^{-|k|\lambda}$ and $K \approx (1/\lambda)(1+(k\lambda)^2/2)$. Thus, the approximations in table 7.1 are good to three and two orders beyond leading order in k for cases (1),(3) and (2), (4), respectively. In the following, I discuss the far fields obtained from these approximations. To understand those, it is useful to recall that for magnetostatic problems in the absence of macroscopic or supercurrents, $-\nabla^2\Phi = -4\pi\nabla\cdot\mathbf{M}$. Thus, $\nabla\cdot\mathbf{M}$ acts as a magnetic charge by analogy with electrostatics. The field of a discontinuity of the in-plane component of $\mathbf{M}$ [case (1)] is just twice that of a magnetically charged line with linear charge density $4\pi\ 2M\ \lambda$ situated λ below the surface. It can be understood as the charge density due to the discontinuity of $2M$ in the magnetization, which is screened by supercurrents over one penetration depth. The additional factor two formally comes from the extension of M to $z > 0$. For a discontinuity in the normal component M_z [case (2)], one obtains the dipole field of two lines of opposite magnetic charge with a charge density $M\lambda$ as above and a separation of λ. Again, this can be understood as the screened field of the discontinuity in the magnetization occurring at the surface.

The localized dipole pointing into or out of the surface [case (3)] has a a quadrupole field. An in-plane moment [case (4)] on the contrary has a dipole field to leading order.

For a dipole chain, i.e. $\mathbf{M} = \tilde{m}\delta(x)\delta(y)\hat{\mathbf{e}}_z$, I obtain the same results as for a single dipole oriented in the z direction [case (3)] with $m = \lambda\tilde{m}$. The same analogy can be drawn for case (4).

It is also of interest to consider a configuration where a magnetization $M\hat{\mathbf{e}}_z$ is localized over a width w around $x = 0$. This situation may be encountered at an antiferromagnetic domain wall, where canting of antiferromagnetically ordered in-plane moments produces a local net out-of-plane magnetization. The corresponding exact solution is a superposition of two solutions for normal discontinuities with opposite signs, shifted by w. If w is smaller than all other length scales, $M(x)$ can be replaced by a delta function: $M(x) \approx (\int M(x')\, dx')\delta(x) = wM\delta(x)$. The resulting field is then simply the derivative of that of a discontinuity in M_z, i.e. for $z \gg \lambda$,

$$B_z(x,z) \;\approx\; -4M\lambda^2 w \frac{d^2}{dx^2}\frac{(z+\lambda)}{(z+\lambda)^2+x^2}$$

7.4.2 Periodic configurations

If the magnetization is periodic, the Fourier integrals turn into Fourier sums. If the period L is large ($L \gtrsim 2\pi z$), features with size comparable to L can be resolved in each unit cell individually and look similar to a solution obtained from a constant continuation of $\mathbf{M}$ outside that cell. For shorter periods however, the superposition of many such single cell solutions largely cancels out. Formally, this follows from the fact that the wave vector k takes only integer multiples of $2\pi/L$. Therefore, the dominant contributions at $k \lesssim 1/z$ considered in table 7.1 are not present an the leading term becomes that of the lowest wave vector $k = 2\pi/L$. This results in an exponential suppression by $e^{-2\pi z/L}$ of the lowest harmonic of the field variation at a height z above the surface and all higher harmonics being negligible for $z \gtrsim L$.

7.4.3 Effect of smoothing

As the exponential cutoff in the inverse FT becomes increasingly sharper for larger z, the far field from any feature of finite size in the magnetization will always be

Case	$\mathbf{M}(\mathbf{r})$	B_z (exact)	B_z (approximate)
(0)	$M(x)\,\hat{\mathbf{e}}_y$	0	0
(1)	$M\mathrm{sgn}(x)\hat{\mathbf{e}}_x$	$\int dk\ \frac{-4M}{\lvert k\rvert + K} e^{ikx} e^{-\lvert k\rvert z}$	$-4M \int dk\ \lambda e^{ikx} e^{-\lvert k\rvert (z+\lambda)}$ $= -8M\lambda \frac{z+\lambda}{(z+\lambda)^2 + x^2}$
(2)	$M\mathrm{sgn}(x)\hat{\mathbf{e}}_z$	$\int dk\ \frac{4M(-ik)K e^{ikx} e^{-\lvert k\rvert z}}{(1/\lambda^2 + k^2)(\lvert k\rvert + K)}$	$4M \int dk\ (-ik)\lambda^2 e^{ikx} e^{-\lvert k\rvert (z+\lambda)}$ $= -8M\lambda^2 \frac{d}{dx} \frac{z+\lambda}{(z+\lambda)^2 + x^2}$
(3)	$m\hat{\mathbf{e}}_z \delta^3(\mathbf{r})$	$\int_0^\infty dk\ \frac{2mk^3}{k+K} J_0(kr) e^{-kz}$	$2m \int_0^\infty dk\ k^3 \lambda J_0(kx) e^{-k(z+\lambda)}$ $= 2m\lambda \frac{6(z+\lambda)^3 - 9r^2(z+\lambda)}{((z+\lambda)^2 + r^2)^{7/2}}$
(4)	$m\hat{\mathbf{e}}_x \delta^3(\mathbf{r})$	$\int_0^\infty dk\ \frac{2mk^2 K}{k+K} \cos\varphi J_1(kr) e^{-kz}$	$2m\cos\varphi \int_0^\infty dk\, k^2 J_1(kr) e^{-k(z+\lambda)}$ $= 2m\cos\varphi \frac{3r(z+\lambda)}{(r^2 + (z+\lambda^2))^{5/2}}$

Table 7.1: Exact and approximate expressions for the magnetic field above the superconductor for domain walls and dipoles with an in-plane and out-of-plane magnetization. In case (4), φ is the angle between the x-axis and $\mathbf{r}$. The approximate expressions in the last column are valid for $z \gg \lambda$.

determined by the lowest non-vanishing power of k in $k\Phi_{\mathbf{k}}$ for sufficiently large z. For a smooth domain wall, $\mathbf{M}(\mathbf{q})$ has less weight at large $\mathbf{q}$ compared to a sharp discontinuity of equal magnitude, but the values at small $\mathbf{q}$ are affected little. Thus, the asymptotic results for sharp discontinuities in $\mathbf{M}$ are still valid if $\mathbf{M}$ changes smoothly over a width w as long as $z \gg w$. For example, the far field of a single domain boundary does not depend on the length scale over which the magnetization changes in the xy-plane, but only on the difference between the asymptotic values of M on both sides. Hence, the approximate results in table 7.1 are of rather general validity. For a graphic illustration, see Fig. 7.2, which is discussed in Sec. 7.6.

The situation is slightly different for a nontrivial z-dependence of $\mathbf{M}$: the q_z-cutoff is always determined by the $1/(1+(\lambda q_z)^2)$ factor for small k. In real space, this corresponds to an exponentially weighted average over a distance of λ below the surface.

7.5 Spectral Analysis

The resolution of currently available magnetic imaging techniques is often not sufficient to resolve an actual domain structure. In practice, averaging occurs both due to the imaging height z and the finite sensor size. Here, I will only consider the more universal height effect. For a height larger than the typical domain size, the magnetic field represents an average over several domains. As shown in the previous section, this would lead to an exponential suppression for periodic configurations. However, domains will usually not be strictly periodic, but have some distribution of size. Therefore, a statistical description is most adequate. Assuming a given correlation function and thus spectrum of the magnetization $\mathbf{M}(\mathbf{r})$, I compute the spectrum of the resulting magnetic field.

The spectral function of two functions $f(\mathbf{r})$ and $g(\mathbf{r})$ in d dimensions, $S_{fg}(\mathbf{q}) = \int d^d\mathbf{r}' \langle f(\mathbf{r})\, g(\mathbf{r}+\mathbf{r}')\rangle e^{-i\mathbf{r}'\cdot\mathbf{q}}$, satisfies the relation $\langle f(\mathbf{q})^* g(\mathbf{q}')\rangle = (2\pi)^d \delta^d(\mathbf{q}-\mathbf{q}') S_{fg}(\mathbf{q})$ Here, $\langle\cdot\rangle$ stands for an ensemble average over different realizations of f and g. It is implicit to this definition that the correlator $\langle f(\mathbf{r})\, g(\mathbf{r}+\mathbf{r}')\rangle$ is independent of $\mathbf{r}$.

It is convenient to introduce the propagation coefficients

$$\begin{aligned} c_{\mathbf{q},z} &= 2k^2\lambda^2\gamma_{\mathbf{q}} \\ c_{\mathbf{q},\alpha} &= -2ik_\alpha K\lambda^2\gamma_{\mathbf{q}} \quad (\alpha = x,y) \qquad (7.7) \\ \gamma_{\mathbf{q}} &= \frac{(K-iq_z)e^{-kz}}{\lambda^2(k+K)(1/\lambda^2+k^2+q_z^2)} \qquad (7.8) \end{aligned}$$

and rewrite Eq. (7.6), using $\tilde{B}_z(\mathbf{k},z) = k\Phi_{\mathbf{k}} e^{-kz}$, as $B_z(z_0,\mathbf{k}) = \int dq_z \sum_\alpha c_{\mathbf{q},\alpha} M_\alpha(\mathbf{q})$.

It follows that

$$S_{B_z}(\mathbf{k},z) = 2\pi\int dq_z \sum_{\alpha,\beta} c^*_{\mathbf{q},\alpha}c_{\mathbf{q},\beta}S_{M,\alpha\beta}(\mathbf{q}) \tag{7.9}$$

$$= 2\pi\int dq_z \sum_{\alpha} |c_{\mathbf{q},\alpha}|^2 S_{M,\alpha\alpha}(\mathbf{q})$$

$$+ 4\pi\int dq_z \sum_{\alpha\neq\beta} \mathrm{Re}(c^*_{\mathbf{q},\alpha}c_{\mathbf{q},\beta}S_{M,\alpha\beta}(\mathbf{q})). \tag{7.10}$$

I have used $S_{M,\alpha\beta}$ as a short hand notation for the spectral function $S_{M\alpha M\beta}$ of two different components of $\mathbf{M}$. Similar expressions can be written down for spectral densities involving other components of $\mathbf{B}$.

Because of the presence of the surface, the assumption of translational invariance in the z-direction implicit to the definition of S_M is by no means trivial. If the presence of the surface does not affect the structure of $\mathbf{M}$ too much, and the range of the surface influence is much shorter than λ, most of it should average out because B_z is sensitive to what happens within a layer of thickness λ below the surface. However, the z-invariance is only required in order to define spectral functions $S_{M,\alpha\beta}$. If the interface (or other effects) do break the z-invariance of $\langle M_\alpha(\mathbf{r})\ M_\beta(\mathbf{r}+\mathbf{r}')\rangle$ so that it depends on both z and z', it is still possible to derive an expression for S_{B_z} similar to Eq. (7.10), however involving a double integral over q_z.

A statistical analysis will be most relevant when the measurement height z is much larger than any of the intrinsic length scales of the variation of $\mathbf{M}$, i.e. too large to resolve individual features. In this case, $S_M(\mathbf{k}+q_z\hat{\mathbf{e}}_z)$ will not have a strong $\mathbf{k}$ dependence in the small $\mathbf{k}$ region surviving the e^{-kz} cutoff and can be approximated by $S_M(q_z\hat{\mathbf{e}}_z)$. For $z \gg \lambda$, a similar approximation can be made for the propagation coefficients $c_{\mathbf{q},\alpha}$ and $\gamma_{\mathbf{q}}$:

$$c_{\mathbf{q},\alpha} \approx -2ik_\alpha\lambda\gamma_{\mathbf{q}} \quad (\alpha = x,y) \tag{7.11}$$

$$|\gamma_{\mathbf{q}}|^2 \approx \frac{e^{-2k(z+\lambda)}}{1+q_z^2\lambda^2} \tag{7.12}$$

In any case, the properties of $\mathbf{M}$ only enter via the integrals

$$\int dq_z \frac{1}{1+k^2\lambda^2+q_z^2\lambda^2} S_{M,\alpha\beta}(\mathbf{q}) \tag{7.13}$$

As argued above, it will often be a good approximation to set $\mathbf{k}=0$. In many cases, $S_M(q_z\hat{\mathbf{e}}_z)$ will have a peak at some wave vector q_0 (and consequently at $-q_0$), similar to the illustration in Fig. 7.1. For simplicity, I assume that there is only one such maximum. A finite q_0 is a signature of an oscillatory behavior of $\mathbf{M}$. The width of the peak corresponds to the inverse coherence length of the oscillation or the correlation length for $q_0=0$.

The integral (7.13) can be approximated further in two limiting cases. If the coherence length of $\mathbf{M}$ along the z direction is much larger than λ, then $S_M(q_z\hat{\mathbf{e}}_z)$ is sharply peaked, and the kernel $1/(1+q_z^2\lambda^2)$ can be replaced by $1/(1+q_0^2\lambda^2)$ and pulled out of the integral. In the opposite limit, the peak in $S_M(q_z\hat{\mathbf{e}}_z)$ is much wider than $1/\lambda$ so that the q_z dependence of S_M can be neglected entirely and one obtains

$$\int dq_z \frac{1}{1+q_z^2\lambda^2} S_{M,\alpha\beta}(\mathbf{q}) \approx (\pi/\lambda) S_M(0)$$

Assuming that the α-component of $\mathbf{M}$ dominates, the respective diagonal term of Eq. (7.10) takes the form

$$S_{B_z}(\mathbf{k}) = (8\pi^2/\lambda)(k_\alpha\lambda)^2 e^{-2k(z+\lambda)} S_{M,\alpha\alpha}(0)$$

for $\alpha = x, y$. If the M_z component is dominant, $(k_\alpha\lambda)^2$ in the prefactor must be replaced by $(k\lambda)^4$. Similar expressions can be written down for the off-diagonal components of $S_{M,\alpha\beta}$. For an illustration of the relation between a measured B_z and its spectral function, the reader is referred to chapter 6. Integration leads to simple expressions for $\langle B_z^2\rangle = (2\pi)^{-2}\int d^2\mathbf{k} S_{B_z}(\mathbf{k})$:

$$\langle B_z^2\rangle = \frac{3\pi}{4}\frac{\lambda}{(z+\lambda)^4} S_{M,\alpha\alpha}(0) \quad \text{for } \alpha = x, y \tag{7.14}$$

$$\langle B_z^2\rangle = \frac{15\pi}{2}\frac{\lambda^3}{(z+\lambda)^6} S_{M,zz}(0). \tag{7.15}$$

Those expressions can be used to estimate the signal expected in a scanning experiment or to estimate $S_M(0)$ from the observed field variation. Note that if the variation of the domain size is sufficiently large for $\langle \mathbf{M}(\mathbf{r})\mathbf{M}(\mathbf{r}+\mathbf{r}')\rangle$ to be essentially non-negative, as for the exponential width distribution in Fig. 7.1, $S_{M,\alpha\alpha}(0) = \int d^3\mathbf{r}'\langle M_\alpha(\mathbf{r})M_\alpha(\mathbf{r}+\mathbf{r}')\rangle$ can be interpreted as the product of a correlation volume $\int d^3\mathbf{r}'\langle M_\alpha(\mathbf{r})M_\alpha(\mathbf{r}+\mathbf{r}')\rangle/\langle M_\alpha^2\rangle$ and the mean square magnetization $\langle M_\alpha^2\rangle$.

7.6 Application to Sr_2RuO_4

Based on various evidence, it is believed that Sr_2RuO_4 is a spin triplet superconductor with a p-wave order parameter of the same symmetry class as $k_x \pm ik_y$ [87, 103]. Convincing evidence that the order parameter is indeed time-reversal symmetry breaking (TRSB) has recently been obtained by Sagnac-interferometry experiments [144]. Such a TRSB order parameter is expected to cause chiral currents at sample edges, domain walls or impurities. [92, 126] The direct observation of such effects in Sr_2RuO_4 is an ongoing effort. So far, the most direct indication of spontaneous fields is given by μSR data, reporting "a broad distribution of fields arising from a dilute distribution of sources" [84]. Phase sensitive tunneling measurements support the notion of small chiral domains [72]. Scanning Hall probe and scanning SQUID microscopy experiments [18, 73, 44] on the other hand did not detect any sign of a spontaneous magnetization associated with superconductivity.

The magnetic scans of the *ab*-face in Ref. [18] showed neither localized features nor a random field variation that could be attributed to TRSB. Even holes that were drilled using a focused ion beam (FIB) failed to show a magnetic signature. Lacking suitable theoretical models, a quantitative analysis of those null results was inconclusive. In this section, I will use the results derived above to compute the expected field from domains and defects. This allows to set certain limits on the internal magnetization strength that would be consistent with the data.

A complete description of chiral domains requires a self consistent computation of the order parameter and magnetic fields. This has been carried out using microscopic theory [92] and a GL approach[126] without considering the effect of a surface. Such

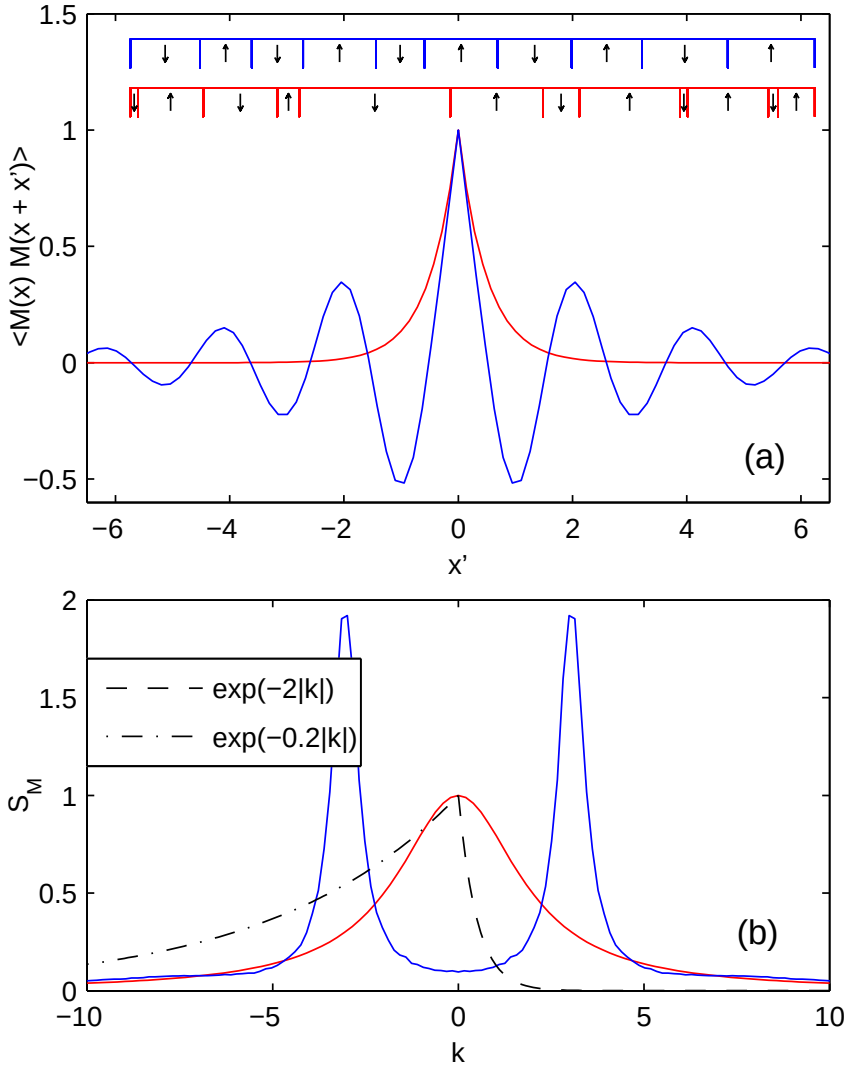

Figure 7.1: Illustration of different one-dimensional domain structures for $|M| = 1$. (a) Correlator of M, and small sample of the corresponding real space domain structure (inset). (b) Corresponding spectral functions. The domain width in the red (lower) structure is exponentially distributed with mean 1, which gives $\langle M(x)M(x+x')\rangle = e^{-2|x'|}$ and $S_M(k) = 1/(1+k^2/4)$. The domain width in the blue (upper) structure has a Gaussian distribution with mean 1 and standard deviation 0.3, leading to an oscillatory correlator and peaks in the spectral function at $k = \pm\pi$. The curves for this case were obtained numerically from an ensemble of 10^5 domains. The dashed lines in (b) represent the propagation factors $e^{-|k|z}$ for heights $z = 2$ and $z = 0.2$. For large z, only $S_M(k \approx 0)$ is relevant.

detailed calculations generally require a numerical solution. Taking the presence of a surface into account leads to a further complication. Thus, they are rather cumbersome for the purpose of data analysis and planning experiments.

For a domain wall along the $x = 0$ plane in an infinite sample, the results of those computations generally show a current along the y-direction which decays over about one in-plane coherence length ξ_{ab} in the x-direction and changes sign. The counterflowing current decays on the scale of λ such that the magnetic field far inside each domain vanishes. Indeed, one can obtain good fits of the form

$$B_{0,z}(x) = \frac{B_0}{1 - \tilde{\xi}^2/\tilde{\lambda}^2}\mathrm{sgn}(x)(e^{-|x|/\tilde{\lambda}} - e^{-|x|/\tilde{\xi}}) \tag{7.16}$$

to the numerical results for the magnetic field of Ref. [92], with $\tilde{\lambda} = 2.2\ \xi_{ab}$, $\tilde{\xi} = 1.5\ \xi_{ab}$, and $B_0 = 87$ G. I used $\xi_{ab} = 66$ nm and $\lambda = 150$ nm [87] to compute the thermodynamic critical field entering the prefactor of the result of Ref. [92]. It is easy to show that this expression is a solution to the London equations for $\lambda = \tilde{\lambda}$ in the presence of a chiral current density $j_y(x) = -(cB_0/4\pi\tilde{\xi})e^{-|x|/\tilde{\xi}}$. This current can be identified with an internal magnetization $M_z = (B_0/4\pi)\mathrm{sgn}(x)(1 - e^{-|x|/\tilde{\xi}})$ in the z direction due to the orbital magnetic moments of the Cooper pairs. The value of $\tilde{\lambda}$ is in good agreement with the value of $\kappa \equiv \lambda/\xi_{ab} = 2.5$ assumed in Ref. [92]. This suggests that the London approach captures screening effects quite accurately, and therefore should give a good approximation for the field above a surface. Of course, this will neglect some features in the full GL solutions. For example, the latter show a slight depression of the superfluid density near the domain wall, which is neglected here by assuming a constant λ. Similar modifications of both the superfluid density and the chiral current density at the surface should be small due to the short c-axis coherence length $\xi_c = 0.05\ \xi_{ab}$. The anisotropy is of no consequence because all currents flow along the ab-plane so that only λ_{ab} matters.

Since the far field of the domain wall only depends on the difference of the asymptotic values of M away from the domain wall, and experimentally $\xi_{ab} = 66$ nm $< \lambda = 150$ nm $\ll z \approx 1\ \mu$m, it is appropriate to use the large-z results for a sharp discontinuity in M to analyze the results of Ref. [18]. If accurate results at a $z \lessapprox 3\lambda$

are required, Eq. (7.4) together with the above approximation for $B_{0,z}(x)$ should be used. Fig. 7.2 shows the field profiles for those two methods and the exact result for a sharp domain wall at different heights.

In the experiments, the rms noise levels were 35 mG and 0.45 mG at imaging heights $z = 1.2$ μm and 2 μm in the Hall probe and SQUID scans, respectively. Correction factors due to oversampling and averaging over the size of the SQUID pickup loop are of order unity. An isolated domain wall would result in a field of $5 \cdot 10^{-3} 4\pi M = 0.4$ G and $2 \cdot 10^{-3} 4\pi M = 0.17$ G respectively at the above imaging heights and $B_0 = 87$ G, and should be clearly visible in the data. Thus, there was either no such domain wall in the scanned area, or its magnetization was $4\pi M < 7$ G and $4\pi M < 0.2$ G respectively, so that it was hidden by sensor noise.

The exact calculation of the signature of a hole is more difficult because the translational invariance of the boundary conditions is broken. However, if the diameter of the hole or defect, which I assume to extend along the z-direction normal to the surface, is much smaller than λ, the absence of superfluid in it can be neglected and the dipole calculation should be a good approximation. For a hole or defect with a volume of ξ_{ab}^3, the maximum field according to case (3) in table 7.1 at $z = 1.2$ μm and 2 μm is $1.2 \cdot 10^{-5} 4\pi M = 1.1$ mG and $2 \cdot 10^{-6} 4\pi M = 0.17$ mG, respectively. This signal would be nearly undetectable at the experimental noise level of Ref. [18]. Furthermore, the extent of the defect along the z-direction could be as small as $\xi_c = 0.05\ \xi_{ab}$, and the order parameter is not necessarily suppressed entirely. For a columnar defect on the other hand, one factor of ξ_{ab} has to be replaced by λ, decreasing the limit on M only by about a factor three. Since the FIB drilled holes in the experiment were significantly larger (about 1 μm), they have both a larger moment and less effective Meissner screening. This leads to a stronger signal whose calculation goes beyond the scope of this paper.

One can also estimate the signal expected from a random configuration of small domains. The smallest conceivable domain volume is on the order of $\xi_{ab}^2 \xi_c$. Assuming that the domain size fluctuates enough to use this as correlation volume, Eq. (7.15) implies that the rms signal could be as small as 0.7 mG and 0.16 mG, again less than the experimental noise. A domain size distribution that does not satisfy the

assumptions leading to Eq. (7.15) may result in even smaller signals. Thus, the possibility of very small domains cannot be ruled out.

In all the above cases, the smaller imaging height of the Hall probe does not compensate for its large noise compared to the SQUID. Assuming the predicted magnitude of the chiral currents [92] is correct, the calculations show that any domain wall should have been detected by the measurements. Small defects on the other hand might easily have been hidden in the noise. It is also possible that a random signal from domains would have been too small to observe, especially if the domains are short in the c-direction or very homogeneous in size while not too large. However, it appears that one should not take the notion of a magnetization due to p-wave pairing too literally. It was shown [24] that the chiral currents can in general *not* be written as the curl of a global magnetization, and that the effective value of $\mathbf{M}$ depends on the type of domain wall.

Note that a similar analysis of the magnetic scanning data of Refs. [18, 73], also making use of the relations derived in Sec. 7.3, has been carried out in parallel with the present work in Ref [73].

7.7 Conclusion

I have presented a model for a superconductor with an intrinsic magnetization by combining the macroscopic magnetostatic Maxwell equation with the London relation and obtained the field geometry at a planar superconductor-vacuum interface for a given spatial variation of the magnetization. Solutions for a range of specific magnetic domain boundary configurations give simple expressions in the limit of a large height above the sample. If the height above the surface at which the magnetic field can be measured exceeds the characteristic length scale of variations in the magnetization, a spectral analysis can be used to relate the spectral densities of the two at resolvable wave vectors. If a specific model for the structure of the magnetization is at hand, a direct comparison with the measured field is possible. Otherwise, some simplifying assumptions give a simple estimate relating the spectral density of $\mathbf{M}$ at the superconductor - vacuum interface to the observable spatial rms-variation of the

magnetic field. As an example for an application, I have applied my calculations to recent experimental results on Sr_2RuO_4 [18], concluding that large chiral domains would have been visible in those experiments, but small domains and defects may have escaped detection.

Acknowledgments

I would like to thank Kam Moler, Ophir Auslaender and John Kirtley for giving feedback on the manuscript. This work has been supported by the Department of Energy under contract DE-AC02-76SF00515.

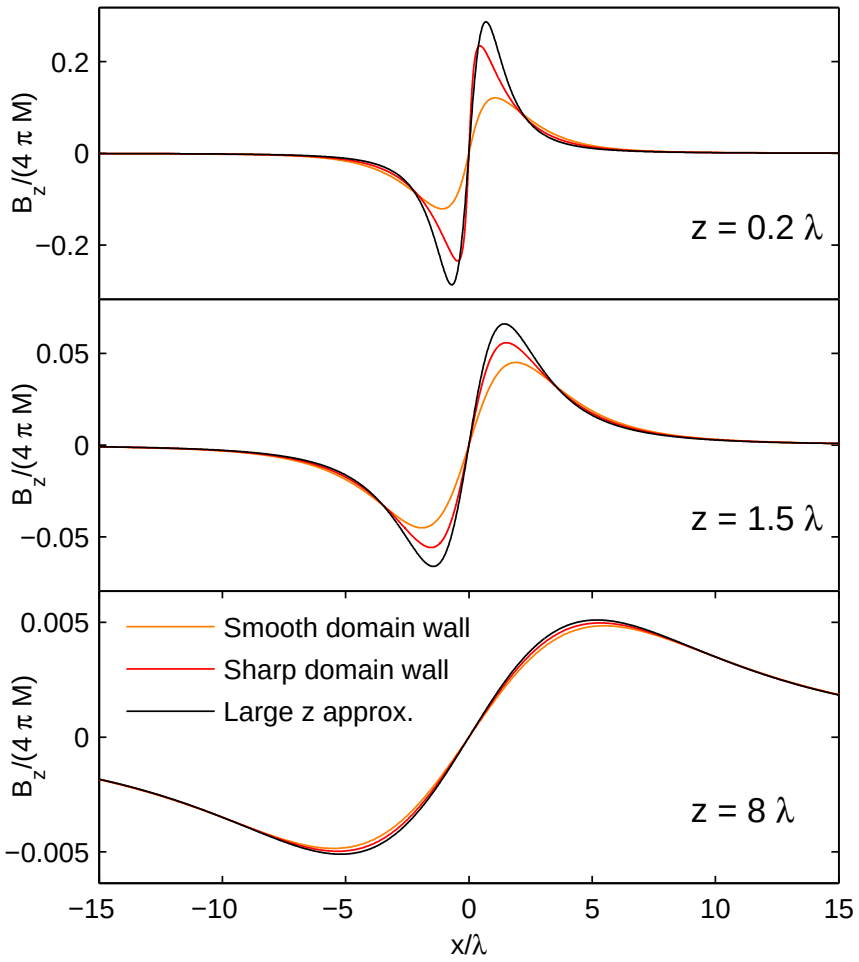

Figure 7.2: Field profile at different heights z above a domain wall were M_z changes sign. The curves labeled "smooth" and "sharp domain wall" were obtained from the full solution with $M_z(x) = M\mathrm{sgn}(x)(1 - e^{-|x|/(0.7\lambda)})$ and $M_z(x) = M\mathrm{sgn}(x)$ respectively. The latter solution and the corresponding large z approximation as shown are given by table 7.1, case (2). The value of the domain boundary width was chosen according to the fit to the numerical results for Sr_2RuO_4 from Ref. [92]. $z = 8\lambda$ corresponds to the Hall probe scans from Ref. [18].

Appendix A

List of common symbols

d	Film thickness, sometimes dimensionality
$D = v_F l_e/d$	Diffusivity
Δ	Superconducting gap
Δ_M	Level spacing
$E_c = \pi^2 \hbar D/L^2$	Correlation energy
F	Free energy
$\Phi_0 = h/2e$	Superconducting flux quantum
$\phi_0 = h/e$	Single-electron flux quantum
Φ_a	applied flux
$\varphi = \Phi_a/\Phi_0$ or Φ_a/ϕ_0	Dimensionless flux
I	Ring current
I_m	m-th harmonic of persistent current
$I_0 = ev_F l_e/L^2$	Scale of persistent currents
H_c	Thermodynamic critical field
H_{c1}	Lower critical field
H_{c2}	Upper critical field
k_F	Fermi wave vector
L	Ring circumference
l_e	Electronic mean free path
$L_\phi = \sqrt{D\tau_\phi}$	Dephasing length

$L_{so} = \sqrt{D\tau_{so}}$	Spin-orbit scattering length
λ	Penetration depth (chapters 3, 4, 7)
	Interaction constant (chapter 5)
$M = wdk_F^2/4\pi$	Number of transverse channels (chapter 5)
	Magnetization (chapter 7)
$M_{eff} = (l_e/L)M$	Effective number of channels
m_e	Electron mass
μ	Chemical potential
n	Fluxoid number
$\nu_F = m_e k_F/\hbar^2\pi^2$	Density of states at the Fermi energy
ψ	GL-order parameter
R	Ring radius, sometimes a resistance
ρ	Resistivity
σ	Conductance
τ_ϕ	Dephasing time (chapter 5)
	Phase slip duration (chapter 4)
$\tau_{\lvert\psi\rvert}$	Order parameter relaxation time
T	Temperature
T_c	Superconducting critical temperature
v_F	Fermi velocity
w	Line width
x	Position around ring
ξ	Superconducting coherence length (chapters 3, 4)
	Localization length (chapter 5)
$\xi_0 = \hbar v_F/\pi\Delta$	Pippard (clean limit, $T = 0$) coherence length.

Bibliography

[1] B. L. Altshuler, A. G. Aronov, and B. Z. Spivak. The Aaronov-Bohm effect in disordered conductors. *JETP Lett.*, 33(2):94 – 97, 1981.

[2] B. L. Altshuler, Y. Gefen, and Y. Imry. Persistent differences between canonical and grand canonical averages in mesoscopic ensembles: large paramagnetic orbital susceptibilities. *Phys. Rev. Lett.*, 66(1):88 – 91, 1991.

[3] V. Ambegaokar and A. Baratoff. Erratum: tunneling between superconductors. *Phys. Rev. Lett.*, 11(2):104 – 104, 1963.

[4] V. Ambegaokar and A. Baratoff. Tunneling between superconductors. *Phys. Rev. Lett.*, 10(11):456 – 459, 1963.

[5] V. Ambegaokar and U. Eckern. Coherence and persistent currents in mesoscopic rings. *Phys. Rev. Lett.*, 65(3):381 – 4, 1990.

[6] V. Ambegaokar and U. Eckern. Nonlinear diamagnetic response in mesoscopic rings of superconductors above t_c. *Europhysics Letters*, 13(8):733 – 8, 1990.

[7] A. J. Annunziata, A. Frydman, M. O. Reese, L. Frunzio, M. Rooks, and D. E. Prober. Superconducting niobium nanowire single photon detectors. *Proc. of SPIE - The International Society for Optical Engineering*, 6372, 2006.

[8] A. Anthore, H. Pothier, and D. Esteve. Density of states in a superconductor carrying a supercurrent. *Phys. Rev. Lett.*, 90(12):127001 – 4, 2003.

[9] E. Babaev. Vortices with fractional flux in two-gap superconductors and in extended faddeev model. *Phys. Rev. Lett.*, 89(6):067001 – 4, 2002.

[10] E. Babaev. Phase diagram of planar $u(1) * u(1)$ superconductor. condensation of vortices with fractional flux and a superfluid state. *Nuclear Physics B*, B686(3):397 – 412, 2004.

[11] E. Babaev, A. Sudbo, and N. W. Ashcroft. A superconductor to superfluid phase transition in liquid metallic hydrogen. *Nature*, 431(7009):666 – 8, 2004.

[12] A. Baratoff. Self-consistent nonequilibrium description of phase-slip states in superconducting filaments. *Phys. Rev. Lett.*, 48(6):434 – 8, 1982.

[13] G. Baskaran. Electronic model for CoO_2 layer based systems: chiral resonating valence bond metal and superconductivity. *Phys. Rev. Lett.*, 91(9):097003 – 4, 2003.

[14] J. Berger. Flux transitions in a superconducting ring. *Phys. Rev. B*, 67(1):14531 – 1, 2003.

[15] P. Bertet, I. Chiorescu, G. Burkard, K. Semba, C. J. P. M. Harmans, D. P. DiVincenzo, and J. E. Mooij. Dephasing of a superconducting qubit induced by photon noise. *Phys. Rev. Lett.*, 95(25):257002 – 4, 2005.

[16] Norman O. Birge and F. Pierre. Dephasing by extremely dilute magnetic impurities revealed by aharonov-bohm oscillations. *Phys. Rev. Lett.*, 89(20):2068041 – 2068044, 2002.

[17] P. G. Bjornsson, B. W. Gardner, J. R. Kirtley, and K. A. Moler. Scanning superconducting quantum interference device microscope in a dilution refrigerator. *Rev. Sci. Inst.*, 72(11):4153 – 8, 2001.

[18] P. G. Bjornsson, Y. Maeno, M. E. Huber, and K. A. Moler. Scanning magnetic imaging of Sr_2RuO_4. *Phys. Rev. B*, 72(1):012504 – 1, 2005.

[19] K. Bladh, D. Gunnarsson, E. Hurfeld, S. Devi, C. Kristoffersson, B. Smalander, S. Pehrson, T. Claeson, P. Delsing, and M. Taslakov. Comparison of cryogenic filters for use in single electronics experiments. *Rev. Sci. Inst.*, 74(3):1323 – 7, 2003.

[20] E. I. Blount and C. M. Varma. Electromagnetic effects near the superconductor-to-ferromagnet transition. *Phys. Rev. Lett.*, 42(16):1079 – 82, 1979.

[21] H. Bluhm, Julie A. Bert, N. C. Koshnick, M. E. Huber, and K. A. Moler. (unpublished).

[22] H. Bluhm, N. C. Koshnick, M. E. Huber, and K. A. Moler. Magnetic response of mesoscopic superconducting rings with two order parameters. *Phys. Rev. Lett.*, 97(23):237002 – 4, 2006.

[23] O. Bourgeois, S. E. Skipetrov, F. Ong, and J. Chaussy. Attojoule calorimetry of mesoscopic superconducting loops. *Phys. Rev. Lett.*, 94(5):057007, 2005.

[24] V. Braude and E. B. Sonin. Orbital magnetic dynamics in chiral p-wave superconductors. *Phys. Rev. B*, 74(6):64501 – 1, 2006.

[25] C. Buzea and T. Yamashita. Review of the superconducting properties of MgB_2. *Superconductor Science & Technology*, 14(11):R115 – 46, 2001.

[26] N. Byers and C. N. Yang. Theoretical considerations concerning quantized magnetic flux in superconducting cylinders. *Phys. Rev. Lett.*, 7(2):46 – 49, 1961.

[27] P. C. Canfield, S. L. Budko, and B. K. Cho. Possible co-existence of superconductivity and weak ferromagnetism in $ErNi_2B_2C$. *Physica*, 262C(3/4):249 – 54, 1996.

[28] R. J. Cava, H. Takagi, H. W. Zandbergen, J. J. Krajewski, W. F. Peck, T. Siegrist, B. Batlogg, R. B. Vandover, R. J. Felder, K. Mizuhashi, J. O. Lee, H. Eisaki, and S. Uchida. Superconductivity in the quaternary intermetallic compounds $LnNi_2B_2C$. *Nature (London)*, 367(6460):252 – 3, 1994.

[29] V. Chandrasekhar, R. A. Webb, M. J. Brady, M. B. Ketchen, W. J. Gallagher, and A. Kleinsasser. Magnetic response of a single, isolated gold loop. *Phys. Rev. Lett.*, 67(25):3578 – 81, 1991.

[30] A. M. Chang, H. D. Hallen, L. Harriott, H. F. Hess, H. L. Kao, J. Kwo, R. E. Miller, R. Wolfe, J. Vanderziel, and T. Y. Chang. Scanning hall probe microscopy. *Applied Physics Letters*, 61(16):1974 – 6, 1992.

[31] H. F. Cheung, Y. Gefen, E. K. Riedel, and W. H. Shih. Persistent currents in small one-dimensional metal rings. *Phys. Rev. B*, 37(11):6050 – 62, 1988.

[32] Ho-Fai Cheung and E. K. Riedel. Energy spectrum and persistent current in one-dimensional rings. *Phys. Rev. B*, 40(14):9498 – 501, 1989.

[33] Ho-Fai Cheung, E. K. Riedel, and Y. Gefen. Persistent currents in mesoscopic rings and cylinders. *Phys. Rev. Lett.*, 62(5):587 – 90, 1989.

[34] E. E. M. Chia, M. B. Salamon, T. Park, H. J. Kim, S. I. Lee, and H. Takeya. Observation of the spontaneous vortex phase in the weakly ferromagnetic superconductor $ErNi_2B_2C$: A penetration depth study. *Europhys. Lett.*, 73(5):772 – 778, 2006.

[35] B. K. Cho, P. C. Canfield, L. L. Miller, D. C. Johnston, W. P. Beyermann, and A. Yatskar. Magnetism and superconductivity in single-crystal $ErNi_2B_2C$. *Phys. Rev. B*, 52(5):3684 – 95, 1995.

[36] S. M. Choi, J. W. Lynn, D. Lopez, P. L. Gammel, P. C. Canfield, and S. L. Bud'ko. Direct observation of spontaneous weak ferromagnetism in the superconductor. *Phys. Rev. Lett.*, 87(10):107001 – 4, 2001.

[37] Suk Bum Chung, Hendrik Bluhm, and Eun-Ah Kim. Stability of half-quantum vortices in $p_x + ip_y$ superconductors. *Physical Review Letters*, 99(19):197002, 2007.

[38] R. W. Cohen and B. Abeles. Superconductivity in granular aluminium films. *Phys. Rev.*, 168(2):444 – 450, 1968.

[39] S. Das Sarma, C. Nayak, and S. Tewari. Proposal to stabilize and detect half-quantum vortices in strontium ruthenate thin films: non-abelian braiding statistics of vortices in a $p_x + ip_y$ superconductor. *Phys. Rev. B*, 73(22):220502(R) – 1, 2006.

[40] R. Deblock, R. Bel, B. Reulet, H. Bouchiat, and D. Mailly. Diamagnetic orbital response of mesoscopic silver rings. *Phys. Rev. Lett.*, 89(20):206803 – 4, 2002.

[41] R. Deblock, Y. Noat, B. Reulet, H. Bouchiat, and D. Mailly. ac electric and magnetic responses of nonconnected aharonov-bohm rings. *Phys. Rev. B*, 65(7):075301 – 14, 2002.

[42] C. Detlefs, A. H. M. Z. Islam, T. Gu, A. I. Goldman, C. Stassis, P. C. Canfield, J. P. Hill, and T. Vogt. Magnetoelastic tetragonal-to-orthorhombic distortion in $ErNi_2B_2C$. *Phys. Rev. B*, 56(13):7843 – 6, 1997.

[43] C. D. Dewhurst, S. S. James, R. A. Doyle, Y. Paltiel, H. Shtrikman, E. Zeldov, and D. McK. Paul. Vortex pinning by magnetic order in $ErNi_2B_2C$. *Phys. Rev. B*, 63(6):060501(R) – 4, 2000.

[44] V. O. Dolocan, C. Veauvy, F. Servant, P. Lejay, K. Hasselbach, Y. Liu, and D. Mailly. Observation of vortex coalescence in the anisotropic spin-triplet superconductor Sr_2RuO_4. *Phys. Rev. Lett.*, 95(9):097004 – 4, 2005.

[45] P. Dubos, P. Charlat, Th. Crozes, P. Paniez, and B. Pannetier. Thermostable trilayer resist for niobium lift-off. *J. Vac. Sci. Technol. B*, 18(1):122 – 6, 2000.

[46] U. Eckern and P. Schwab. Persistent currents versus phase breaking in mesoscopic metallic samples. *J. Low Temp. Phys.*, 126(3/4):1291 – 304, 2002.

[47] U. Eckern, P. Schwab, and V. Ambegaokar. Comment on "magnetic response of disordered metallic rings: large contributions of far levels". *Phys. Rev. Lett.*, 93(20):209701 –, 2004.

[48] J. T. Edwards and D. J. Thouless. Numerical studies of localization in disordered systems. *Journal of Physics C (Solid State Physics)*, 5(8):807 – 20, 1972.

[49] H. Eisaki, H. Takagi, R. J. Cava, B. Batlogg, J. J. Krajewski, W. F. Peck, K. Mizuhashi, J. O. Lee, and S. Uchida. Competition between magnetism and superconductivity in rare-earth nickel boride carbides. *Phys. Rev. B*, 50(1):R647 – 50, 1994.

[50] O. Entin-Wohlman, Y. Gefen, Y. Meir, and Y. Oreg. Effects of spin-orbit scattering in mesoscopic rings: canonical-versus grand-canonical-ensemble averaging. *Phys. Rev. B*, 45(20):11890 – 5, 1992.

[51] W. A. Fertig, D. C. Johnston, L. E. Delong, R. W. McCallum, and M. B. Maple. Destruction of superconductivity at the onset of long-range magnetic order in the compound $ErRh_4B_4$. *Phys. Rev. Lett.*, 38(17):987 – 90, 1977.

[52] A. Fukushima, A. Sato, A. Iwasa, Y. Nakamura, T. Komatsuzaki, and Y. Sakamoto. Attenuation of microwave filters for single-electron tunneling experiments. *IEEE Transactions on Instrumentation and Measurement*, 46(2):289 – 93, 1997.

[53] P. L. Gammel, B. Barber, D. Lopez, A. P. Ramirez, D. J. Bishop, S. L. Bud'ko, and P. C. Canfield. Enhanced critical currents of superconducting $ErNi_2B_2C$ in the ferromagnetically ordered state. *Phys. Rev. Lett.*, 84(11):2497 – 500, 2000.

[54] P. L. Gammel, B. P. Barber, A. P. Ramirez, C. M. Varma, D. J. Bishop, P. C. Canfield, V. G. Kogan, M. R. Eskildsen, N. H. Andersen, K. Mortensen, and K. Harada. Effects of magnetic order on the superconducting length scales and critical fields in single crystal $ErNi_2B_2C$. *Phys. Rev. Lett.*, 82(8):1756 – 9, 1999.

[55] B. W. Gardner et al. Scanning superconducting quantum interference device susceptometry. *Rev. Sci. Inst.*, 72(5):2361 – 4, 2001.

[56] P. G. De Gennes. Boundary effects in superconductors. *Rev. Mod. Phys.*, 36(1):225 – 237, 1964.

[57] H. S. Greenside, E. I. Blount, and C. M. Varma. Possible coexisting superconducting and magnetic states. *Phys. Rev. Lett.*, 46(1):49 – 53, 1981.

[58] Janice W. Guikema. *Scanning Hall probe microscopy of magnetic vortices in very underdoped Yttrium-Barium-Copper-Oxide.* PhD thesis, Stanford University, 2004. unpublished.

[59] A. Gurevich. Enhancement of the upper critical field by nonmagnetic impurities in dirty two-gap superconductors. *Phys. Rev. B*, 67(18):184515 – 1, 2003.

[60] A. Gurevich and V. M. Vinokur. Phase textures induced by dc current pair-breaking in multilayer structures and two-gap superconductors. *Phys. Rev. Lett.*, 97(13):137003 – 137006, 2006.

[61] K. Hasselbach, D. Mailly, and J. R. Kirtley. Micro-superconducting quantum interference device characteristics. *J. Appl. Phys.*, 91(7):4432 – 7, 2002.

[62] Martin E. Huber et al. (unpublished).

[63] M. Ishikawa and O. Fischer. Destruction of superconductivity by magnetic ordering in $Ho_{1.2}Mo_6S_8$. *Solid State Commun.*, 23(1):37 – 9, 1977.

[64] B. I. Ivlev and N. B. Kopnin. Electric currents and resistive states in thin superconductors. *Adv. Phys.*, 33(1):47 – 114, 1984. and references therein.

[65] John D. Jackson. *Classical Electrodynamics, 3rd Ed.* USA : Wiley, 1998, 1998.

[66] S. S. James, C. D. Dewhurst, S. B. Field, D. M. Paul, Y. Paltiel, H. Shtrikman, E. Zeldov, and A. M. Campbell. Flux pinning mechanisms in $ErNi_2B_2C$. *Phys. Rev. B*, 64(9):092512 – 4, 2001.

[67] E. M. Q. Jariwala, P. Mohanty, M. B. Ketchen, and R. A. Webb. Diamagnetic persistent current in diffusive normal-metal rings. *Phys. Rev. Lett.*, 86(8):1594 – 7, 2001.

[68] A. M. Kadin, L. N. Smith, and W. J. Skocpol. Charge imbalance waves and nonequilibrium dynamics near a superconducting phase-slip center. *J. Low Temp. Phys.*, 38(3/4):497 – 34, 1980.

[69] R. L. Kautz, G. Zimmerli, and J. M. Martinis. Self-heating in the coulomb-blockade electrometer. *J. of Appl. Phys.*, 73(5):2386 – 96, 1993.

[70] H. Kawano-Furukawa, E. Habuta, T. Nagata, M. Nagao, H.Yoshizawa, N. Furukawa, and H. Takeya K. Kadowaki. Spontaneous vortex phase in $ErNi_2{}^{11}B_2C$. *cond-mat/0106273*, 2001.

[71] H. Kawano-Furukawa, H. Takeshita, M. Ochiai, T. Nagata, H. Yoshizawa, N. Furukawa, H. Takeya, and K. Kadowaki. Weak ferromagnetic order in the superconducting $ErNi_2{}^{11}B_2C$. *Phys. Rev. B*, 65(18):180508(R) – 4, 2002.

[72] Francoise Kidwingira, J. D. Strand, D. J. Van Harlingen, and Yoshiteru Maeno. Dynamical superconducting order parameter domains in Sr_2RuO_4. *Science*, 314(5803):1267 – 1271, 2006.

[73] J. R. Kirtley, C. Kallin, C. W. Hicks, E. Kim, Y. Liu, K. A. Moler, Y. Maeno, and K. D. Nelson. Upper limit on spontaneous supercurrents in Sr_2RuO_4. *Phys. Rev. B*, 76(1):14526 – 8, 2007.

[74] J. R. Kirtley and J. P. Wikswo. Scanning SQUID microscopy. *Annual Review of Materials Science*, 29:117 – 148, 1999.

[75] M. R. Koblischka and R. J. Wijngaarden. Magnetooptical investigations of superconductors. *Superconductor Science & Technology*, 8(4):199 – 213, 1995.

[76] R. H. Koch, D. P. DiVincenzo, and J. Clarke. Model for $1/f$ flux noise in SQUIDs and qubits. *Phys. Rev. Lett.*, 98(26):1 – 4, 2007.

[77] V. G. Kogan, A. Y. Simonov, and M. Ledvij. Magnetic field of vortices crossing a superconductor surface. *Phys. Rev. B*, 48(1):392 – 7, 1993.

[78] Nicholas C. Koshnick, Hendrik Bluhm, Martin E. Huber, and Kathryn A. Moler. Fluctuation Superconductivity in Mesoscopic Aluminum Rings. *Science*, 318(5855):1440–1443, 2007.

[79] L. Kramer and R. J. Watts-Tobin. Theory of dissipative current-carrying states in superconducting filaments. *Phys. Rev. Lett.*, 40(15):1041 – 4, 1978.

[80] V. E. Kravtsov and B. L. Altshuler. Relationship between the noise induced persistent current and the dephasing rate. *Phys. Rev. Lett.*, 84(15):3394 – 7, 2000.

[81] C. G. Kuper, M. Revzen, and A. Ron. Ferromagnetic superconductors: a vortex phase in ternary rare-earth compounds. *Phys. Rev. Lett.*, 44(23):1545 – 8, 1980.

[82] J. S. Langer and V. Ambegaokar. Intrinsic resistive transition in narrow superconducting channels. *Phys. Rev.*, 164(2):498 – 510, 1967.

[83] L. P. Levy, G. Dolan, J. Dunsmuir, and H. Bouchiat. Magnetization of mesoscopic copper rings: evidence for persistent currents. *Phys. Rev. Lett.*, 64(17):2074 – 7, 1990.

[84] G. M. Luke, Y. Fudamoto, K. M. Kojima, M. I. Larkin, J. Merrin, B. Nachumi, Y. J. Uemura, Y. Maeno, Z. Q. Mao, Y. Mori, H. Nakamura, and M. Sigrist. Time-reversal symmetry-breaking superconductivity in Sr_2RuO_4. *Nature*, 394(6693):558 – 61, 1998.

[85] J. W. Lynn, D. E. Moncton, W. Thomlinson, G. Shirane, and R. N. Shelton. Direct observation of long range ferromagnetic order in the reentrant superconductor $HoMo_6S_8$. *Solid State Commun.*, 26(8):493 – 6, 1978.

[86] J. W. Lynn, G. Shirane, W. Thomlinson, and R. N. Shelton. Competition between ferromagnetism and superconductivity in $HoMo_6S_8$. *Phys. Rev. Lett.*, 46(5):368 – 71, 1981.

[87] A. P. Mackenzie and Y. Maeno. The superconductivity of Sr_2RuO4 and the physics of spin-triplet pairing. *Rev. Mod. Phys.*, 75(2):657 – 712, 2003. and references therein.

[88] Y. Maeno, H. Hashimoto, K. Yoshida, S. Nishizaki, T. Fujita, J. G. Bednorz, and F. Lichtenberg. Superconductivity in a layered perovskite without copper. *Nature (London)*, 372(6506):532 – 4, 1994.

[89] D. Mailly, C. Chapelier, and A. Benoit. Experimental observation of persistent currents in a gaas-algaas single loop. *Phys. Rev. Lett.*, 70(13):2020 – 3, 1993.

[90] J. M. Martinis, M. H. Devoret, and J. Clarke. Experimental tests for the quantum behavior of a macroscopic degree of freedom: the phase difference across a josephson junction. *Phys. Rev. B*, 35(10):4682 – 98, 1987.

[91] J. M. Martinis and M. Nahum. Effect of environmental noise on the accuracy of coulomb-blockade devices. *Phys. Rev. B*, 48(24):18316 – 19, 1993.

[92] M. Matsumoto and M. Sigrist. Quasiparticle states near the surface and the domain wall in a $p_x \pm ip_y$-wave superconductor. *J. Phys. Soc. J.*, 68(3):994 – 1007, 1999. See also erratum in Vol. 68, p. 3120.

[93] D. E. McCumber and B. I. Halperin. Time scale of intrinsic resistive fluctuations in thin superconducting wires. *Phys. Rev. B*, 1(3):1054 – 70, 1970.

[94] Y. Meir, Y. Gefen, and O. Entin-Wohlman. Universal effects of spin-orbit scattering in mesoscopic systems. *Phys. Rev. Lett.*, 63(7):798 – 800, 1989.

[95] R. Meservey and B. B. Schwartz. *Equilibrium properties: comparison of experimental results with predictions of the BCS theory.*, pages 117 – 84. Marcel Dekker Inc., New York, 1969.

[96] S. Michotte, S. Matefi-Tempfli, L. Piraux, D. Y. Vodolazov, and F. M. Peeters. Condition for the occurrence of phase slip centers in superconducting nanowires under applied current or voltage. *Phys. Rev. B*, 69(9):094512 –, 2004.

[97] F. P. Milliken, J. R. Rozen, G. A. Keefe, and R. H. Koch. 50 Ω characteristic impedance low-pass metal powder filters. *Rev. Sci. Inst.*, 78(2):24701 – 1, 2007.

[98] P. Mohanty and R. A. Webb. Decoherence and quantum fluctuations. *Phys. Rev. B*, 55(20):R13452 – 5, 1997.

[99] D. E. Moncton, D. B. McWhan, P. H. Schmidt, G. Shirane, W. Thomlinson, M. B. Maple, H. B. MacKay, L. D. Woolf, Z. Fisk, and D. C. Johnston. Oscillatory magnetic fluctuations near the superconductor-to-ferromagnet transition in $ErRh_4B_4$. *Phys. Rev. Lett.*, 45(25):2060 – 3, 1980.

[100] G. Montambaux, H. Bouchiat, D. Sigeti, and R. Friesner. Persistent currents in mesoscopic metallic rings: ensemble average. *Phys. Rev. B*, 42(12):7647 – 50, 1990.

[101] E. Morenzoni, T. Prokscha, A. Suter, H. Luetkens, and R. Khasanov. Nanoscale thin film investigations with slow polarized muons. *J. Phys. Cond. Mat.*, 16(40):S4583 – 601, 2004.

[102] A. Moser, H. J. Hug, I. Parashikov, B. Stiefel, O. Fritz, H. Thomas, A. Baratoff, H. J. Guntherodt, and P. Chaudhari. Observation of single vortices condensed into a vortex-glass phase by magnetic force microscopy. *Phys. Rev. Lett.*, 74(10):1847 – 50, 1995.

[103] K. D. Nelson, Z. Q. Mao, Y. Maeno, and Y. Liu. Odd-parity superconductivity in Sr_2RuO_4. *Science*, 306(5699):1151 – 4, 2004.

[104] T. K. Ng and C. M. Varma. Spontaneous vortex phase discovered?. *Phys. Rev. Lett.*, 78(2):330 – 3, 1997.

[105] C. Noce and L. Maritato. Microscopic equivalence between the two-band model and mcmillan proximity-effect theory. *Phys. Rev. B*, 40(1):734 – 6, 1989.

[106] J. Pearl. Structure of superconductive vortices near a metal-air interface. *J. Appl. Phys.*, 37(11):4139, 1966.

[107] S. Pedersen, G. R. Kofod, J. C. Hollingbery, C. B. Sorensen, and P. E. Lindelof. Dilation of the giant vortex state in a mesoscopic superconducting loop. *Phys. Rev. B*, 64(10):104522 – 4, 2001.

[108] R. B. Pettit and J. Silcox. Film structure and enhanced superconductivity in evaporated aluminium films. *Phys. Rev. B*, 13(7):2865 – 72, 1976.

[109] F. Pierre, A. B. Gougam, A. Anthore, H. Pothier, D. Esteve, and N. O. Birge. Dephasing of electrons in mesoscopic metal wires. *Phys. Rev. B*, 68(8):85413 – 1, 2003.

[110] B. L. T. Plourde, T. L. Robertson, P. A. Reichardt, T. Hime, S. Linzen, C. E. Wu, and J. Clarke. Flux qubits and readout device with two independent flux lines. *Phys. Rev. B*, 72(6):60506 – 1, 2005.

[111] Frank Pobell. *Matter and methods at low temperatures*. Springer, 2nd edition, 1996.

[112] David M. Pozar. *Microwave Engineering*. USA: Addison Wesley, 1990, 1990.

[113] W. Rabaud, L. Saminadayar, D. Mailly, K. Hasselbach, A. Benoit, and B. Etienne. Persistent currents in mesoscopic connected rings. *Phys. Rev. Lett.*, 86(14):3124 – 7, 2001.

[114] B. Reulet, M. Ramin, H. Bouchiat, and D. Mailly. Dynamic response of isolated aharonov-bohm rings coupled to an electromagnetic resonator. *Phys. Rev. Lett.*, 75(1):124 – 7, 1995.

[115] E. K. Riedel and F. von Oppen. Mesoscopic persistent current in small rings. *Phys. Rev. B*, 47(23):15449 – 59, 1993.

[116] B. J. Roth, N. G. Sepulveda, and J. P. Wikswo. Using a magnetometer to image a two-dimensional current distribution. *J. Appl. Phys.*, 65(1):361 – 72, 1989.

[117] D. Rugar, H. J. Mamin, P. Guethner, S. E. Lambert, J. E. Stern, I. McFadyen, and T. Yogi. Magnetic force microscopy: general principles and application to longitudinal recording media. *J. Appl. Phys.*, 68(3):1169 – 83, 1990.

[118] N. Saha, R. Surdeanu, M. Marchevsky, G. J. Nieuwenhuys, C. D. Dewhurst, R. J. Wijngaarden, D. M. Paul, and P. H. Kes. Magnetic twin boundaries and flux pinning in the antiferromagnetic superconductor $ErNi_2B_2C$. *Phys. Rev. B*, 63(2):020502(R) – 4, 2000.

[119] J. E. Sauvageau, C. J. Burroughs, P. A. A. Booi, M. W. Cromar, S. P. Benz, and J. A. Koch. Superconducting integrated circuit fabrication with low temperature ECR-based PECVD SiO_2 dielectric films. *IEEE Transactions on Applied Superconductivity*, 5(2):2303 – 2309, 1995.

[120] M. Schechter, Y. Oreg, Y. Imry, and Y. Levinson. Magnetic response of disordered metallic rings: Large contribution of far levels. *Phys. Rev. Lett.*, 90(2):026805 – 4, 2003.

[121] A. Schmid. Persistent currents in mesoscopic rings by suppression of charge fluctuations. *Phys. Rev. Lett.*, 66(1):80 – 3, 1991.

[122] A. Schmid, G. Schön, and M. Tinkham. Dynamic properties of superconducting weak links. *Phys. Rev. B*, 21(11):5076 – 86, 1980.

[123] P. Schwab. Persistent current in metals with a large dephasing rate. *European Physical Journal B*, 18(2):189 – 92, 2000.

[124] P. Schwab and U. Eckern. Persistent current induced by magnetic impurities. *Zeitschrift fur Physik B (Condensed Matter)*, 103(1):97 – 103, 1997.

[125] T. Siegrist, H. W. Zandbergen, R. J. Cava, J. J. Krajewski, and W. F. Peck. The crystal structure of superconducting $LuNi_2B_2C$ and the related phase LuNiBC. *Nature (London)*, 367(6460):254 – 6, 1994.

[126] M. Sigrist, T. M. Rice, and K. Ueda. Low-field magnetic response of complex superconductors. *Phys. Rev. Lett.*, 63(16):1727 – 30, 1989.

[127] W. J. Skocpol, M. R. Beasley, and M. Tinkham. Phase-slip centers and nonequilibrium processes in superconducting tin microbridges. *J. Low Temp. Phys.*, 16(1/2):145 – 67, 1974.

[128] Lafe Spietz, John Teufel, and R. J. Schoelkopf. A twisted pair cryogenic filter. *cond-mat/0601316*, 2006.

[129] M. Stone and Suk-Bum Chung. Fusion rules and vortices in $p_x + ip_y$ superconductors. *Phys. Rev. B*, 73(1):014505 – 1, 2006.

[130] H. Suhl, B. T. Matthias, and L. R. Walker. Bardeen-cooper schrieffer theory of superconductivity in the case of overlapping bands. *Phys. Rev. Lett.*, 3(12):552 – 554, 1959.

[131] Y. Tanaka. Soliton in two-band superconductor. *Phys. Rev. Lett.*, 88(1):017002 – 3, 2002.

[132] M. B. Tarlie and K. R. Elder. Metastable state selection in one-dimensional systems with a time-ramped control parameter. *Phys. Rev. Lett.*, 81(1):18 – 21, 1998.

[133] R. Tidecks. Current-induced nonequilibrium phenomena in quasi-one-dimensional superconductors - introduction. *Springer Tracts in Modern Physics*, 121, 1990.

[134] N. Trivedi and D. A. Browne. Mesoscopic ring in a magnetic field: reactive and dissipative response. *Phys. Rev. B*, 38(14):9581 – 93, 1988.

[135] L. Ya. Vinnikov, J. Anderegg, S. L. Bud'ko, P. C. Canfield, and V. G. Kogan. Domain structure in $ErNi_2B_2C$ and $HoNi_2B_2C$ single crystals observed by a high-resolution bitter decoration technique. *Phys. Rev. B*, 71(22):224513 – 1, 2005.

[136] D. Vion, P. F. Orfila, P. Joyez, D. Esteve, and M. H. Devoret. Miniature electrical filters for single electron devices. *J. of Appl. Phys.*, 77(6):2519 – 24, 1995.

[137] D. Y. Vodolazov and F. M. Peeters. Dynamic transitions between metastable states in a superconducting ring. *Phys. Rev. B*, 66(5):054537 – 7, 2002.

[138] D. Y. Vodolazov, F. M. Peeters, S. V. Dubonos, and A. K. Geim. Multiple flux jumps and irreversible behavior of thin al superconducting rings. *Phys. Rev. B*, 67(5):054506 – 1, 2003.

[139] F. von Oppen and E. K. Riedel. Average persistent current in a mesoscopic ring. *Phys. Rev. Lett.*, 66(1):84 – 7, 1991.

[140] F. von Oppen and E. K. Riedel. Flux-periodic persistent current in mesoscopic superconducting rings close to T_c. *Phys. Rev. B*, 46(5):3203 – 6, 1992.

[141] J. Vranken and C. Van Haesendonck and Y. Bruynseraede. Enhanced magnetic surface scattering of weakly localized electrons. *Phys. Rev. B*, 37(14):8502 – 5, 1988.

[142] R. J. Watts-Tobin, Y. Krähenbühl, and L. Kramer. Nonequilibrium theory of dirty, current-carrying superconductors: phase-slip oscillators in narrow filaments near T_c. *J. Low Temp. Phys.*, 42(5/6):459 – 501, 1981.

[143] J. Wei, S. Pereverzev, and M. E. Gershenson. Microwave-induced dephasing in one-dimensional metal wires. *Phys. Rev. Lett.*, 96(8):1 – 4, 2006.

[144] Jing Xia, Yoshiteru Maeno, Peter T. Beyersdorf, M. M. Fejer, and Aharon Kapitulnik. High resolution polar kerr effect measurements of Sr_2RuO_4: Evidence for broken time-reversal symmetry in the superconducting state. *Phys. Rev. Lett.*, 97(16):167002, 2006.

[145] X. Zhang and J. C. Price. Susceptibility of a mesoscopic superconducting ring. *Phys. Rev. B*, 55(5):3128 – 3140, 1997.

[146] A. B. Zorin. The thermocoax cable as the microwave frequency filter for single electron circuits. *Rev. Sci. Inst.*, 66(8):4296 – 300, 1995.